Design and Analysis of a Monolithic Flexure Atomic Force Microscope

by

Dean Marko Ljubicic

Submitted to the Department of Mechanical Engineering
in partial fulfillment of the requirements for the degree of

Master of Science

at the

MASSACHUSETTS INSTITUTE OF TECHNOLOGY

June 2008

Author .....
Department of Mechanical Engineering
May 19, 2008

Certified by .....
David L. Trumper
Professor
Thesis Supervisor

Accepted by .....
Lallit Anand
Chairman, Department Committee on Graduate Students

Design and Analysis of a Monolithic Flexure Atomic Force Microscope

by

Dean Marko Ljubicic

Submitted to the Department of Mechanical Engineering
on May 19, 2008, in partial fulfillment of the
requirements for the degree of
Master of Science

Abstract

This thesis details the design, manufacture, and testing of a sub-nanometer accuracy atomic force microscope. It was made to be integrated into the Sub-Atomic Measuring Machine (SAMM) in collaboration with the University of North Carolina at Charlotte (UNCC). The microscope uses a tuning fork sensor to gauge its proximity to the sample surface. The sensor is fixed to a stage that is guided to move in one degree of freedom by a monolithic flexure. A piezoelectric actuator drives the moving stage while three capacitance sensors provide a non-contact direct measurement of the displacement. A decoupling flexure prohibits the error motions of the actuator from propagating into the moving stage.

A digital control system uses closed loop control to regulate the vertical displacement of the stage. The positioning system demonstrated a 450 Hz -3db closed loop bandwidth and 0.249 RMS noise positioning. A new probe named after its inventor Dr. Terunobu Akiyama is implemented in a feedback control system that adjusts the displacement of the stage in order to maintain a constant gap between the probe and the sample. The system displayed an 8.3 nm RMS positioning noise when set to measure a stationary block of aluminum. The dynamics of the feedback control loop indicate that the system can operate at 27 Hz upon application of a proportional controller. Advanced methods to self excite the tuning fork sensor at resonance by use of a phase locked loop are explored. Follow-up work to integrate the atomic force microscope into the SAMM stage, diminish the electrical noise in the tuning fork, and to implement the phase locked loop circuit are suggested.

Thesis Supervisor: David L. Trumper
Title: Professor

Acknowledgments

I would like to first and foremost thank my advisor Professor David Trumper. I've found he is deeply knowledgeable and skilled in a variety of disciplines ranging from both electrical and mechanical engineering to literary arts. I found Professor Trumper unequivocally upholds a set of first-rate standards with every project he becomes involved with. This became evident to me after observing the quality and caliber of both his and his student's work as well as the passion and thoroughness in which Professor Trumper lectures with in the classroom. I reserve a special thanks for the patience and understanding given to me by Professor Trumper at the beginning of my graduate experience when my own bearings had been temporarily lost.

I would also like to thank Professor Robert Hocken at UNC Charlotte for his contribution to the mechanical design of the project. I learned a great deal from Professor Hocken's intuition and expertise of mechanical systems on a nanoscale. Both he and Jerald Overcash provided useful support and technical advice upon the integration of the atomic force microscope into the SAMM stage.

I wish to thank a handful of people here at MIT that made the completion of my thesis possible. Both Professors Martin Culpepper and Alex Slocum provided valuable input upon the mechanical design of the microscope. Jerry Wentworth always made himself available to field my questions on machining and motorcycles. Mark Belanger graciously extended to me his expertise and resources in the Edgerton student machine shop when LMP became busy. Lastly I wanted to also thank Aaron Mazzeo for donating his time at the beginning of the project to catch me up to speed on his hardware.

I could not have finished this thesis without the help and support of my fellow labmates. I must first thank Ian MacKenzie who always provided an open ear to listen to both my mechanical designs and personal affairs. Ian's sharp wit and colorful sense of humor found a way to bring light to a laboratory devoid of windows. I also wish to thank Aaron Gawlik whose dependable support and solid character spoke for him when his quiet nature was too modest to pipe up. On the other hand there

was Kevin Miu who arguably spoke too much and at the same time never enough. I found Kevin's incredible work ethic was somehow outdone by his selflessness to which I remain indebted.

Finally I must acknowledge my family whose concrete support has never faltered. They supply my basis with such naturalness that I often take it for granted but always remain deeply grateful.

Contents

List of Figures

List of Tables

Chapter 1

Introduction

1.1 Project Summary

This thesis presents the design and testing of an atomic force microscope developed for high accuracy metrology. The microscope was designed to integrate into and deliver compatible performance as a probe for the Sub-Atomic Measuring Machine (SAMM), a precision metrology stage at the University of North Carolina at Charlotte (UNCC). The microscope can linearly actuate and measure the displacement of a moving stage in one degree of freedom. The functional requirements of the microscope are:

1 nm accuracy

20 micron range

100 Hz closed loop bandwidth

1.4" diameter geometrical constraint

1 micron resolution coarse adjust

1mm diameter coarse view target visibility

Figure 1-1 shows a three dimensional CAD model of the final design followed by Figure 1-2 which shows the a digital photo of the microscope head viewed from the top and from the bottom. A central Invar stage carries the AFM probe and is guided to move in one degree of freedom by radially symmetric steel flexures. A high voltage piezoactuator drives the stage while three capacitance sensors measure its displace-

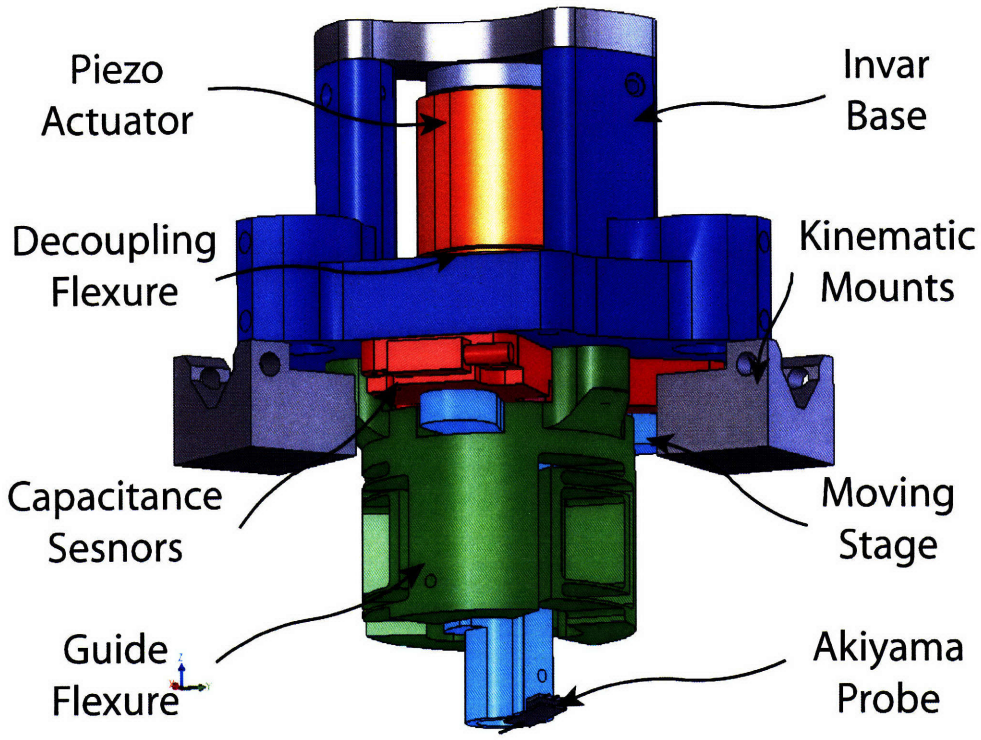

Figure 1-1: 3 dimensional CAD drawing of the instrument shot from the underside.

ment. Error motions in the piezoactuator are decoupled from the stage by a hinge flexure. A borescope nested concentrically though the center of the microscope provides coarse imaging of the sample for locating features. Three ball screws preloaded into kinematic mounts allow for micron resolution coarse adjustment of the microscope over a quarter inch of travel. The newly available Akiyama probe [38] mounted on the bottom of the stage is used to sense the surface of the sample though atomic force microscopy.

The instrument was designed for high accuracy positioning. The relative stiffnesses between the guide flexure and the decoupling flexure in parallel degrees of freedom is used to deamplify error motions introduced by the piezoelectric actuator. Figure 1-3 shows CAD drawings of both of these flexures side by side. Figure 1-4 shows their orientation and integration into the instrument via a cross sectional view. The atomic force microscope was designed to be thermally stable by making every component in the metrology loop out of Invar. The forces required to actuate the stage that result

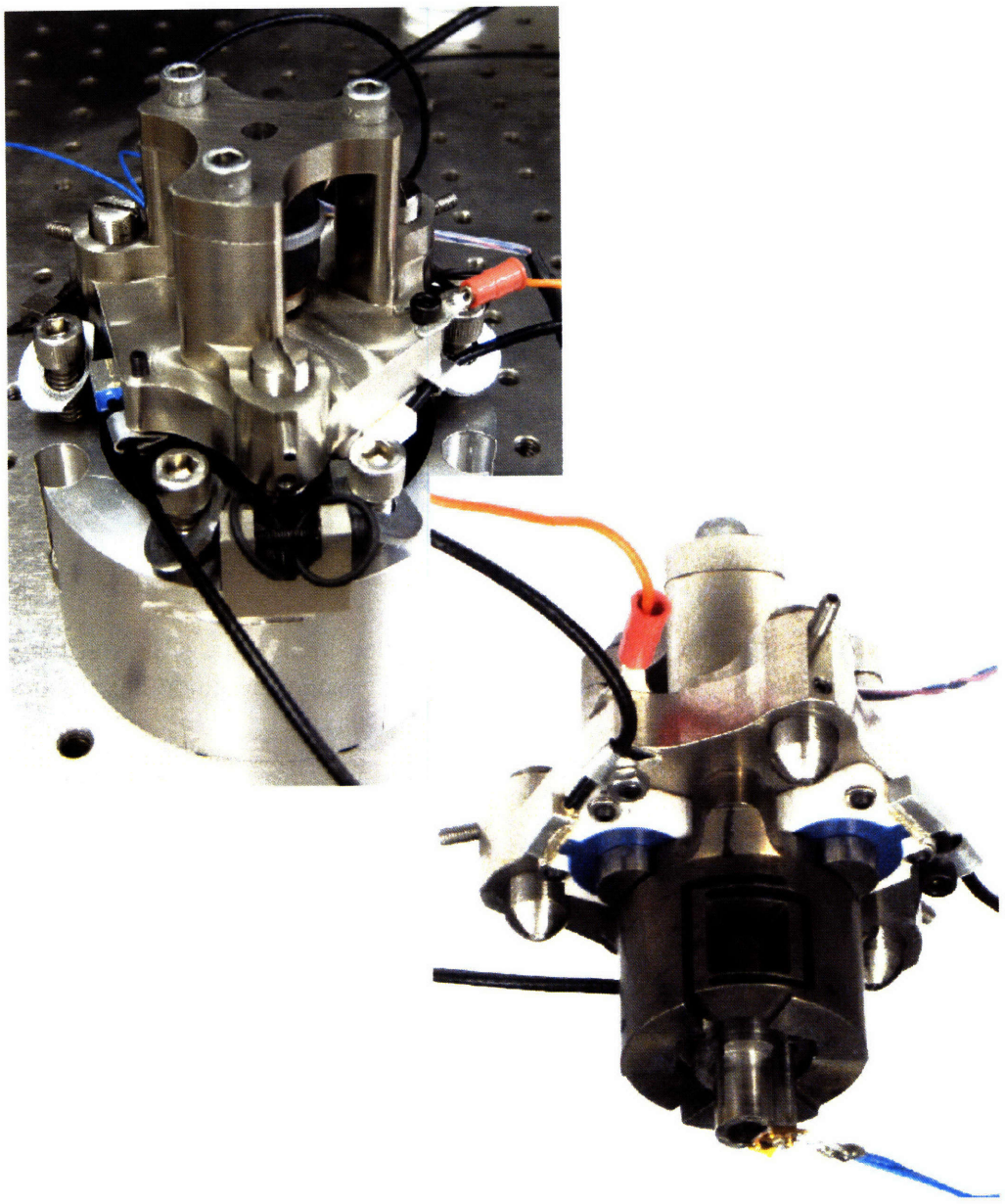

Figure 1-2: Two digital photos of the instrument as built. The upper photo shows the instrument sitting in a fixture designed to hold it during testing. The lower photo shows the Akyiyama probe mounted at the tip of the Invar stage.

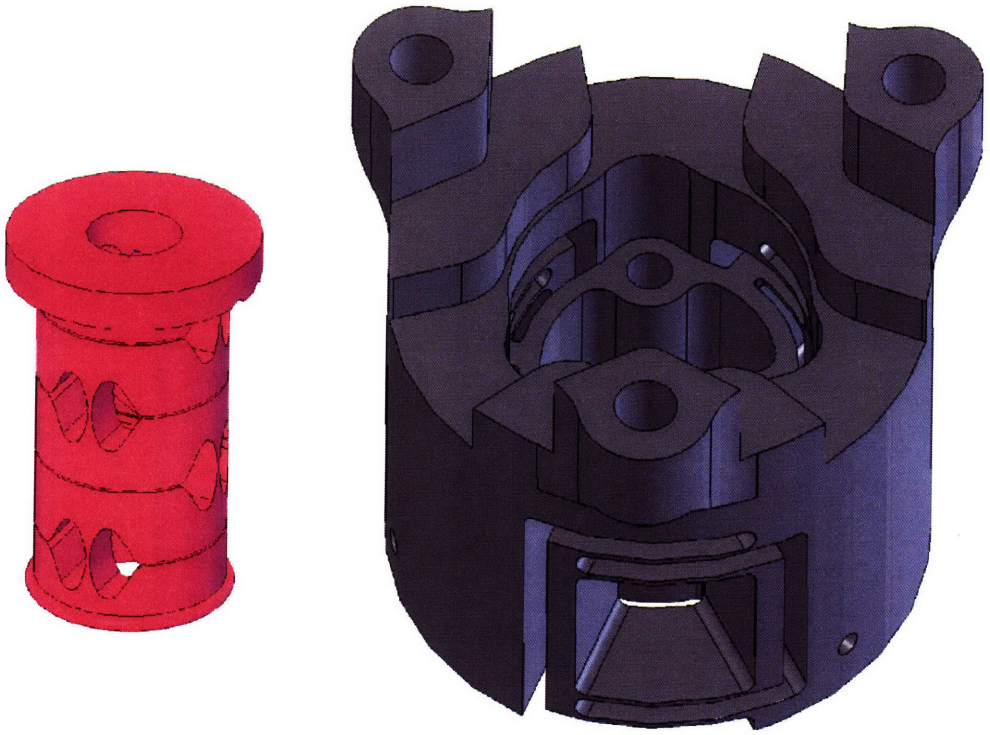

Figure 1-3: CAD drawing of the two flexures designed in the thesis in relative scale to each other. The decoupling flexure sits on the left while the guide flexure sits on the right.

in nanoscale deflections of the body of the microscope flow in a force loop that does not intersect the metrology loop.

We have built and tested the atomic force microscope as described above. The piezoelectric actuator can move the stage approximately 20 μm. The three capacitance sensors measure its position with 0.170 nm RMS noise at 1000 Hz bandwidth. Three 80 tpi screws made of Invar are used to adjust the height of the tip by 0.3 μm per degree turned per screw. High resolution analog to digital boards were used in the electrical system and had an measured output of 20 effective bits. While using these high resolution boards, our sampling rate was limited to 8 kHz which added a significant phase lag to a wide range of frequencies. We find that by instead using a 50 kHz sampling rate, the phase at the 200 Hz crossover increases by 23 degrees.

We used a dSpace digital controller board software to rapidly test and augment

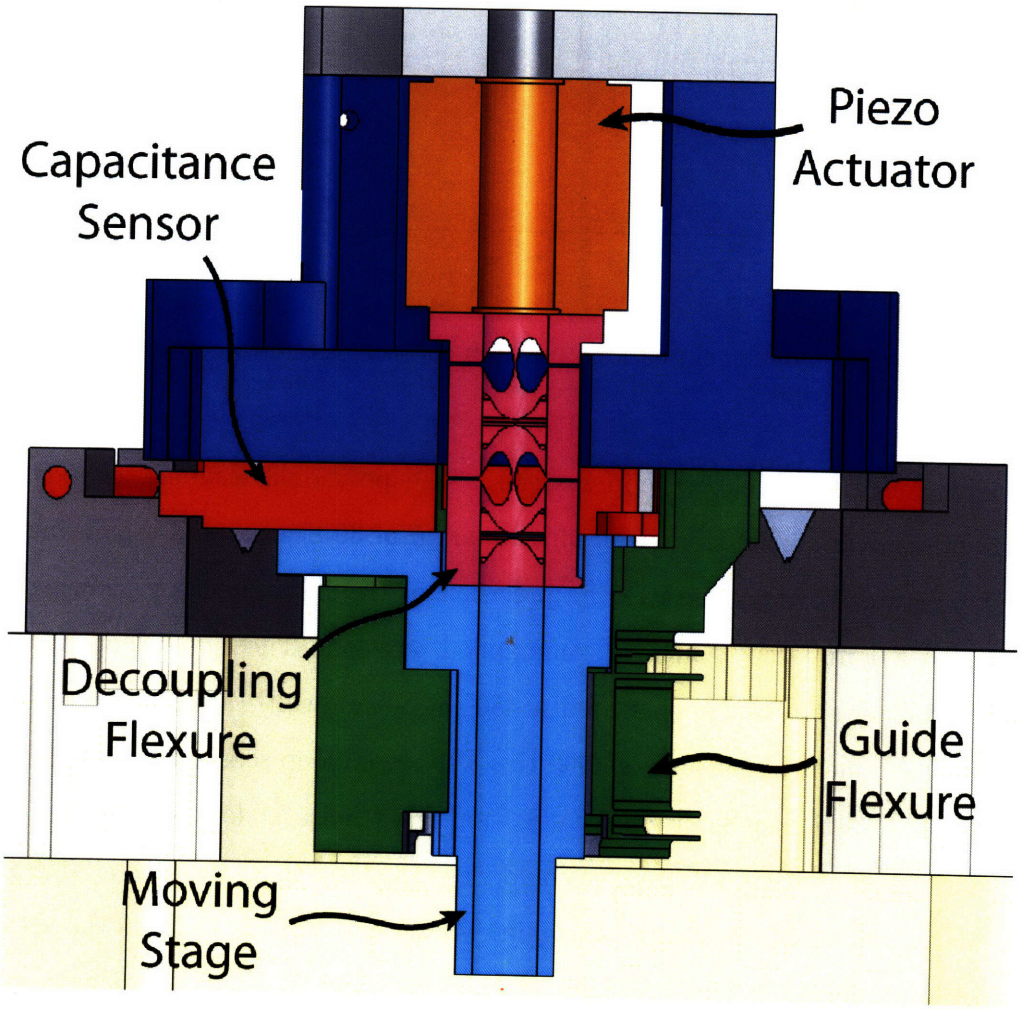

Figure 1-4: Cross sectional view of the atomic force microscope showing the geometrical interaction and placement of the two flexures within the instrument.

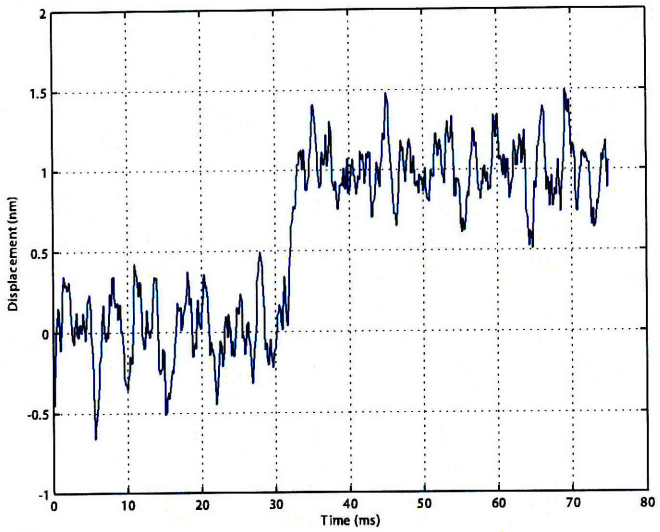

Figure 1-5: Reaction of the closed loop position control system to a 1 nm step change in commanded position.

controllers for the two closed loop systems. The positional feedback closed loop system crosss over at 200 Hz with a phase margin of 30 degrees and a gain margin of 1.81. Figure 1-5 demonstrates the precision of the instrument by showing the response to a 1 nm step change in commanded position. The closed loop position feedback control system demonstrated a 450 -3dB bandwidth and 0.249 nm RMS noise a measurement bandwidth of 1000 Hz. The closed loop sensor feedback control system held a stationary position with 8.3 nm RMS noise at low bandwidth. The dynamics of this system indicated we could close the loop at 27 Hz with a 30 degree phase margin by simply increasing the gain. More work remains to do in the area of the probe control.

1.2 Thesis Overview

The remainder of this chapter includes a brief history of atomic force microscopy followed by a review of the latest research in high accuracy metrology. In Chapter 2 we derive the fundamental equations that govern the physics behind flexures and cover practical guidelines for their manufacture and use. Chapter 3 describes the design

and testing of a simple, flexural guided nanopositioner. The next chapter presents the design and manufacture of the one degree of freedom monolithic flexure. Chapter 5 evaluates the positioning errors derived from by mechanical and thermal noise. Chapter 6 examines the details of various mechanical and electrical systems within the atomic force microscope. Chapter 7 describes the control system implemented to control the position of the moving stage via the displacement reading from the capacitance sensors. Chapter 8 describes the tests preformed to characterize the Akiyama probe and the control strategy used to regulate the stage displacement from feedback of the probe. Finally in the last chapter we discuss the results and progress of the thesis and offer suggestions for future work.

1.3 Background

1.3.1 Atomic Force Microscopy

Modern day atomic imaging traces its origins back to the scanning tunneling microscope (STM) invented by Binning and Rohrer in 1982 [10]. This instrument allowed researchers for the first time in history to create images with subatomic resolution of sample surfaces. The first of many applications of the STM helped scientists in 1985 build an atomic model of the diamond lattice of silicon [17]. The rapid success of this instrument led Binning and Rohrer to win the Nobel Prize in 1986.

The most innovative part of the STM was its tip sensing technology. During operation of the instrument, a constant voltage difference is held between a sharp, conductive probe and the sample. In a homogeneous sample, the current that flows from the tip to the sample varies only by the probe-to-sample gap, typically between 0.4 to 0.7 nm [6]. As the sample is raster scanned laterally, a feedback loop monitors the current through the probe and vertically adjusts tip in order to maintain a constant current. The microscope records the lateral movement of the stage and the vertical movement of the tip to generate a contour map of the sample surface. This type of current-monitored height detection is used for various other applications such

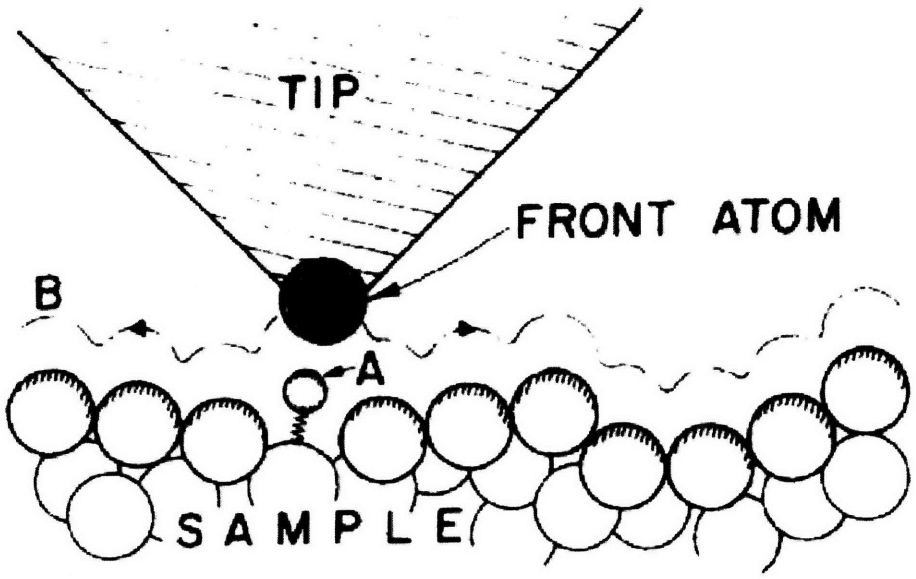

Figure 1-6: Cross Sectional view of a current-based height detection probe, taken from [11].

as the plasma cutting of steel[15].

The scanning tunneling microscope employed a new type of tip sensing that far outperformed other imaging technologies of its time. Conventional far-field optical microscopes use the reflection of light in order to resolve an image of a sample. These types of images have a resolution of about 200 nm limited by the wavelength and diffraction of light. By relying on electrical signals instead of electromagnetic radiation, the STM is able to avoid the problems associated with diffraction. Instead, the STM monitors the electron tunneling current which decreases exponentially with standoff distance. Because most of the current flows through the closest atom of the tip to the sample surface, the STM operates with effectively an atomically sharp probe with a demonstrated lateral resolution of 0.1 nm and vertical resolution of 0.01 nm [5]. This concept is depicted in Figure 1-6 as taken from [11]. This vast improvement in resolution revolutionized nanometrology.

The main drawback to STM imaging is that the sample must conduct electricity. This excludes many biological or carbon based samples from being able to be scanned.

Researchers have plated biological elements with a fine coat of gold but this operation often changes the landscape of the specimen by dulling the edges and crevices [3]. This operation also limits itself to biological samples that are no longer living. To address this problem, a new type of microscopy dubbed atomic force microscopy (AFM) was invented and has become the preferred type of metrology for non-conductive samples.

The term "atomic force microscope" covers a variety of instruments beginning with first AFM invented by Binnig in 1983 [9]. As indicated by its name, the AFM was made to sense minute changes in force as small as 10^{-18}N delivered by singular atoms upon a tiny cantilever. The cantilever was actuated by a piezoelectric element to resonate at a harmonic of its natural frequency. The atomic forces perturb the natural resonance of the oscillating cantilever and are thereby detected when the cantilever comes within proximity of the sample. A feedback control system was employed to maintain constant force, and therefore constant displacement, between the probe and the sample. Although the first AFM was invented two decades ago, it works almost identically to the one designed in this thesis by virtue of its "non-contact metrology."

Alternatively, there is a tip imaging dubbed "contact metrology" whereby a sharp cantilevered tip is essentially dragged across the sample surface. A laser is reflected off the back of the cantilever and detected with a photodiode as shown in Figure 1-7 [2]. Measuring the deflection of the laser over a distance amplifies the angle over which the dragging cantilever rotates thereby acquiring greater sensitivity. The stiffness of the cantilever must be weaker than the atomic interaction between the probe and the sample so that the cantilever deflects instead of the atoms being measured. Such low stiffness beams have low natural frequencies which limits the speed in which the instrument can measure. Also, the resolution of the image taken by contact metrology is inferior to non-contact metrology. In [12], Giessibl and Binnig demonstrate atomic resolution using this technology, but the method can only be applied in certain cases. Although the contact metrology AFM is slower and is generally not capable of atomic resolution, it is mechanically simpler than non-contact AFM's since it contains no

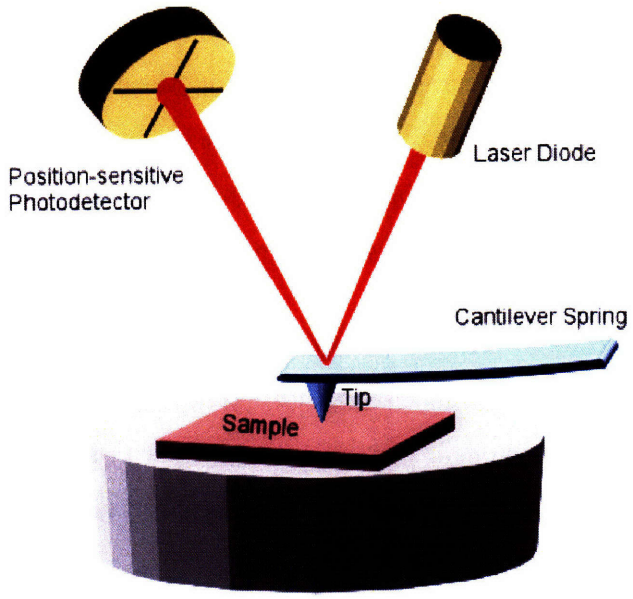

Figure 1-7: This schematic depicts the functionality and packaging of a laser interferometry atomic force microscope, taken from [2].

oscillating parts.

Looking to simplify the non-contact AFM, Karrai and Grober introduced a new tip imaging method in 1995 through the work reported in two successive papers [18, 19]. The silicon cantilever was replaced with a quartz tuning fork found in watches. These tuning forks are very inexpensive due to their mass production and tuned highly accurately to 32.768 kHz resonant frequency for time keeping purposes. Karrai and Grober developed their sensor by gluing a fine tip onto a watch crystal tuning fork. The piezoelectric nature of the tuning fork allowed for excitation of the fork without using a piezoelectric actuator. This simpler, more compact design allowed for the actuation and height sensing all in one unit, also making the optical laser obsolete. Although the raw materials of this probe are cheap and abundant, the tip forming and gluing process under Karrai and Grober's operation was rather crude and unrepeatable.

In [38] Akiyama develops a new process that addresses the drawbacks of Karrai and Gruber's self sensing, self actuating sensor. In his research, Akiyama used MEMS

fabrication to span a chemically etched AFM tip across two tines of a piezoelectric tuning fork. The fork itself is soldered and electrically connected to a base which is magnetically preloaded into a kinematic mount. This manufacturing process provides a securely positioned, fine tipped, self resonating and sensing, repeatable, and wireless probe that with careful handling can be easily replaced if broken. The lateral oscillation of the tines excites the cantilevered tip into a vertical pecking mode that probes the surface via non-contact metrology similar to Binnig's original AFM.

1.3.2 High-Accuracy Metrology

Although much attention needs to be granted to the tip sensing element, the focus of this thesis is primarily on the pursuit of 1 nm accuracy positioning and metrology. Many AFM's to-date have demonstrated sub-nanometer resolution, but few have claimed sub-nanometer accuracy. For many biological and scientific purposes it is adequate to simply get an image of the sample surface without being strict with scale. As the miniaturization of components brings feature size down to the nanometer scale, the ability to accurately measure the size and shape of these parts becomes increasingly important.

Many AFM's use open loop metrology in order to achieve greater simplicity but sacrifice accuracy. When using open loop metrology, the measurement of position is derived from some quantity that does not directly represent the displacement of the probe. Open loop metrology AFM's using piezoelectric actuators often measure the position of the probe by assuming the piezoelectric's expansion and voltage potential are linearly proportional. This allows the designer to use the piezoelectric as an actuator and a position sensor. The voltage to displacement relationship is linear to the first degree but is subject to many nonlinearities such as hysterics, creep, and thermal expansion. These immeasurable inaccuracies affect the absolute position of the probe and ultimately degrade the accuracy of the measurement. Researchers in the field have worked to minimize these non-idealizations. Newcomb and Flynn showed that relating the capacitance instead of the voltage across a piezoelectric to

its expansion yields a more accurate relationship [29]. In other work, Jung and Kim have developed feed-forward control methods to reduce open loop errors by using deterministic hysteretic path models [16]. This work helps mitigate the effect of the inaccuracies but ultimately open loop metrology systems cannot meet the standards of our 1 nm accuracy metrological goal.

By using closed loop metrology, researchers have demonstrated significant improvements in imaging accuracy. Common applications of closed loop metrology use laser interferometers, capacitance sensors, or grid scales that directly measure the displacement of the target with reference to an isolated mechanical ground. This technology and closed loop metrology approach has for example been utilized by researchers at PTB to create a high accuracy three axis scanning stage [31]. The position and feedback control of an X-Y stage was measured through capacitance sensors calibrated in situ by laser interferometers in order to account for repeatable nonlinearities. This instrument was designed to operate in conjunction with a commercial STM microscope that measured the topography of the sample.

1.3.3 The Sub-Atomic Measuring Machine (SAMM)

The Sub-Atomic Measuring Machine is a nanometrology instrument designed and built at the University of North Carolina Charlotte (UNCC) under the supervision of Dr. Robert Hocken, Dr. David Trumper, and Dr. Chunhai Wang. The focus of the instrument is to achieve nanoscale accuracy measurements over macroscale ranges. This capability is most applicable to the semi-conductor industry which requires an accurate measure of their ever shrinking processors for quality control purposes.

The development of the SAMM stage began with the Angstrom Stage [14]. The core of this instrument is a neutrally buoyant stage floating in an oil bath. All six degrees of freedom are measured by capacitance sensors and actuated by magnetic suspension. The oil carries the weight of the stage while the magnetic actuators impart fine tuned forces in order to achieve 0.05 nm RMS positioning over a travel

of 100 μm in all three translational degrees of freedom. The stage in operation with a commercial STM head demonstrated atomic resolution by imaging the surface of graphite.

The Long Range Scanning (LORS) stage became the next evolution of the project. It is the focus of a Ph.D. thesis by Michael Homes under the supervision of Dr. Trumper [13]. The LORS stage exhibited a 10 fold increase in lateral range over the Angstrom Stage with 0.1 nm resolution, 1 nm repeatability, and a design goal of 10 nm accuracy. The magnetic suspension was replaced by four sets of linear motor stator windings arranged in a square. Current is passed through each winding to impart either a vertical or lateral Lorentz force onto one of four permanent magnets glued to a platen. The eight independently controlled forces allowed the instrument to independently actuate the platen all six degrees of freedom. A Zerodur reference block is mounted to the top of the platen with a kinematic mount to accept the sample. Three laser interferometers reflected off the sides of the reference block measure it x, y, and yaw while three capacitance sensors mounted on the top of the block measure z, roll, and pitch. Thus, the LORS stage operates with both non-contact metrology and non-contact actuation. The geometry and assembly of these features are shown in Figure 3-2, which is taken from Holmes's Ph.D. Thesis [13].

The Sub-Atomic Measuring Machine [34] represents the culmination of a nanometrology initiative with professors at UNCC and MIT. It uses the hardware developed in the LORS project and encompasses varied improvements in an effort to achieve nanometer accuracy metrology over long ranges. Currently, these researchers are pursuing advances in the laser interferometry system in order to reduce the noise on the position sensors. Ultimately the stage will be run in a pure helium environment, requiring a vacuum tight chamber and helium purging system. A pure helium environment ensures that the lasers propagate through a uniform medium and allows for the convection of unknown heat sources throughout the chamber. The SAMM stage performance is naturally similar to that of the LORS stage demonstrating sub-nanometer resolution, 1 nm repeatability, and 30 nm accuracy over its full range.

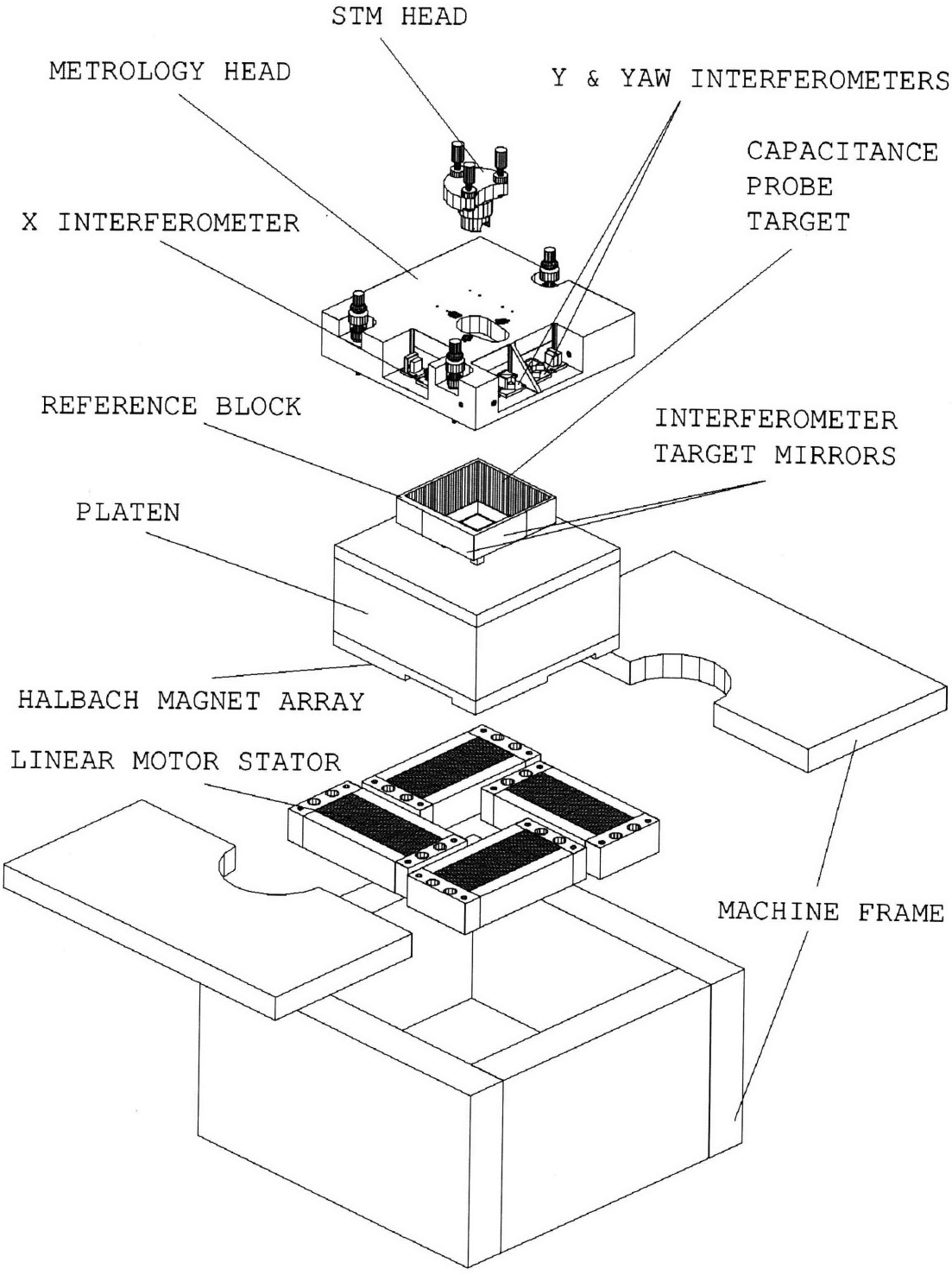

Figure 1-8: Exploded view of the LORS stage, taken from [13].

The advances in nanometrology demonstrated by the SAMM stage have given rise to the necessity of higher accuracy imaging heads. When a positioning stage equipped with an AFM or STM images a sample, the level of positional accuracy is dictated by the less accurate component. The quantization of the LORS stage's error motions were complicated by experiments that indicated the commercial STM head was simply not accurate enough to make the necessary measurements. In his master's theses [37], John Stein developed a direct metrology AFM prototype eventually intended to work in conjunction with the SAMM stage with an ultimate goal of nanometer accuracy. This AFM moved in three degrees of freedom and demonstrated a range of travel of 100 μm in X, Y, and Z directions. Many of the geometrical and material constraints were relaxed in order to demonstrate proof-of-concept. Continuing Stein's work, Aaron Mazzeo made modifications to the hardware as well as the metrological analysis and processing in order to eliminate repeatable errors thereby obtaining approximately 3 nm accuracy in the measuring of step heights [27]. The AFM head was then commissioned for a redesign that would employ the same direct metrology concept and interface with the SAMM stage.

Chapter 2

Flexures: A Quick Tutorial

A flexure is a mechanical element which allows for motion primarily through elastic deformation. A main component of this project involved designing and testing of flexure components. Design considerations included fatigue life, machinability, parasitic errors, and stiffness in the compliant and rigid directions.

2.1 Stiffness

Flexures with constant cross sections are mechanically simple devices. They are accurately modeled a by simple beam bending equations. Because much of the terminology and equations used in the thesis come from these equations, we use the next section to derive the boundary conditions and equations in detail.

2.1.1 The Simple Cantilever

The left half of Figure 2-1 depicts a single pinned beam of length l, width w, and thickness t with one end fixed to a wall at point A and the other end left free at point B. A force F_B is applied downward at point B resulting in a counter-torque at point A with a magnitude M_A equal to -Fl. The fixed end boundary condition requires that the slope of the deflection at point A remain equal to zero. The free end at point B cannot support a moment, resulting in the moment diagram shown as a function of

length.

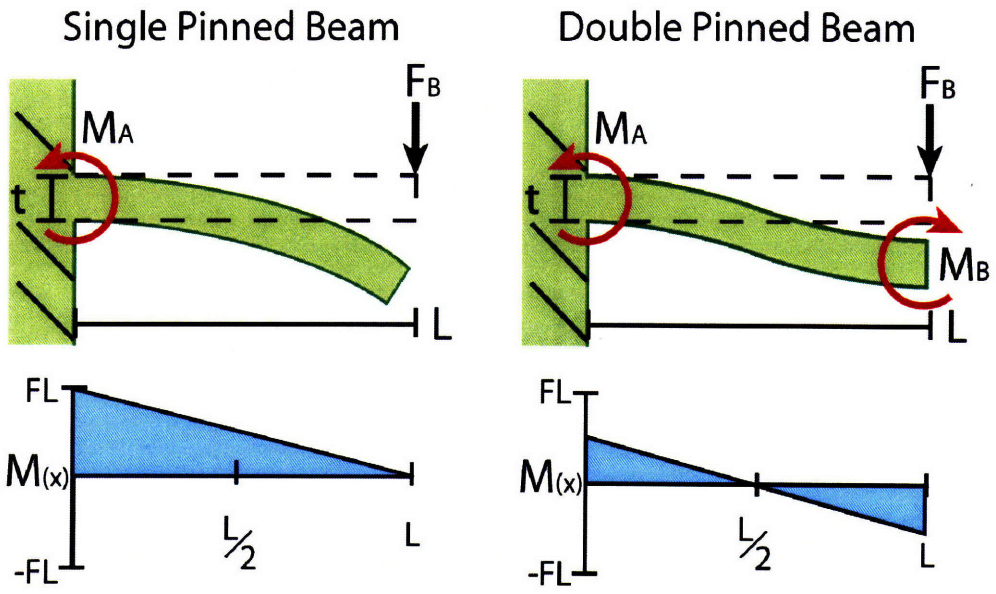

Figure 2-1: Illustration showing the applied forces, constraints, and moments within two different beams.

We divide the moment in the beam by its inertia and Young's Modulus to get the second derivative of the vertical position. We then integrate twice to get the vertical displacement of the beam as a function of the horizontal displacement.

$$y''_{(x)} = \frac{M_{(x)}}{EI} = \frac{F_B}{EI}(l - x) \tag{2.1}$$

$$y'_{(x)} = \int \frac{M_{(x)}dx}{EI} = \frac{F_B}{EI}\left(xl - \frac{x^2}{2}\right) \tag{2.2}$$

$$y_{(x)} = \iint \frac{M_{(x)}d^2x}{EI} = \frac{F_B}{EI}\left(\frac{x^2 l}{2} - \frac{x^3}{6}\right) \tag{2.3}$$

Solving for the displacement at the end of the beam, we find:

$$y_{(l)} = \frac{F_B l^3}{3EI} \tag{2.4}$$

The beam stiffness is thus given by

$$k = \frac{F_B}{y_{(l)}} = \frac{3EI}{l^3} = \frac{Ebt^3}{4l^3} \tag{2.5}$$

2.1.2 Double Pinned Beam

The next set of interesting boundary conditions will use the same beam but require that both points A and B have zero slope. The counter-torques applied at these points are non-zero under loading as well as equal and opposite. The difference in moment from point A to point B remains at the total moment applied to the beam Fl. Thus, the moment at point A equals -$\frac{Fl}{2}$ and the moment at point B equals $\frac{Fl}{2}$ leaving the moment at the center of the beam equal to zero. We solve for the displacement of the beam in the vertical direction as a function of x with the same mathematics and equations used for the previous case.

$$y''_{(x)} = \frac{M_{(x)}}{EI} = \frac{F_B}{EI}\left(\frac{l}{2} - x\right) \tag{2.6}$$

$$y'_{(x)} = \int \frac{M_{(x)}dx}{EI} = \frac{F_B}{EI}\left(\frac{xl}{2} - \frac{x^2}{2}\right) \tag{2.7}$$

$$y_{(x)} = \iint \frac{M_{(x)}d^2x}{EI} = \frac{F_B}{EI}\left(\frac{x^2l}{4} - \frac{x^3}{6}\right) \tag{2.8}$$

Solving for the displacement at the end of the beam, we find:

$$y_{(l)} = \frac{F_B l^3}{12EI} \tag{2.9}$$

The beam stiffness is thus given by

$$k = \frac{F_B}{y_{(l)}} = \frac{12EI}{l^3} = \frac{Ebt^3}{l^3} \tag{2.10}$$

From this analysis we conclude that the double pinned beam is four times stiffer than the single pinned beam. Later we will break down more complex flexures into these two simple elements in order to evaluate the stiffness of the more complex

flexures.

2.2 Parasitic Error

In motion systems there can often be undesired movement in degrees of freedom which are designed to remain constant. Parasitic errors commonly arise from mechanical coupling of two independent axis or inadequate machining tolerances. The effects of parasitic error can be minimized by implementing direct metrology or dynamically modeling the undesired movement.

2.2.1 Machining Tolerances

It is common in metallic flexures to use relatively thin components to achieve low stiffness in the desired direction of motion. This enables the flexure to attain larger displacements without approaching yield stress. As a rule of thumb in this project, no flexural component was manufactured with a thickness of less than 0.010". The waterjet, high speed mill, and wire EDM are the three most common manufacturing machines used to machine parts on this order of thickness. These three manufacturing machines have a dimensional tolerance of approximately 3, 0.5, and 0.1 thousandths of an inch respectively.

This uncertainty in dimensional tolerance can lead to systematic parasitic error. This concept can be demonstrated by studying the flexure in Figure 2-2. The body of the center of the flexure will track a straight line given that the legs have equal stiffness. The stiffness of each leg in this orientation is proportional to the cube of their thickness. Given a nominal thickness of 0.020", the flexures on the left could have a thickness of 0.017" due to the relatively loose dimensional tolerance of the waterjet. Thus, the flexures on the left would be 62% less stiff than those on the right. This would result in a systematic horizontal movement as a function of vertical position. The same flexure machined on the high speed mill or wire EDM would have a maximum discrepancy in stiffness of 7.9 and 1.5 percent respectively.

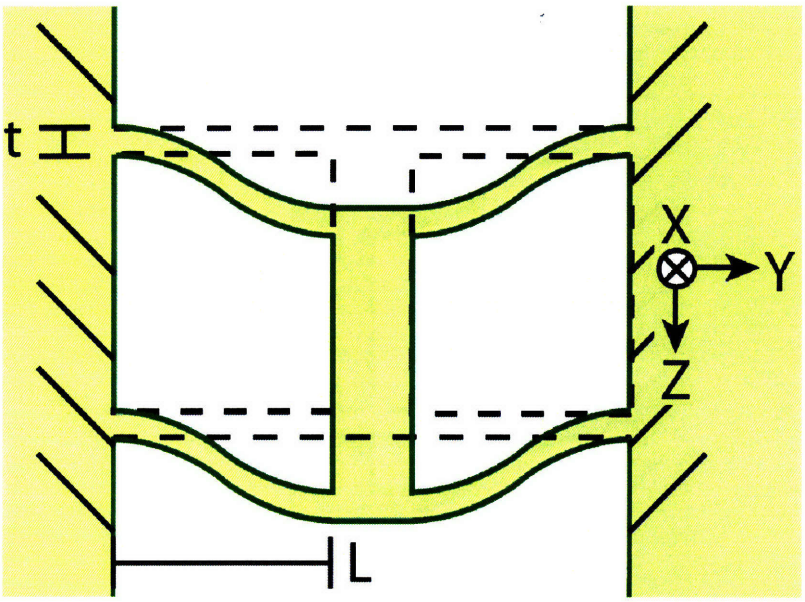

Figure 2-2: Flexure susceptible to the effects of machining tolerances.

2.2.2 Coupling of Independent Axis

Parasitic error can still be inherent in a design even if the components are made exactly to the machined specifications. A common one degree of freedom flexure is illustrated in Figure 2-3. The moving body is connected to ground by two planar flexures. Each planar flexure constrains movement in the θ_x, z, and y directions while allowing movement in x, θ_y, and θ_z. When the two flexures are added in parallel, the moving body is constrained on a first order level to move only in the x direction. The length of each flexure is conserved, causing the moving body to draw in horizontally due to movement in the vertical direction in a somewhat circular track. The parasitic error is defined by the following formula

$$\delta_x = \frac{3\delta_y^2}{5L} \tag{2.11}$$

Where δ_x is the displacement in the x direction, l is the length of the flexure, and δ_y is the parasitic error in the y direction. A more in depth derivation of this phenomenon can be found the text by Smith [36].

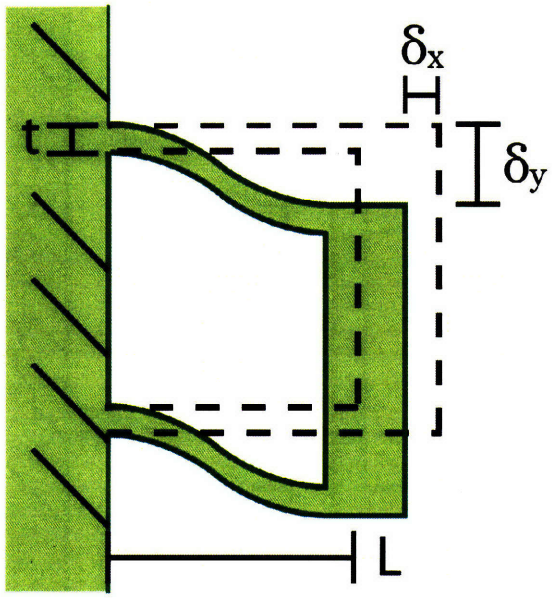

Figure 2-3: Flexure susceptible to coupling of independent axis.

2.2.3 Fatigue Life

In high speed precision motion systems it is common to expose the moving equipment to a large number of cycles. A single frequency sweep centered around 1 kHz can subject the system to over one million cycles alone. Thus, choosing the correct material and designing for low stress becomes very important to the robustness of the design. For flexural systems, the flexures must stay within the limits of elastic deformation. As a rule of thumb, the flexures should not be stressed beyond 30% of their yield stress to ensure long life stability. Regardless of the level of stress, aluminum will eventually yield after a given number of cycles while steel can last indefinitely if stressed correctly. More detailed fatigue life information can be found in the Military Handbook of Materials [1].

Chapter 3

The "Polylithic" One Degree of Freedom Acutator

The project began with the design and implementation of a simplistic one degree of freedom actuator. Its constraints and functionality were relaxed in order to focus on basic principles of mechanics and metrology.

3.1 Mechanics

The constraint principles used in the first AFM design were based on classical rod flexures. A rod is a simple flexural element providing only one constraint along its axial dimension. The core of the design in principle featured a cylindrical body held by two sets of three rods. Each set of rods were put together a radially symmetric pattern and constrained lateral and rotational movement within the plane they shared. In principle, one set of flexures would primarily constrain translational movement in x and y while the second set would constrain all rotations in θ_x, θ_y, and θ_z. Figure 3-1 shows the geometrical orientation of the cylindrical body with an overlayed theoretical structure to demonstrate the fundamental principles of constraint present in the body.

The greatest strength of the design was its manufacturability. Each set of coplanar flexural rods were cut out of a singular sheet of stainless steel on the waterjet.

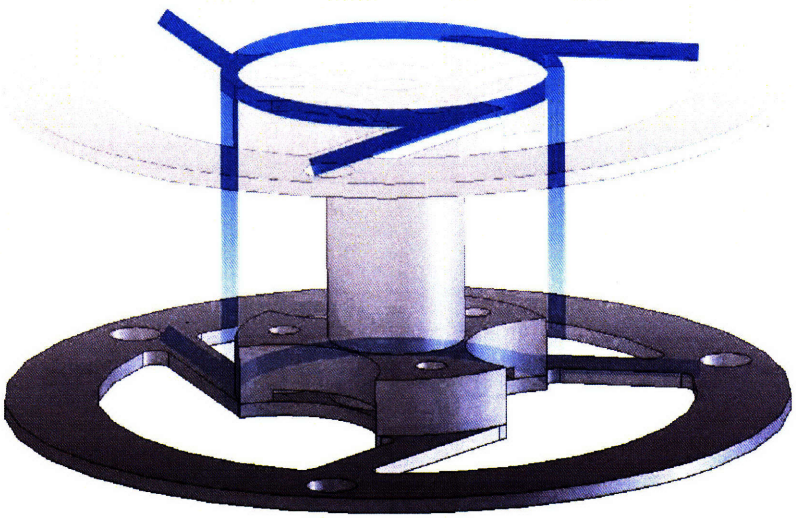

Figure 3-1: Center stage of the first actuator with a blend of theoretical constraints overlayed upon the actual hardware.

This method of manufacture also allowed us freedom to make a rectangular instead of circular cross section of the flexural beams to provide greater in plane stiffness. The thin nature of the stainless steel sheets also minimized the tapering effects of waterjet manufacturing. We required the use thin flexures in order to achieve large displacements within small geometric constraints without exceeding 30% yield stress. By cutting the flexures with the waterjet we circumvented manufacturing concerns such as unwanted vibrations in the beams as brought about by high speed milling.

The geometry of the planar sheet flexures fit into a layered design that allowed us to fit many features into a compact geometry. The geometrical cross-section of each layer was not limited in manufacturability by any other layer; a freedom that would have not been possible with a monolithic design. Each layer also featured three holes into which three bolts were fit into. These bolts provided lateral registration of the layers with respect to each other as well as a compact way to preload the stack together. Using three pins in three holes to provide lateral positioning caused over-constraint in the system. This problem can be alleviated by using more complicated but kinematically correct solution in which each layer would have featured three ra-

dially symmetric slots instead of three bolt holes. The different layers of the design are depicted in Figure 3-2 in an exploded view.

The constraint of the piezoactuator was another detail of the design that was chosen because of its mechanical simplicity in favor of absolute accuracy. Two spherical end caps were glued to the faces of the piezoactuator. The actuator was then sandwiched between two conical pits. In principle, the actuator is able to rotate in all rotational degrees of freedom. Thus, if the actuator were to tip, tilt, or twist as it elongated, the actuator would only transmit a force in the direction of actuation. In practice, frictional effects inhibit smooth rotation and instead will cause jerky microslip movements. These unpredictable movements will in turn cause jumps in the z actuation. A smoother but more cumbersome solution would use flexures that allow for a continuous engagement through angular misalignment.

The first flaw in the design was the seemingly inherent over constraint in the θ_z rotation caused by constraining five degrees of freedom with six constraints. To avoid over constraint, the redundant θ_z constraint was arranged in parallel, allowing similar movement between all flexure rods. Each rod engages the cylindrical body in a clockwise approach. Thus, a slight elongation or contraction of the flexure rods would cause an overall rotation of the center body with respect to the outer housing. Had one set of rods been oriented clockwise while the other set oriented counter clockwise the flexures would no longer be able to rotate in parallel, leading to definite over constraint. In this configuration, the flexures provide stiffness in the θ_z rotation, but at the same time allow for small perturbations in angle. We could have alleviated the amount of constraints by eliminating one of the flexure legs, but we wanted to preserve the symmetry in the design.

Although the rotation of the center body helped avoid over constraint, the presence of this undesired movement causes a fundamental angular displacement error in the positioning system. By using equation 2.11 we find that each flexure leg will contract 31.5 nm over the 20 micron range of the nanopositioner. This contraction at a radius

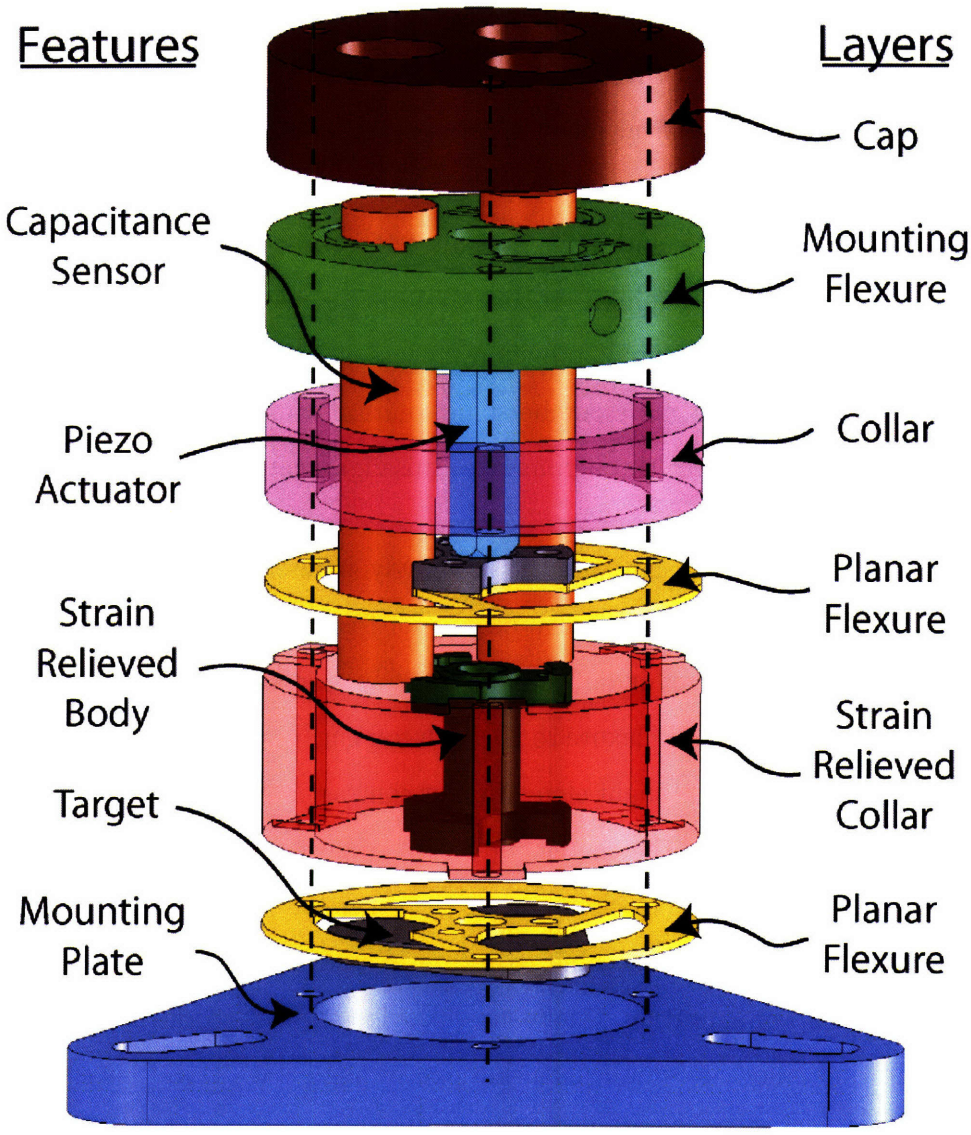

Figure 3-2: Exploded view of all the different layers and components part of the first nanopositioner.

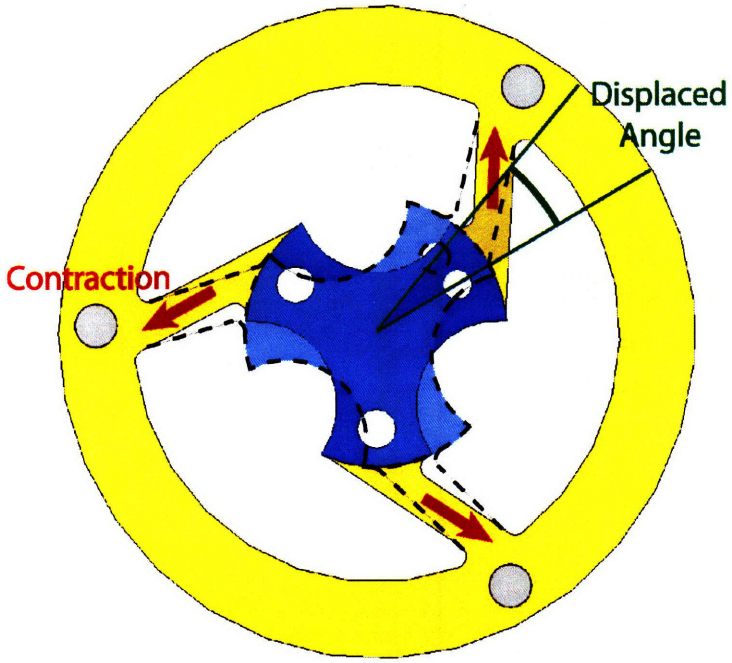

Figure 3-3: The dotted outline depicts the rotation of the center stage as a result of the flexures contracting their in plane length.

of 8.5 mm results in an displaced angular rotation of 3.6 microradians. A depiction of the center stage rotated about a displaced angle is shown with a dotted outline in Figure 3-3. Assuming that the tip of the AFM can be placed within 0.5 mm of the center of rotation, the nanopositioner would have a 1.8 nm lateral error over the full range of its travel. This undesired movement nears the boundaries of the error budget, weakening the accuracy of the positioning system.

The non-monolithic design of the nanopositioner caused further complications in the design. Each flexural beam must be pinned down on both ends to avoid microslip during movement. The clamping force of the bolts required to pin down the parts cause localized stress gradients within the part that deflect the supporting material and change over time. Reliefs had to be cut into the aluminum support layers in order to maximize the clamping pressure delivered from the screws. These reliefs are clearly shown in Figure 3-4. Furthermore, the alignment of the two flexures with respect to each other could not be kinematically determined, causing the flexures to guide the moving mass with an undefined error. The maximum estimated error in

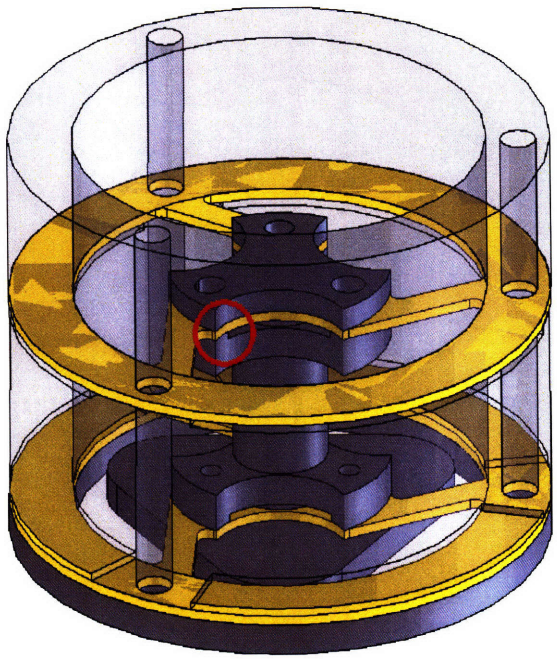

Figure 3-4: Transparent view of the nanopositioner focusing on the reliefs cut into the center stage to maximize clamping force on the flexures.

lateral positioning of the flexures with respect to each other in the assembly can range up to 0.003". This is determined by the clearance around a shoulder screw within a close fit hole. Given that the flexures are 0.75" apart, the central mass would then be guided to move with a 0.23 degree offset. Over a 20 micron range, this offset would result in a lateral positioning error of 80 nm. A monolithic design would eliminate both of these problems.

The remainder of the flaws in the design yield small, unpredictable errors. The body of the AFM head is made entirely out of aluminum which has a relatively large thermal expansion rate of 18 parts per million per degree Celsius. Aluminum was chosen for this prototype because of its ease of machining as well as its relatively low cost. In a final iteration of this design any thermal error caused by expansion can be attenuated by replacing the aluminum with Invar, thereby reducing any thermal expansion to about 1 part per million per degree Celcius.

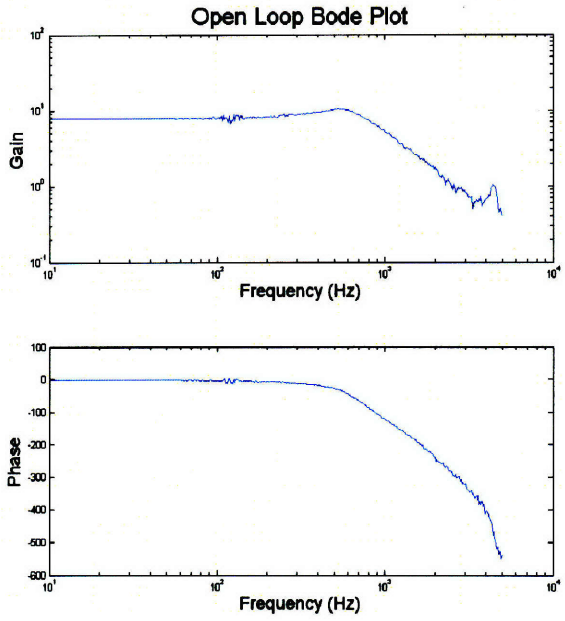

Figure 3-5: Open loop Bode plot of Input Voltage to Output Position.

3.2 Dynamics

Several basic tests were preformed on the first nanopositioner before it was retired. The first and most important of these tests was to measure the open loop Bode plot from input voltage to output position. This bode plot enabled us to characterize the electrical and mechanical effects of the system at different frequencies. The open loop bode plot for this system can be seen in Figure 3-5.

The first thing to notice about this plot is the pair of damped poles with a break-point around 550Hz. This effect is due to large signal distortion. The piezoactuator acts essentially as a capacitor. The high voltage amplifier which charges and discharges this capacitor has a limit on the amount of current it can output. This piezoactuator used in this nanopositioner (PhysikInstrumente P-885.50) can be charged up to 100V and has a capacitance of 1.5 μF. In the generation of this Bode plot, we applied a sinewave with amplitude A onto the piezoactuator. Thus the input voltage was defined by equation 3.1.

$$Voltage = A \cdot sin(\omega t) \tag{3.1}$$

We find dV/dt by taking the derivative of equation 3.1.

$$\frac{dV}{dt} = A \cdot \omega \cdot cos(\omega t) \tag{3.2}$$

In this simple circuit we find that the current is equal to the capacitance of the piezoactuator multiplied by dV/dt. Substituting in for dV/dt we find:

$$I = C \cdot \frac{dV}{dt} = C \cdot A \cdot \omega \cdot cos(\omega t) \tag{3.3}$$

With large signal distortion, the output wave becomes triangular instead of sinusoidal by keeping the current at a maximum and thus making dV/dt a constant. This effectively negates the effect of the trigonometric cosine term in the dV/dt equation pegging the value of this term as 1 or -1 at all times. Because the current limit and the capacitance will remain constant, the only variables left in the equation are ω and the amplitude. This leads to an inversely proportional relationship in which the amplitude of the output decreases as the frequency of the input signal increases thereby explaining the poles around 550Hz. In a proper electrical design the circuit will not operate in a range in which it encounters large signal distortion. This is primarily a non-linear effect that limits the bandwidth of the system but not through traditional linear control guidelines.

The next point of interest on the Bode plot is the mechanical resonance around 4.5kHz. This is attributed to the primary mode shape of the system whose frequency is numerically calculated by taking the square root of the stiffness divided by the moving mass. We identify this as a resonant peak by the jump in magnitude as well as a loss of 180 degrees in phase. This resonance is of primary concern when evaluating the stability of the loop. In one experiment, rubber was added in series with the moving mass in order to increase the damping of this mechanical resonance and thus decrease the magnitude of its peak. It was found that although the stiffness decreased and consequently lowered the resonant frequency, the addition of the rubber

was successful in decreasing the magnitude of the resonant peak.

Lastly, we notice another non-linear effect by observing the phase of the Bode plot. Electrical and mechanical effects have thus far introduced four poles into the system. If each pole adds 90 degrees of phase, we should not observe less than 360 degrees of phase. The bode plot clearly marks less than 500 degrees of phase at 5 kHz. This loss of phase is due to the fact that we are converting the analog signals into a digital domain which employ a zero order hold between samples. This in turn adds a time delay equivalent to one half of the inverse of the sampling frequency. On a logarithmic plot we see the effect upon the phase is negligible for small frequencies and completely dominating for large frequencies for the phase lag added by a time delay increases linearly with frequency. With a target crossover frequency of 200 Hz, we find that the addition of phase in the kHz range from the discrete time sampling is negligible.

Chapter 4

Design and Construction of the Monolithic Flexure

The main mechanical design contribution of this thesis is the design and fabrication of the monolithic one degree of freedom flexure. This chapter begins by detailing the reasoning and calculations behind the choices that define the flexure. The results of the theoretical and experimental testing are then presented. Lastly, a detailed look at the fabrication process of the flexure is laid out.

4.1 Radial to Axial Stiffness Ratio

The steel flexures used in the atomic force microscope are designed to guide the stage in one degree of freedom. We rely on the SAMM stage to provide movement in the remaining X and Y translational motions. Four different designs were proposed over the development of the flexure. This chapter compares the performance of the four designs. The numerical values used in the following calculations reflect the dimensions of the prototype flexure whose flexural beams were not curved, making it manageable to mathematically evaluate its characteristics without the necessity of finite element analysis. The dimensions of the prototype as well as its physical properties used in these calculations are found in Table 4.1.

Parameter	Symbol	Numerical Value
Thickness	t	0.635mm
Width	b	5.08mm
Length	L	5.85mm
Young's Modulus	E	70 GPa
Density	ρ	2700 $\frac{kg}{m^3}$

Table 4.1: Numerical Values of Physical Properties selected for Aluminum Prototype Flexure

4.1.1 Performance Criterion

Before comparing the performance of the four flexures it is important to first define the performance criterion. The flexure is designed to allow linear translation in the vertical direction and resist lateral movement. To simplify the nomenclature of this ultimately cylindrical design, we define a co-ordinate system in which vertical movement of the stage in the z-direction is referred to as "axial," while horizontal movement in either x or y direction is referred to as "radial." For notation purposes of this analysis, we define the Z direction to run up and down the page while Y runs left to right and X goes in and out. Thus, the main performance criterion of the flexure is the ratio of radial stiffness to axial stiffness. Although the term "radial" groups together the x and y characteristics, the radial stiffness of the flexure is proportional to the minimum of the x or y stiffness. We also rate the performance of the flexures based on intrinsic design flaws they may have such as parasitic errors or overconstraint.

4.1.2 The Four Bar Link

The four bar link consists of a stage guided by two planar flexures. This geometry holds the stage perpendicular to the base through its travel as would a four bar linkage. As touched upon in subsection 2.2.2, the stage will also exhibit a parasitic error in the y direction as a function of the z displacement which severely compromises the performance of the flexure. Otherwise, the stage exhibits good radial stiffness as

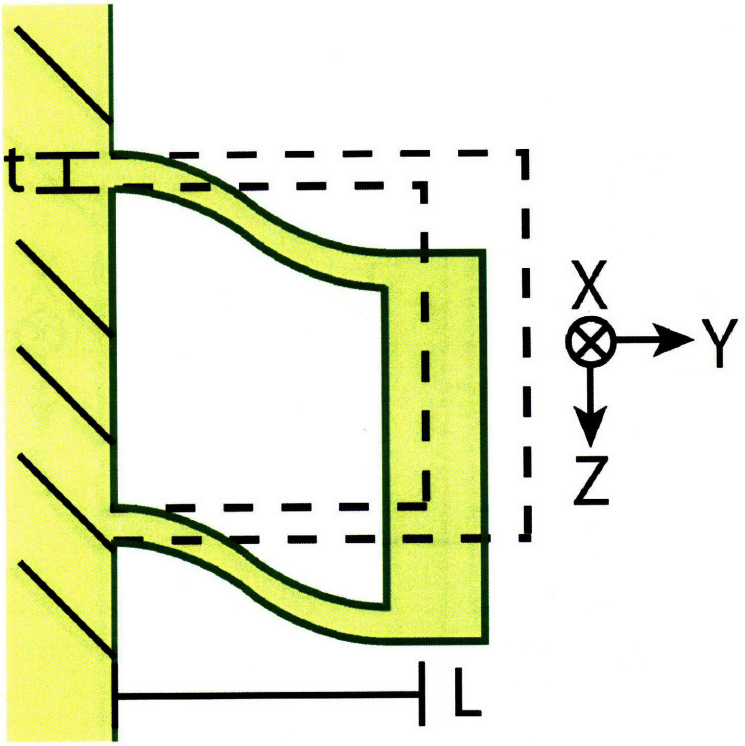

Figure 4-1: Cross-Sectional Sketch of the Four Bar Link Flexure

defined below:

$$k_x = \frac{3EI_{xx}}{L^3} = 2 \cdot \frac{Eb^3t}{4L^3} = 14.6\frac{N}{\mu m} \tag{4.1}$$

$$k_y = \frac{EA_{xy}}{L} = 2 \cdot \frac{Ebt}{L} = 77.3\frac{N}{\mu m} \tag{4.2}$$

The axial stiffness of the flexure is defined by:

$$k_z = \frac{12EI_{zz}}{L^3} = 2 \cdot \frac{Eb^3t}{L^3} = 0.913\frac{N}{\mu m} \tag{4.3}$$

It is important to note that the boundary conditions used to calculate k_z and k_x are different. When the stage is displaced in the z direction, both ends of the flexures are mechanically held at zero slope. Conversely when the stage is displaced in the x direction, the free end of the flexure not mounted to mechanical ground is free to bend. In this geometry we find that k_x is much less than k_y leading us to estimate

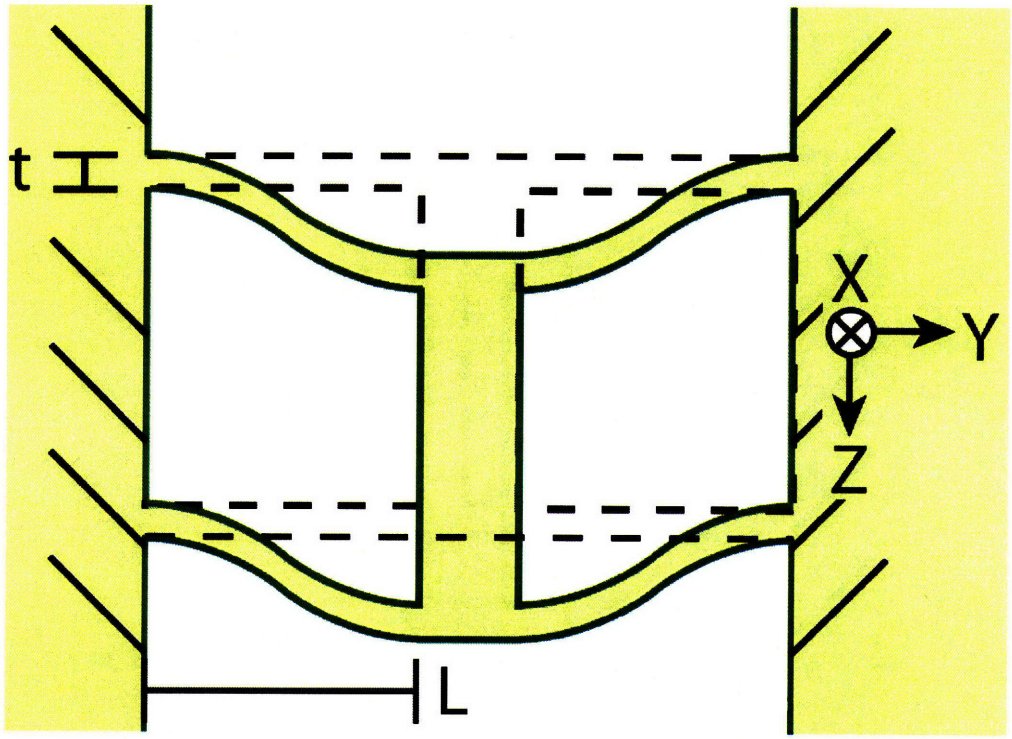

Figure 4-2: Cross-Sectional Sketch of the Single Beam Flexure

the radial to axial stiffness ratio as

$$\frac{k_{rad}}{k_{axial}} = \frac{Eb^3t}{2L^3} \cdot \frac{L^3}{2Ebt^3} = \frac{b^2}{4t^2} = 16.0 \tag{4.4}$$

4.1.3 Single Beam Flexure

The single beam flexure uses four linkages to guide a central stage. This flexure can be visualized as two four bar links connected back to back. This flexure exhibits better radial stiffness and minimized parasitic error as compared to the four bar link. The main downfall of this design is its fundamental over-constraint. Both four bar links will want to pull the stage toward their mechanical ground as the stage moves in the z direction. This fight for position will increase the nominal z stiffness. The nominal z stiffness is defined by:

$$k_z = 4 \cdot \frac{12EI_{xx}}{L^3} = \frac{4Ebt^3}{L^3} = 1.83\frac{N}{\mu m} \tag{4.5}$$

To calculate the resultant z stiffness, we begin by calculating the change in length of each member as a function of the z displacement:

$$\delta_x = \frac{3\delta_z^2}{5L} \tag{4.6}$$

The stretching of each member by δ_x will make rise to a tensile force in the member:

$$F_{tensile} = \frac{EA\delta_x}{L} = \frac{3EA\delta_z^2}{5L^2} \tag{4.7}$$

We estimate that the tensile force is colinear with the member. Thus, the component of the tensile force in the z direction is given by:

$$F_{tensile_z} = F_{tensile} \cdot tan\left(\frac{\delta_z}{L}\right) \approx F_{tensile} \cdot \frac{\delta_z}{L} = \frac{3EA \cdot \delta_z^3}{5L^3} \tag{4.8}$$

$$k_z = \frac{F_z}{\delta_z} = \frac{3EA \cdot \delta_z^2}{5L^3} \tag{4.9}$$

We then combine the nominal stiffness with the tensile stiffness to obtain the resultant stiffness:

$$k_z = k_{nominal} + 4k_{tensile_z} = \frac{48EI_z z}{L^3} + \frac{12EA \cdot \delta_z^2}{5L^3} = \frac{EBt}{L^3}\left(4t^2 + \frac{12}{5}\delta_z^2\right) \tag{4.10}$$

In our instrument, t = 0.030" and δ_z = 0.005" thereby making $t^2 \gg \delta_z^2$. Thus, we find that the increase in stiffness in negligible for our purposes. Although the stiffness does not pose a fundamental problem for our relatively short strokes, this overconstraint leads to an undesirable phenomenon called "oil-canning." With shifts in temperature and stress, the overconstrained system can develop a bi-stable state in which the overconstrained nature of the moving element can lock it into one of two different low energy states. This change in state is erratic and hysteretic, two qualities that we try to preclude from any precision motion system.

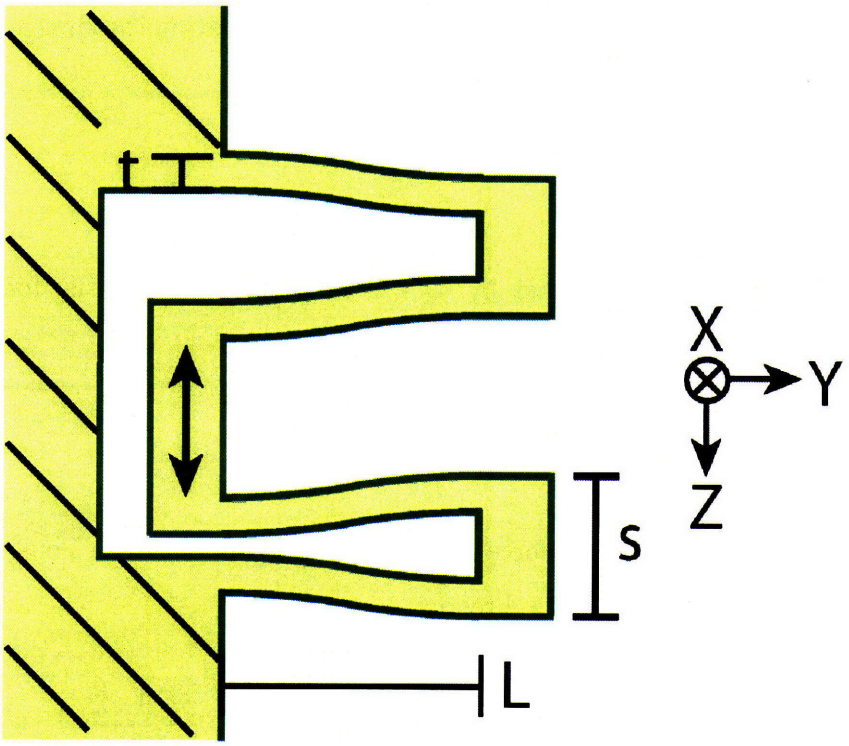

Figure 4-3: Cross-Sectional Sketch of the Crab-Leg Flexure

Continuing with the analysis, we find the single beam flexure has relatively high radial stiffness:

$$k_x = 4 \cdot \frac{12EI_{xx}}{L^3} = \frac{4Eb^3t}{L^3} = 117\frac{N}{\mu m} \tag{4.11}$$

$$k_y = \frac{EA_{xy}}{L} = 4 \cdot \frac{Ebt}{L} = 154\frac{N}{\mu m} \tag{4.12}$$

Finally, we calculate the axial to radial stiffness ratio as

$$\frac{k_{rad}}{k_{axial}} = \frac{4Eb^3t}{L^3} \cdot \frac{L^3}{4Ebt^3} = \frac{b^2}{t^2} = 64.0 \tag{4.13}$$

4.1.4 Crab-Leg Flexure

The crab leg flexure guides the mass with a two sets of doubled-back flexural beams. This flexure not only minimizes parasitic errors but also alleviates the overconstraint

present in the single beam flexure. The main drawback of this flexure is its weak k_y. This is fundamentally different from the previous flexures whose k_y was three and ten times greater than k_x respectively. To calculate this effect, we impart a load on the stage in the y direction. This in turn creates a z-moment through the entire flexure with a magnitude of the force times the radius arm, s. Though beam bending equations we find that the slope of the flexure at the end of the beam:

$$x'' = \frac{F_y \cdot s}{EI} \tag{4.14}$$

$$x'|_{x=L} = \frac{F_y \cdot s \cdot L}{EI_{zz}} \tag{4.15}$$

The displacement of the stage in the y direction is given by sin(x') multiplied by the lever arm, s. Assuming small angles, we solve for the deflection in the y direction and thus the stiffness in the y direction:

$$\delta_y = s \cdot sin\left(x'\right) \approx s \cdot s' = \frac{F_x \cdot s^2 \cdot L}{EI_{zz}} \tag{4.16}$$

$$k_y = \frac{F_x}{\delta_x} = \frac{EI_{zz}}{s^2 L} = 4 \cdot \frac{Ebt}{12L} \cdot \left(\frac{t}{s}\right)^2 = 0.838 \frac{N}{\mu m} \tag{4.17}$$

This stiffness calculation clearly demonstrates the importance of minimizing s. Geometrically, s can not be smaller than 2t. Practically, s will equal 2t plus the diameter of the wire or endmill used to cut the slot between the two flexure blades. Constrained by the limit in which endmills can only cut five times deeper than their diameter, we used a 3/64" endmill to cut the 12/64" deep slot. Had we been able to use wire EDM, the slot diameter could have been reduced to 1/128" or eight thousandths of an inch nearly halving s.

The theory predicts relatively weak radial stiffness in this flexure due to lack of a zero slope boundary condition on the free ends of the flexure. This effect can best be visualized by looking at Figure 4-4 which uses FEA to show the deflection of the flexures when a radial load is applied to the center stage.

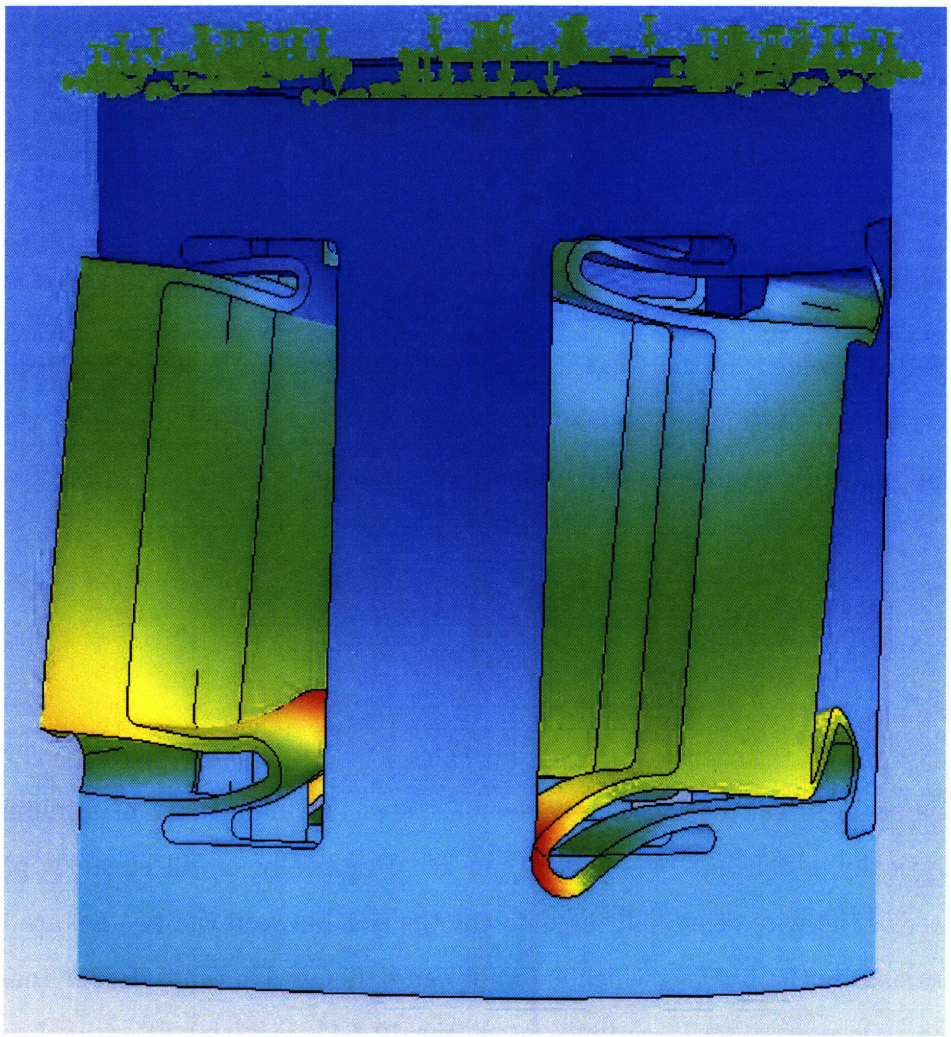

Figure 4-4: This picture uses FEA to show the displacement of the crab-leg flexure when it is radially loaded.

The remaining stiffness calculations for the crab leg flexure are primarily adopted from the four bar link. The primary difference between the two geometries is that the crab-leg flexure doubles back, acting like two springs in series. This in turn halves k_x:

$$k_x = \frac{k_{x\,fourbar}}{2} = \frac{Eb^3t}{4L^3} = 7.3\frac{N}{\mu m} \tag{4.18}$$

Similarly we can calculate the axial stiffness k_z by dividing the four-bar link axial stiffness in half:

$$k_z = \frac{k_{z\,fourbar}}{2} = \frac{Ebt^3}{L^3} = 0.456\frac{N}{\mu m} \tag{4.19}$$

This calculation for k_z is not completely accurate because it is based on a zero slope boundary condition at the free end of the flexure. As we have witnessed in the derivation of k_y, this boundary condition does not hold true for the crab-leg flexure. Using FEA analysis, we found the expected value of k_z to be 0.228 $\frac{N}{\mu m}$, or one half of the stiffness calculated with a zero slope boundary condition.

Lastly, we calculate the radial to axial stiffness which is an order of magnitude lower than the previous flexures.

$$\frac{k_{rad}}{k_{axial}} = 4 \cdot \frac{Ebt}{24L}\left(\frac{t}{s}\right)^2 \cdot \frac{L^3}{Ebt^3} = \frac{2L^2}{3s^2} = 3.67 \tag{4.20}$$

The radial to axial stiffness ratio has an undesirable proportionality to L^2. We would like to leave the length of the flexure as an independent variable set by the target axial stiffness. Coupling these two performance specifications forces us to make trade-offs between the axial to stiffness ratio and the target axial stiffness.

4.1.5 Final Flexure

The final flexure design combines the all the advantages of the previous four flexures with minimal drawbacks. The design minimizes parasitic error while exhibiting correctly constrained movement and respectable radial stiffness. To do so, we start with a crab leg flexure and then add a beam that connects the two free ends as seen in

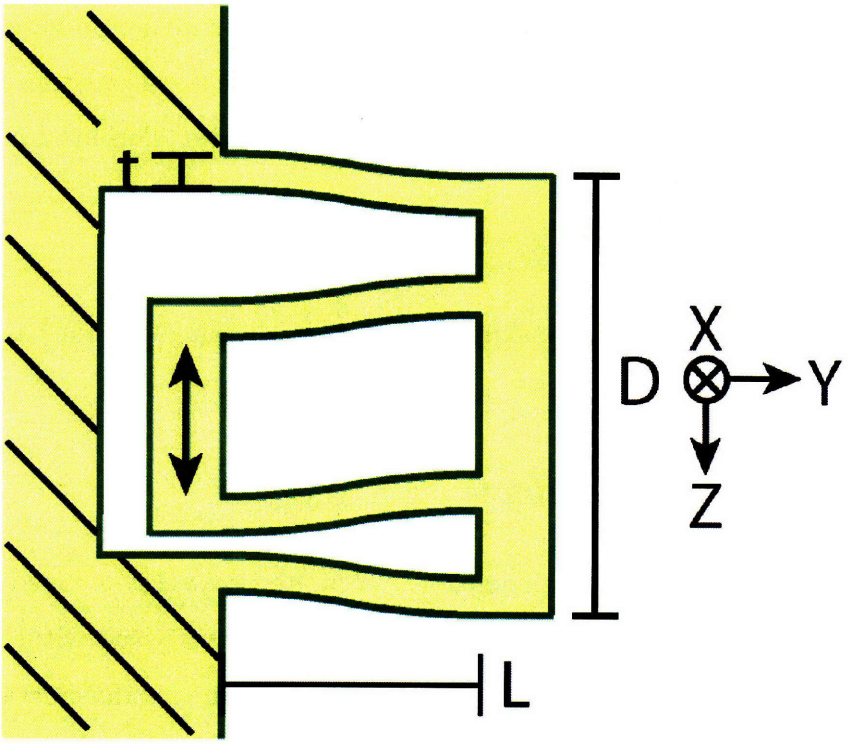

Figure 4-5: Cross-Sectional Sketch of the Final Flexure

Figure 4-5. This beam restores the zero slope boundary condition absent in the crab leg flexure and present in the four bar link resulting in the following stiffnesses:

$$k_z = \frac{k_{zfourbar}}{2} = \frac{Ebt^3}{L^3} = 0.456\frac{N}{\mu m} \tag{4.21}$$

$$k_x = \frac{k_{xfourbar}}{2} = \frac{Eb^3t}{4L^3} = 7.3\frac{N}{\mu m} \tag{4.22}$$

$$k_x = \frac{k_{xfourbar}}{2} = \frac{Ebt^3}{L^3} = 38.7\frac{N}{\mu m} \tag{4.23}$$

Given that each of these stiffnesses is the same given fraction of the four bar link stiffnesses, the radial to axial stiffness ratio remains the same as before;

$$\frac{k_{radial}}{k_{axial}} = \frac{Eb^3t}{2L^3} \cdot \frac{L^3}{2Ebt^3} = \frac{b^2}{4t^2} = 16.0 \tag{4.24}$$

The radial to axial stiffness ratio of the final flexure has no dependence on length

and is 4.5 times larger than the crab-leg flexure. The main drawback of this design is the frequency domain stability of the flexure. The bar which connects the two free ends of the crab leg flexure acts as a free mass whereby it can move independently of the stage and mechanical ground. This free mass has an excitable mode defined by its stiffness and mass. If the frequency of this excitable mode is close to the bandwidth of our system it has the potential to drive the entire system unstable. We first calculate the total stiffness of the combined four beams:

$$k_z = \frac{12EI_{zz}}{L^3} = 4 \cdot Ebt^3/L^3 = 1.83\frac{N}{\mu m} \tag{4.25}$$

Secondly we calculate the volume of the free mass. This leads to an optimization trade-off. Adding the thickness of the free mass will increase the radial stiffness of the flexure but will also add mass. Through FEA we found that increasing the thickness of the free mass over five times the thickness of the flexure began to give negligible changes in radial stiffness. This ratio cannot be used as a firm guideline because it heavily depends on the distance between the two flexures, D. Given our geometry, we calculate the volume of the free mass to be:

$$V = 5t \cdot b \cdot D = 396mm^2 \tag{4.26}$$

Using the density of aluminum we can find the natural frequency of the excitable mode. For simplicity we omit the mass of the flexures.

$$\omega_n = \frac{1}{2\pi}\sqrt{\frac{k}{\rho V}} = 6.6kHz \tag{4.27}$$

Given that we plan to operate our AFM below 1 kHz, we found this to be an acceptable tradeoff between radial stiffness and natural frequency.

4.2 Theoretical Results

The purpose of this short section is to present the results of the flexure analysis in a compact form using normalized values. The main performance criterion derived in

Table 4.2: This table holds the results of the theoretical calculations on the four different proposed flexures.

	Four-Bar	**Single Beam**	**Crab-Leg**	**Final**
Axial Stiffness	$\frac{2Etb^3}{L^3}$	$\frac{4Ebt^3}{L^3}$	$\frac{Ebt^3}{L^3}$	$\frac{Eb^3t}{2L^3}$
Radial Stiffness	$\frac{Eb^3t}{2L^3}$	$\frac{4Eb^3t}{L^3}$	$4 \cdot \frac{Ebt}{24L}\left(\frac{t}{s}\right)^2$	$\frac{2Ebt^3}{L^3}$
R/A Parameter Ratio	$\frac{b^2}{4t^2}$	$\frac{b^2}{t^2}$	$\frac{2L^2}{3s^2}$	$\frac{b^2}{4t^2}$
R/A Numerical Ratio	16	64	3.67	16
Main Drawback	Parasitic Error	Over-Constrained	Weak R/A Ratio	Free Mass

the previous chapter for each of the four flexures can be found in Table 4.2.

4.3 Experimental Results

After machining the flexures we physically tested the hardware to measure the axial and radial stiffness. This test was preformed by loading the flexure with a measured mass and then measuring the resultant displacement with a capacitance sensor. The flexure was first loaded axially with a capacitance sensor positioned parallel to the bottom of the moving stage. The flexure was then turned on its side and loaded radially as a capacitance sensor measured the curved face between two opposing mirror imaged crab leg flexures. We estimated that the curvature of this face would not significantly impact the capacitance sensor measurement based upon the radius of the flexure and the diameter of the capacitance sensor. The theoretical and experimental results for the aluminum prototype flexure seen as a CAD model on the left half of Figure 4-6 and in the digital picture on the right half are given below.

The prototype flexural system incorporated three pairs of crab leg flexures. Each pair of flexures was symmetrically mirrored around a three legged center stage. The

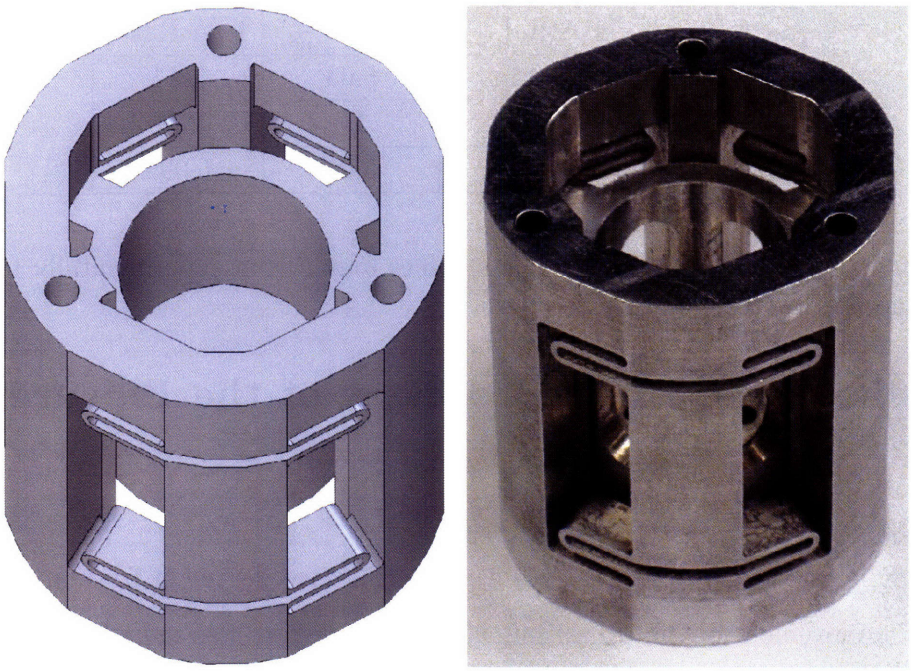

Figure 4-6: Side by side view of the CAD model and a picture of the machined flexure taken with a digital camera.

theoretical stiffness of the flexural system is equal to six times the stiffness of one flexure because all six flexures bend in parallel.

$$k_{axial} = 6 \cdot k_{z\,Prototype} = 1.37 \frac{N}{\mu m} \tag{4.28}$$

$$k_{radial} = 6 \cdot k_{z\,Prototype} = 5.03 \frac{N}{\mu m} \tag{4.29}$$

As described in the previous chapter, we found through FEA that the zero slope boundary conditions on the free end of the crab leg flexure were not upheld causing a decrease in both axial and radial stiffness. The expected FEA values as well as the measured experimental values are given in Table 4.3.

Source	Axial $\frac{N}{\mu m}$	Radial $\frac{N}{\mu m}$	R/A Ratio
Theoretical	2.74	5.03	1.84
FEA	1.47	3.3	2.25
Experimental	0.83	5.05	6.092

Table 4.3: This table holds the stiffness values found from experimentally testing of the aluminum prototype flexure.

4.4 Manufacturing Processes of the Flexure System

The atomic force microscope utilizes a monolithic one degree of freedom flexure to guide the movement of the tip sensing stage. The flexure was manufactured using a combination of high speed milling and wire EDM processes. The large, periodic forces inherent in high speed milling make it difficult to accurately and cleanly manufacture thin walled parts because of the excitement of vibratory modes within the structure. The manufacturing process of the flexure system was tailored to address this problem.

The design of the flexure underwent a series of iterations before settling on the final geometry. The first design served mainly as a proof of concept. Six pairs of crableg flexures were machined into each face of a hexagonal extrusion. The flexure elements themselves were made to be relatively simplistic although their integration into a monolithic piece posed challenges in manufacturing. Each element has a two dimensional cross section that does not change with the depth of cut. Using this geometry allowed the flexure to be manufactured by simple pocketing operations on a three axis mill with conventional square end endmills. The setup of the pocketing operation left a solid core of metal at the base of each pass. Thus, the thin walled flexure always had one end that was pinned during the milling process. This mechanical attachment eliminated low frequency excitations of the flexural beams commonly called "chatter." Chatter can excite the free end of the machined body into vibration during the machining process and lead to bad surface finish and tolerancing. It is very difficult to avoid excitement of a mode because the natural frequency of the flexure

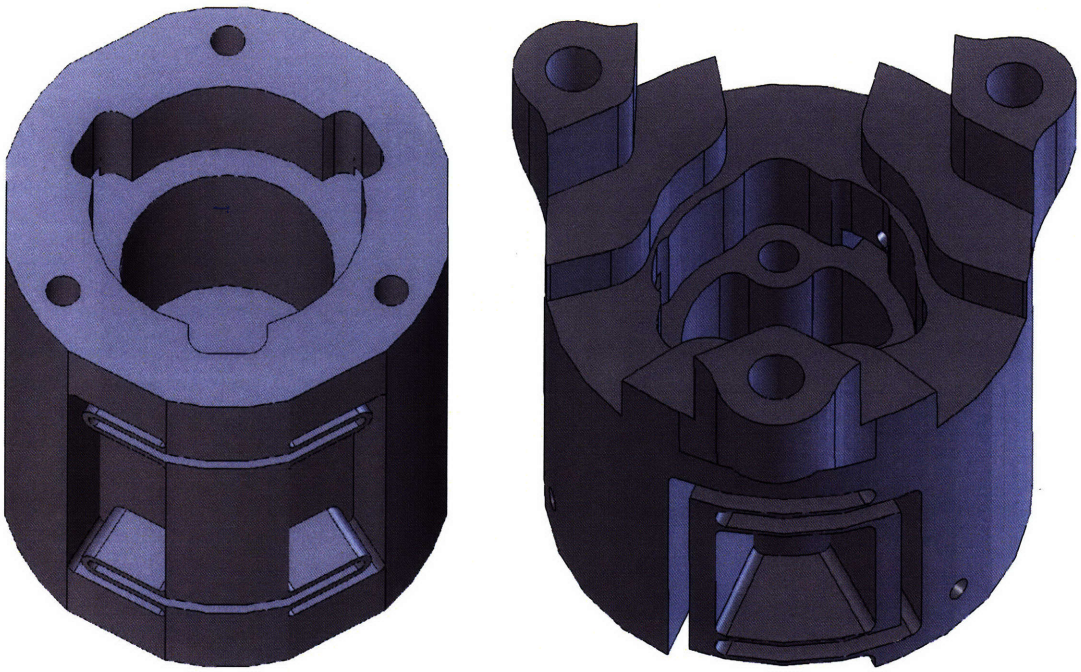

Figure 4-7: Snapshot of the two flexures before the wire EDM process.

will change as the flexure is being cut. Also, the impulses imparted on the body by the cutting tool will not only excite modes at the spindle speed, but also at multiple or harmonic frequencies of the spindle speed. Figure 4-7 shows the proof of concept and final flexures after the end milling process.

The pinned end of the flexure was then cut free by wire EDM in order to avoid exciting vibratory modes. The wire EDM process erodes a thin line through the work piece by discharging current from a continuously fed through wire. The forces on the work piece are relatively small and do not damage or deflect the thin flexures. Figure 4-8 shows the cross-sectional area removed by the wire EDM process.

The final design incorporated a more complex flexure system. The flexures shifted from a constant cross-sectional design to a radially symmetric curved geometry. The manufacturing of these more complex features required the use of a four axis mill but was still processed in the same manner as the first flexural system. Finally, Figure 4-9 shows the freed flexures after all machining processes have been completed.

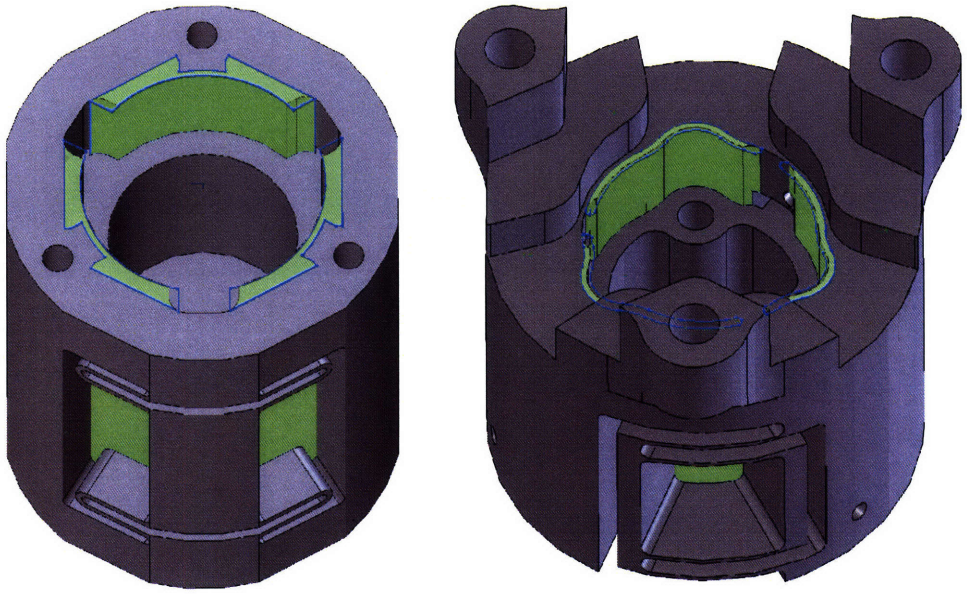

Figure 4-8: The highlighted sections in this picture show the area removed by the wire EDM process.

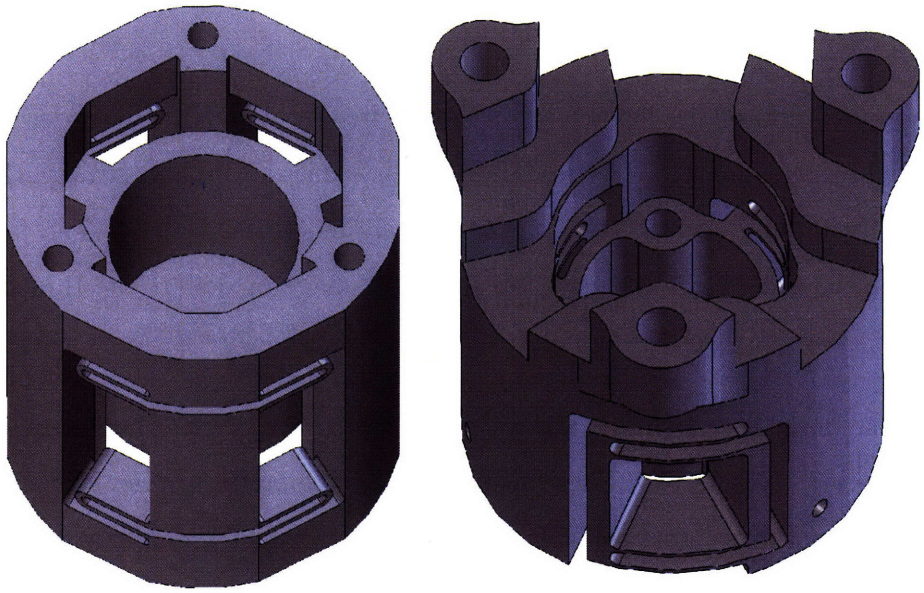

Figure 4-9: The final product after the wire EDM operation.

Chapter 5

Error Budgeting

The purpose of this thesis is to create a nanopositioner with subnanometer accuracy. We have focussed on evaluating and eliminating mechanical and thermal errors that lead to inaccuracies. This chapter presents the results of the error budgeting analysis.

5.1 Mechanical Error Budget

The goal of the project was to design a one degree of freedom stage with nanometer scale accuracy. Because the instrument can only measure the deflection of the stage in the direction of travel, the mechanical design must guarantee that the stage remain within the specified error budget in the remaining degrees of freedom through the mechanical design.

Although the piezoactuator primarily extends in an axial direction, it will have second order undesired motions causing it bend, twist, and shear. The objective of the flexural system is to inhibit the transmission of these error motions from the piezoactuator into the moving stage. We first must estimate the bounds of the error motions before calculating their effects. Figure 5-1 shows exaggerated piezoactuator error motions in order to visualize the different types of positional error. Given a 20 micron range of movement in z, we estimated that the piezoactuator was capable of shear movement resulting in a one micron displacement in either x or y. We also

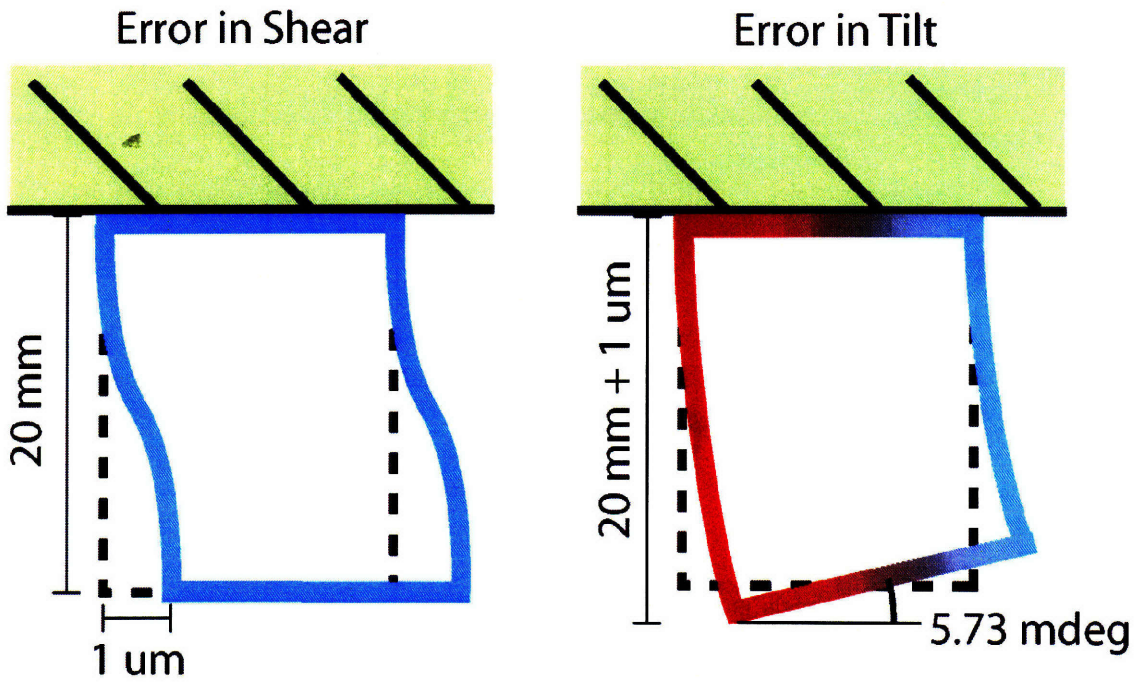

Figure 5-1: Depiction of lateral frictional forces arising from a normal preload force.

estimated that, in cross section, there could be a once micron discrepancy in length between the left and right walls. This one micron difference over a 20 mm base would cause a tilt of 5.73 millidegrees in θ_x or θ_y.

The atomic force microscope uses two flexures whose stiffnesses in their respective degrees of freedom opposite relative to eachother. The decoupling flexure is designed to provide stiffness in the z direction and relative compliance in all other degrees of freedom while the stage flexure is designed to provide compliance in the z direction and relative stiffness in all other degrees of freedom. The relative stiffness between the decoupling and stage flexures permits only a small fraction of the undesired motions piezoelectric error motions to be transmitted into the moving stage. Figure 5-2 shows an overview picture of both flexures while Table 5.1 gives their physical dimensions and properties.

To achieve angular and shear compliance in the decoupling flexure, four flexure

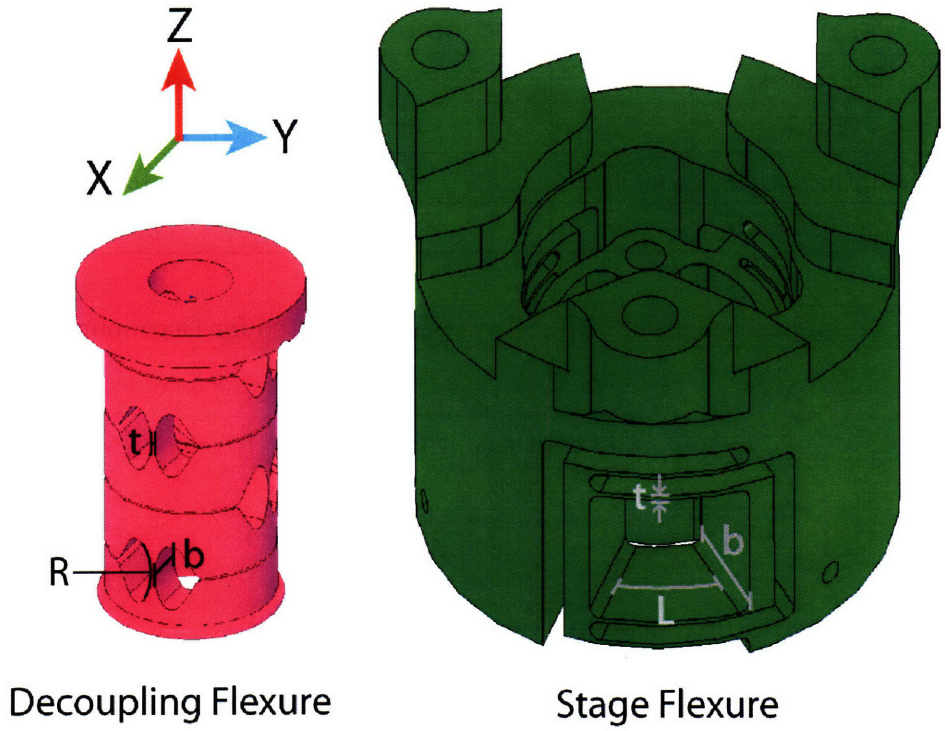

Figure 5-2: Picture of the two flexures used in the AFM in relative proportion.

hinges were cut perpendicular to each other by wire EDM into a cylinder of steel. The angular stiffness of each hinge is defined by the equation (5.1).

$$k_{M\theta} = \frac{M_z}{\theta_z} = \frac{2Ebt^{5/2}}{9\pi R^{1/2}} = 1.45\frac{N \cdot m}{rad} \tag{5.1}$$

where R = Radius of curvature

t = Thickness

E = Young's Modulus

and b = Width

The side slit in the decoupling flexure was cut with a wire EDM, cutting the slot at 0.006" thickness limiting the hinge to $\pm$ 0.73 degrees of rotation. The stress in the hinge is defined by equation (5.2).

$$\sigma = \frac{6 \cdot k_{M\theta} \cdot \theta}{bt^2} \tag{5.2}$$

Parameter	Symbol	Decoupling Flexure	Stage Flexure
Thickness	t	0.254mm	0.381mm
Width	b	6mm	7.81mm
Length/Radius	L or R	4mm	10.5mm
Young's Modulus	E	210GPa	210GPa

Table 5.1: Numerical Values of Physical Properties selected for Decoupling and Stage Flexures.

Direction	Stiffness
Z	18 $\frac{N}{\mu m}$
X	0.033 $\frac{N}{\mu m}$
Y	0.033 $\frac{N}{\mu m}$
θ_x	0.75 $\frac{Nm}{rad}$
θ_y	0.75 $\frac{Nm}{rad}$
θ_z	23.6 $\frac{Nm}{rad}$

Table 5.2: Stiffness of the decoupling flexure in all six degrees of freedom.

Using these equations, we find that the stress in the flexure is limited to 296 MPa before the flexure hits a hard stop. This safeguards the flexure by limiting the stress to 43% of the yield stress at its maximum deflection. We use Hooke's Law to estimate the stiffness of the decoupling flexure in the z direction. Although the flexure beams are very thin, they achieve high stiffness when being loaded in compression or tension. We use equation 5.3 to calculate an estimate of the stiffness of each flexural element.

$$k_z = \frac{F}{x} = \frac{EA}{L} = \frac{Ebt}{L} = 80\frac{N}{\mu m} \tag{5.3}$$

The decoupling uses four flexures in series, each with a stiffness of $80\frac{N}{\mu m}$. Thus, the entire decoupling flexure has a k_z of 20 $\frac{N}{\mu m}$ from our calculations. This figure matched up well with our FEA analysis which estimated the k_z for this flexure to be 18 $\frac{N}{\mu m}$. Lastly, we compile the stiffnesses we calculated from equations 5.1 and 5.3 along with the FEA predictions in Table 5.2.

Direction	Stiffness
Z	1.0 $\frac{N}{\mu m}$
X	56 $\frac{N}{\mu m}$
Y	56 $\frac{N}{\mu m}$
θ_x	2.0 $\frac{kNm}{rad}$
θ_y	2.0 $\frac{kNm}{rad}$
θ_z	1.8 $\frac{kNm}{rad}$

Table 5.3: Stiffness of the stage flexure in all six degrees of freedom.

Direction	Error Piezo	Ratio	Error Stage
X or Y	1.0 μm	1690	0.59nm
θ_x or θ_y	100 μrad	2670	37.5 nrad
θ_z	1 μrad	77.2	13.0 nrad

Table 5.4: Numerical Values of Physical Properties selected for Prototype Flexure

Secondly, we must calculate the stiffness in each degree of freedom of the stage flexure. Again, the purpose of this flexure is to provide compliance in the z direction and rigidity in every other degree of freedom. Because of the complicated geometry of the stage flexure, we rely on FEA to calculate the stiffness values. These values are found in Table 5.3.

Lastly, we evaluate the worst case error motion transmitted into the stage from the piezoactuator by deamplifying the error motions by the ratio between the decoupling and stage flexure stiffness in any given direction. Here we find that the worst case error motions are within our 1nm mechanical error budget. The results of this calculation are found in Table 5.4.

5.2 Thermal Error Budget

Thermal expansion of materials becomes a very important issue when working with macroscale components that require nanoscale thermal stability. A pendulum clock

is a fine example of such a system. The period of a pendulum is defined by the square root of gravity divided by the length of the pendulum. If a one meter long steel pendulum designed to operate in 25°C weather was placed in a 0°C environment, the length of the pendulum would contract by 0.3mm. This change in length would increase the frequency of oscillation by 0.015%, subtracting 13 seconds from every day the clock counted time. To counteract this change in length, accurate clocks are designed to be thermally balanced. One approach is the gridiron pendulum which has spans of brass and steel that thermally expand in opposite directions, canceling out the overall expansion of the pendulum as seen in Figure 5-3 taken from [42]. Although this balanced design attenuates the effect of temperature on length, there can exist thermal gradients within the gridiron that contribute to second order changes in length.

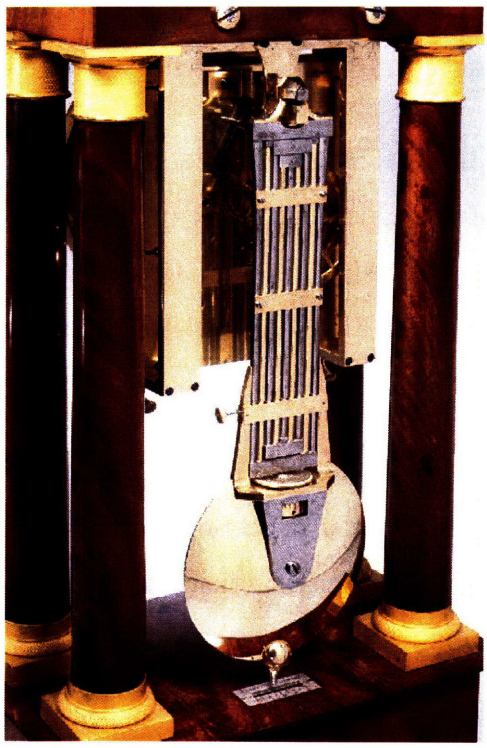

Figure 5-3: Example of a brass-steel balanced grid-iron pendulum, taken from [42]

Although the AFM head will not experience such drastic temperature changes or large lengths of scale, it is important to use a thermally stable and thermally

balanced design to achieve nanometer-scale accuracy. The AFM head will operate in an environment whose temperature is selected to be about 20°C and then controlled within ±0.01°C, over which temperature range a span of steel one inch long will expand three nanometers. Thus, any significant span of length within the metrology loop was made from Invar or Zerodur, both of which have low expansion coefficients in comparison to other common materials as seen in Table 5.2.

Material	**Expansion(parts/million)**
Aluminum	23
Stainless Steel	17.3
Titanium	11.9
Invar	1.2
Zerodur	0.1 - .01

Table 5.5: Thermal expansion rates for different materials presented in parts per million expansion per degree Celsius.

The thermal expansion budget of the AFM head made it difficult to use conventional capacitance sensors. Most commercial capacitance sensors have a cylindrical geometry to house electronics and provide a clamping surface. The cylindrical bodies of these commercial capacitance sensors are typically made out of stainless steel and have a length of at least 15 mm. Due to the thermal expansion of the adhesive used to bond the capacitance sensors, using an invar bodied capacitance sensor would create a thermal mismatch. Ultimately the product engineers at ADE technologies believed this mismatch would cause the invar bodied capacitance sensor to have less thermal stability than a conventional stainless steel sensor [4]. Earlier AFM designs based on using stainless steel capacitance sensors employed a thermally balanced design to counteract any thermal expansion. These designs were not used here due to expected inaccuracies arising from thermal gradients and nonlinear frictional effects of nanoscale movements.

The final design uses low expansion Invar or Zerodur in the entirety of the metrology loop. It is important to note that although the AFM tip is guided by steel

flexures, the thermal expansion of the steel flexures in the z direction is measured and accounted for by the capacitance gauges. This unpredictable, low frequency disturbance input is treated in the same manner as any other disturbance to the closed loop height tracking system.

5.3 Force and Metrology Loops

All methods of precision motion measurement ultimately must close a loop in order to make their measurement. A classical example of such a system is a micrometer. A micrometer pinches the object of measurement between a frame and a post actuated by a fine pitch thread thus completing a loop. The user must apply a clamping force in order to restrain the object from moving and guarantee contact during measurement. The magnitude of this force applied to the object is much greater than the force the user applies due to the amplifying nature of using a screw as a wedge. When measuring a soft material such as plastic or rubber with micrometers, the large applied force can often deform the object being measured by multiple thousandths of inches, leading to an error in measurement. This is a consequence of a coupled force loop and metrology loop, depicted in the Figure 5-5 which was augmented from [23]. To alleviate this problem, manufacturers commonly install slipping mechanisms that only allow the user to clamp with a limited amount of force. Adding this feature decouples the force and metrology loop to an approximate degree in which the applied force does not effect the accuracy of the measurement.

It is also important to conceptualize the deformation of the micrometer itself as a function of the applied force. The "C" clamp post also has a finite amount of stiffness that will deflect under load. As shown by finite element analysis, a steel micrometer of a generic shape specifically designed to have high stiffness in this degree of freedom will deflect 1 micrometer with a 10 Newton force. Furthermore, the user of the micrometer will often hold onto the "C" clamp while using the instrument, adding body heat into the steel. A 10°C change in temperature (roughly the difference between room and

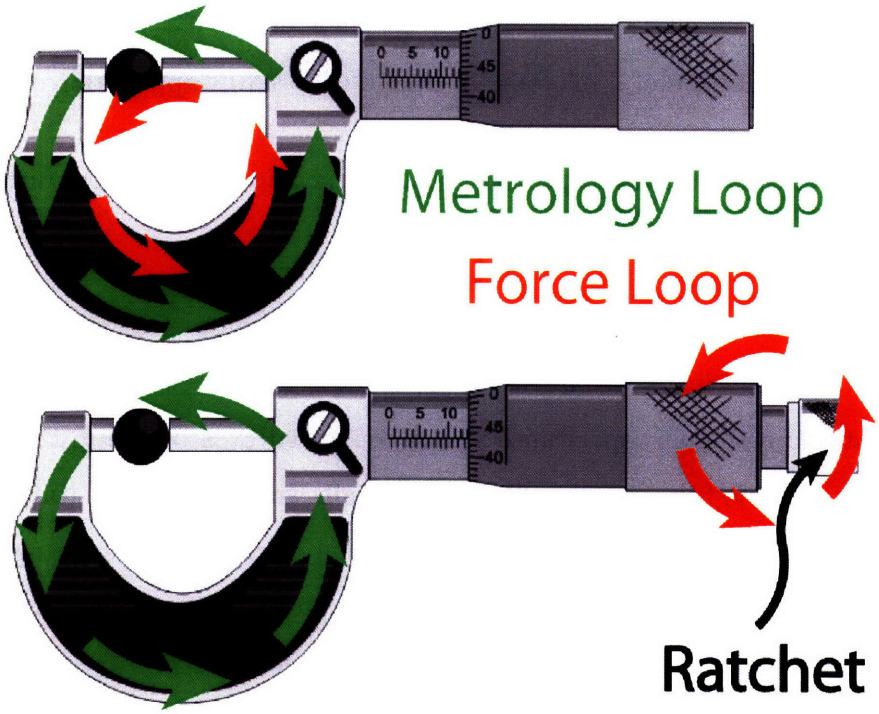

Figure 5-4: Separation of force and metrology loops in a micrometer with the advent of a ratchet mechanism, augmented from [23].

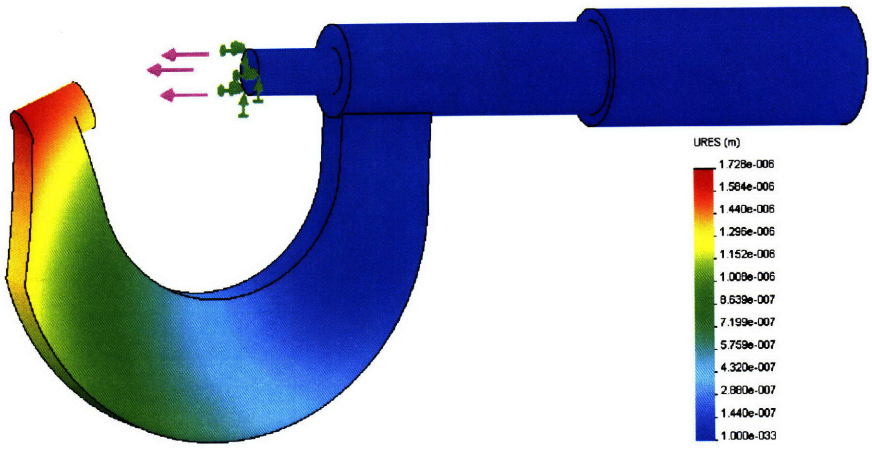

Figure 5-5: Deflection of a micrometer bridge with a 10N applied force.

body temperature) can thermally expand the post up to 5 micrometers in the direction of measurement.

The AFM head design was changed significantly after reconsidering the intersecting force and metrology loops within the design. The original design as depicted in Figure 9-4 featured a singule capacitance sensor connected by a bridge to the AFM housing. A piezoelectric tube was then fit concentrically around the capacitance sensor. The flexures preload the tube against the bridge to provide a restoring force when the piezoelectric tube contracts. In the nominal position, the guide flexure imparts a 50N force onto the piezoelectric actuator. The piezoelectric tube is capable of expanding 20μm. Given that the stiffness of the flexure is 1.0 N/μm, the preload force increases to 70 N when the piezoelectric is fully extended creating a discrepancy of 20 N. In Figure 5-7 we see through FEA that a 20 N force on the bridge would deflect it vertically by 5.8 nm. The deflection of the bridge feeds directly into the capacitance measurement and is indistinguishable from the desired measurement or the displacement of the moving mass. Although this error is repeatable and can be calibrated out of the measurement, it is better practice to design against these types of inaccuracies.

The design was altered from this point in order to seperate the force and metrology loops. The capacitance sensors were relocated onto the base of the AFM as shown in

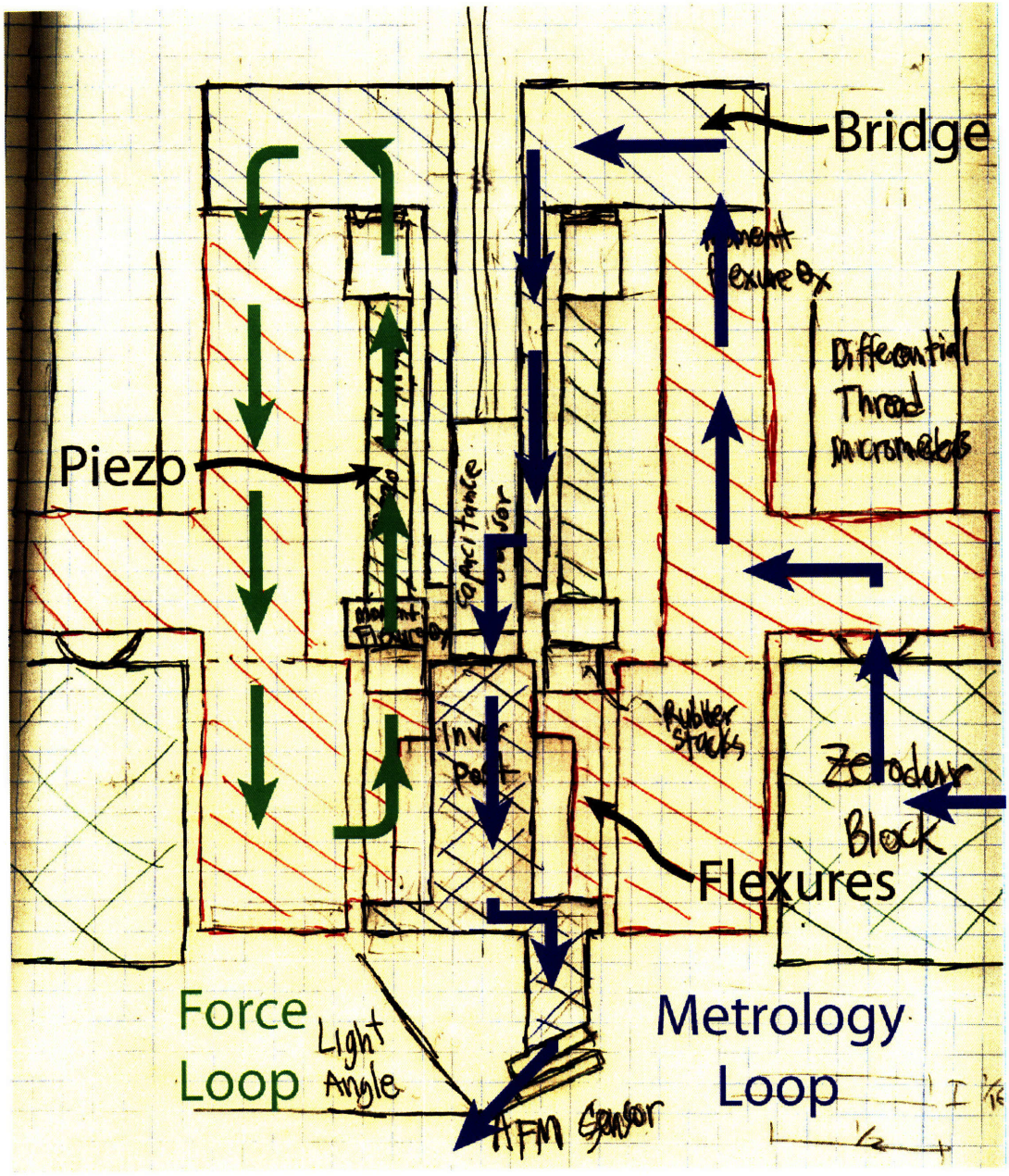

Figure 5-6: Hand-drawn sketch of the structural layout with overlayed force and metrology loops.

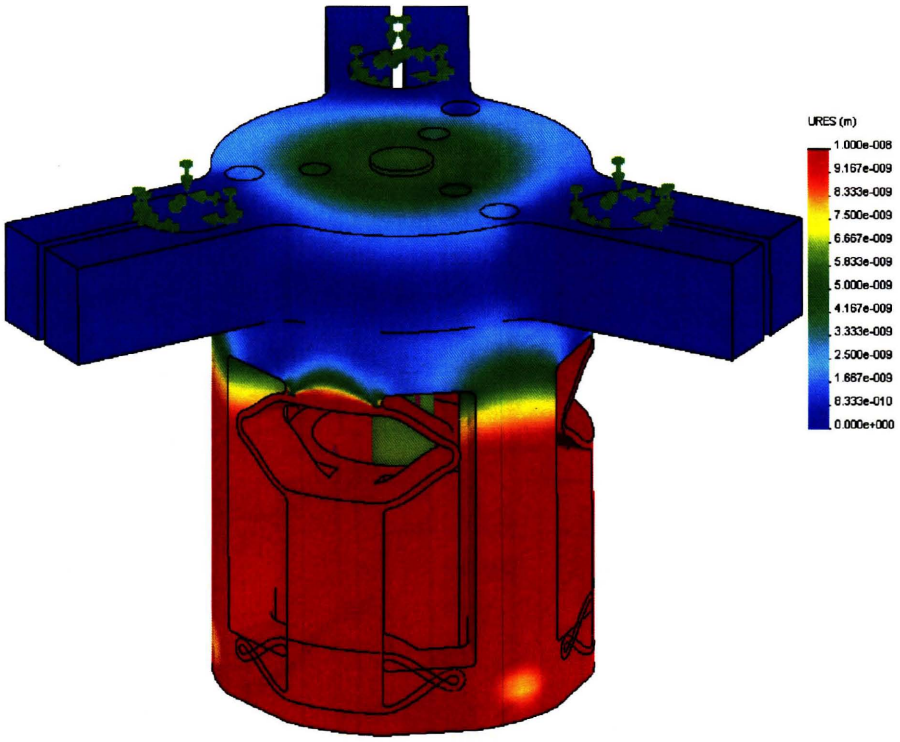

Figure 5-7: FEA image and scaling showing the deflection of the bridge caused by a 20 N preload force.

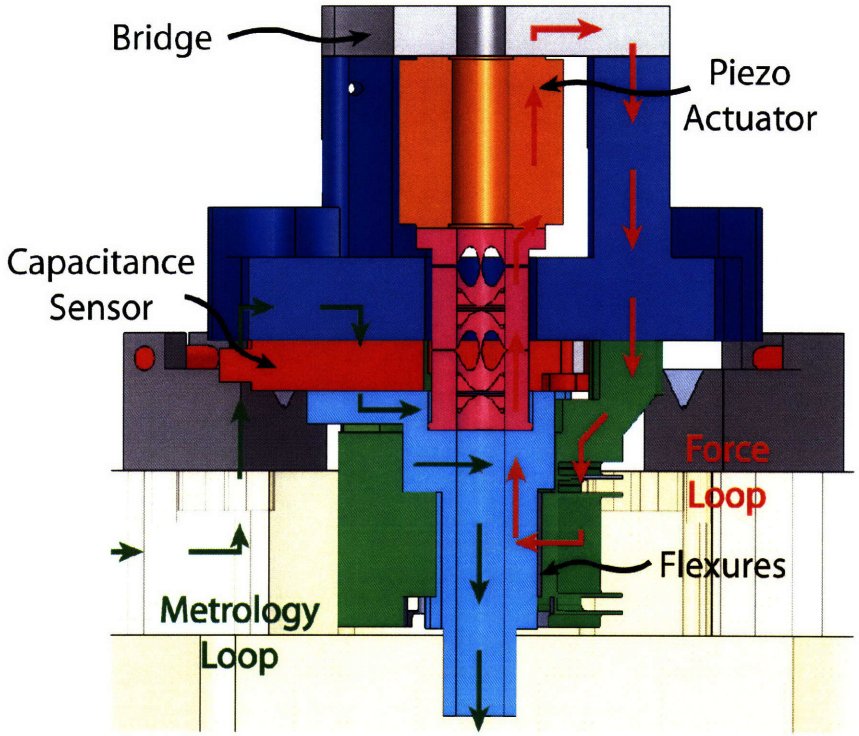

Figure 5-8: CAD model of the final assembly with overlayed force and metrology loops.

Figure 5-8. The piezoacutator still pushes on and deflects the bridge, but in doing so does not affect the measurement. This change in the design protects the measurement against repeatable error but also unpredictable transient forces such as those required to accelerate the moving mass. Although we found in our application that these types of forces created a negligible error when compared to our error budget, it is important in high accuracy applications to address the intersection of force and metrology loops.

Chapter 6

Mechanical and Electrical System Details

This chapter focuses on the mechanical and electrical details of various systems incorporated into the atomic force microscope project beginning with an overview of the current laboratory setup. We then cover the properties of the selected components and how they interface with the instrument. Lastly we look at the future interface between the SAMM stage and the atomic force microscope.

6.1 Laboratory Setup

The atomic force microscope is currently set up in the Precision Motion Control Laboratory at MIT. Although the temperature and humidity is not controlled to the degree required for nanometer level accuracy, we are able to conduct experiments to test equipment and refine the software. The current system uses a dSpace controller but will have to be switched to a National Instruments controller when the instrument is moved to UNC Charlotte. Figure 6-1 shows a picture of the laboratory setup.

As shown by the Figure 6-1, the atomic force microscope has an array of signals and wires that require proper implementation. This task is complicated by the fact that the measurement is taking place within a Helium filled chamber that is isolated from

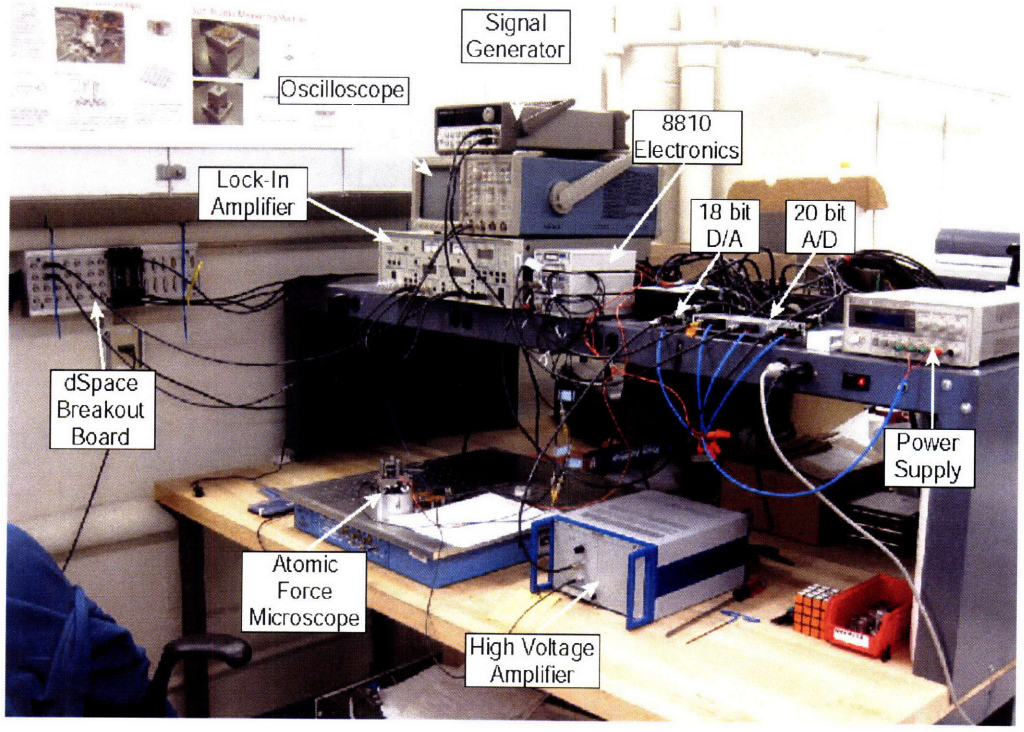

Figure 6-1: Laboratory setup of the atomic force microscope assembled in the Precision Motion Control Laboratory at MIT.

the atmospheric environment. In order to pass the signals through the chamber wall we have selected double ended floating shield BNC vacuum feedthrough connectors. A floating shield is required in our application to ensure the signal ground does not get mixed with earth ground. Vacuum grade hardware is used to ensure an air tight seal between the inside and outside of the chamber.

Passing signals through the chamber wall is but one detail of the entire electrical signal routing. The diagram presented in Figure 6-2 displays all the signals and electrical components of the atomic force microscope laid out in a block diagram format. The vertical blue wall symbolizes the interface between the chamber and the atmosphere. The dotted boxes group together bundles of vacuum feedthrough connectors. It is important to note that the 8810 capacitance sensor gauging electronics as well as the high voltage amplifier output a signal with a Lemo connector that interface with BNC connector upon feedthrough. It is imperative that the ground wire from the target be connected to the ground of the analog to digital converters and

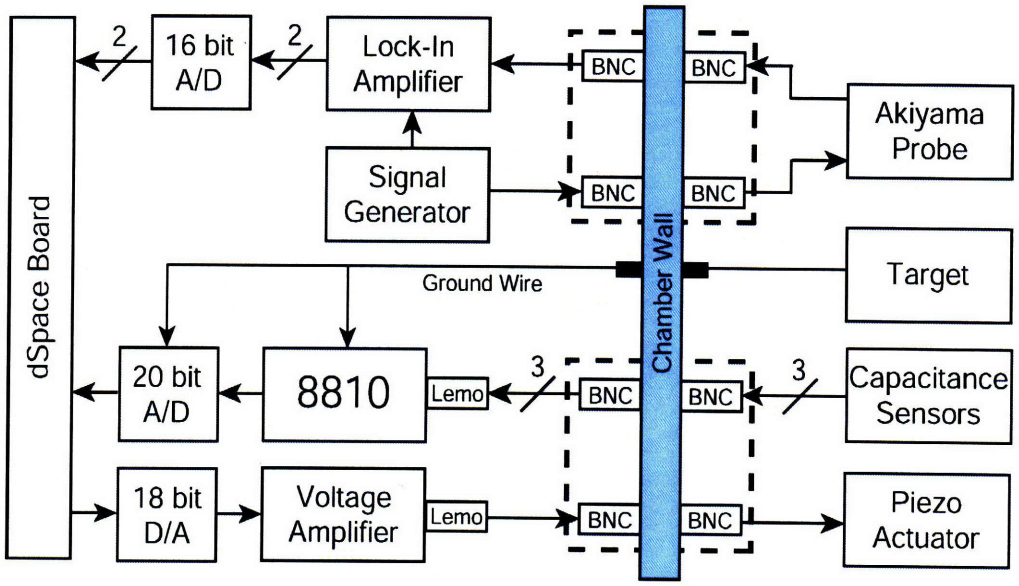

Figure 6-2: Atomic Force Microscope simplified into blocks used to model its dynamics.

the 8810 module in order to get rid of noise at 60 Hz. It is suggested to use a floating shield through the chamber wall for this ground wire although the manufacturer ADE suggests that it is not necessary. The remaining signals are all routed through coaxial cables except for the ethernet connection from the A/D and D/A electronics to the dSpace board. In this configuration there is no need for any additional wires that deliver power or ground to the components inside the chamber. The cables to power the six electronic components outside the chamber wall have been omitted from this diagram for simplicity.

6.2 Coarse Approach Screws

The atomic force microscope needed the flexibility to travel 2.5mm in height with a 1 μm positional resolution to accommodate for different sized samples. This required a second mode of guided travel beyond the piezoelectric actuator whose range is only 15 micrometers. Early designs proposed using two sets of flexures to achieve coarse and fine motion. The geometrical constraints imposed upon the AFM made it difficult to package a set of flexures capable of long range movement without straining the

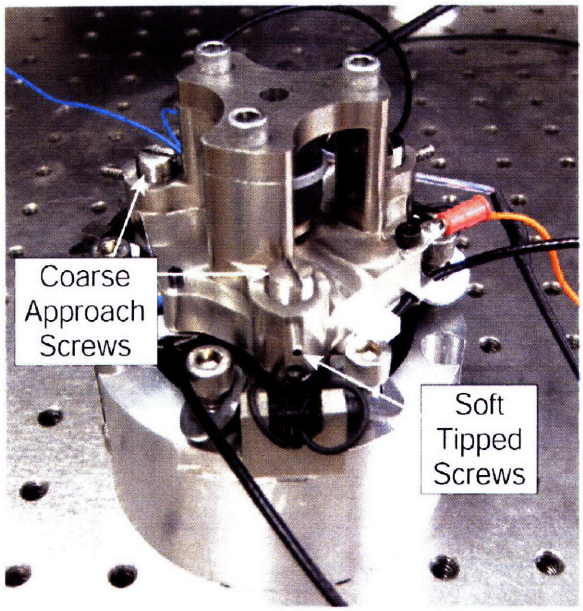

Figure 6-3: Coarse adjustment screw mechanism positioned into the kinematic mounts. The horizontal soft tipped screws lock the screw in position and provide lateral constraint.

flexural beams past their yield stress. After assessing a handful of alternatives, the design ultimately settled on using fine pitched screws to attain the desired motion.

The use of fine pitched screws made for a compact and simple way to solve the design problem. A screw provides an almost unlimited travel in the z direction. Also, the use of fine pitch allows us to achieve linear displacement with micron level resolution. The screws are threaded with 80 threads per inch which translates into 1.13 μm of linear displacement for every 1 degree the screw is turned. Any screw coarser than 80 tpi would not have met our resolution requirement. We chose the diameter to be 3/8" which coincided with the largest diameter 80 tpi tap commercially available. The tapped hole was drilled out to 9.1mm before being tapped with the 3/8" diameter 80 tpi tap. Because all three screws are equidistant from the center of the instrument, linearly displacing one screw displaces the AFM tip by one third of that distance, thereby deamplifying the coarse adjustment mechanism to 0.38 μm per degree turned per screw. This coarse adjustment screw system is pictured in Figure 6-3.

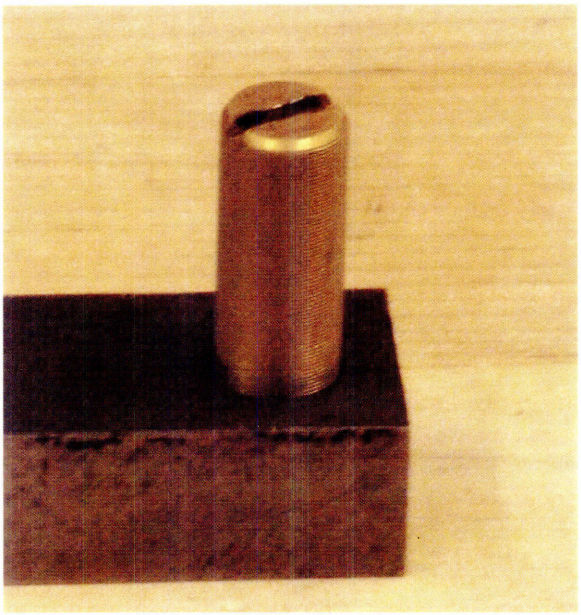

Figure 6-4: Titanium Nitride coated Invar screw screwed into a steel test fixture. The gold color is a property of the coating.

The lateral stability of the coarse adjustment mechanism became a critically important design criterion. Every screw must have a certain amount of lateral clearance in order to permit movement while allowing dimensional tolerancing between the screw and the tapped hole. Without proper constraint, this clearance can lead to lateral error motions. To mitigate the effects of this design flaw, two horizontally oriented screws are used to clamp each fine pitched screw to add lateral rigidity. Each soft-tipped screw imposes a positional constraint to the cylindrical bodied fine pitched screw thus constraining any lateral movement or axial movement once the desired height has been reached.

The base of the AFM and the coarse approach screws are both made out of Invar and remain in contact at all times. This contact between similar metals can cause a phenomenon called galling or cold welding in which the two metal bodies will chemically bond together under mild pressure in atmospheric conditions. Turning the screw breaks these microwelds and scatters bits of Invar into the joint. We first addressed this problem by applying a thin film Molybdenum Disulfide (MoS_2) onto the screws to add lubrication and form a barrier between the two components. This

Tool	Diameter	RPM	Feed
6 Flute Endmill	3/4"	407	3"/minute
4 Flute Endmill	1/2"	153	1"/minute
Drill Bit	1.75 mm	950	.0008 inches/rev
Drill Bit	2.70 mm	630	.0012 inches/rev
Drill Bit	.1957"	380	.0020 inches/rev
Drill Bit	.3598" mm	210	.0035 inches/rev

Table 6.1: Feeds and speeds used with various endmills and drills to cut Invar.

coating sheared off once the screw was screwed back into the base due to the tight tolerances on the 80 tpi pitch. One screw was then experimentally coated with a thin film of Titanium Nitride (TiN). This coating is commonly used to cover drill bits and endmills because of its estimated 24.5 GPa hardness and 3 μm thickness. We found that coating the screws with TiN successfully protected against galling and did not inhibit the screwing functionality as did the Molybdenum Disulfide. The coated screw is pictured in Figure 6-4 and engaged into a steel test piece tapped out to the 3/8" 80 tpi thread. We used the services of BryCoat, Inc. to coat the Invar screws with TiN.

We did not personally manufacture the Invar screws but did made all the other Invar pieces of the instrument such as the base, cap, and kinematic mounts in house on the light duty Bridgeport mills. Although Invar is notoriously hard to machine, we experienced minimal problems and wear by using the correct feeds and speeds based upon endmill and drill diameters. Table 6.1 lists the parameters we used to machine the Invar as dictated by Kaufman Co.

6.3 Hertzian Contact Force

We use the mechanical joint between a sphere and a flat to provide a one degree of freedom constraint. In principle the body connected to the sphere is only constrained in the direction normal to the face of the flat. To properly maintain contact through

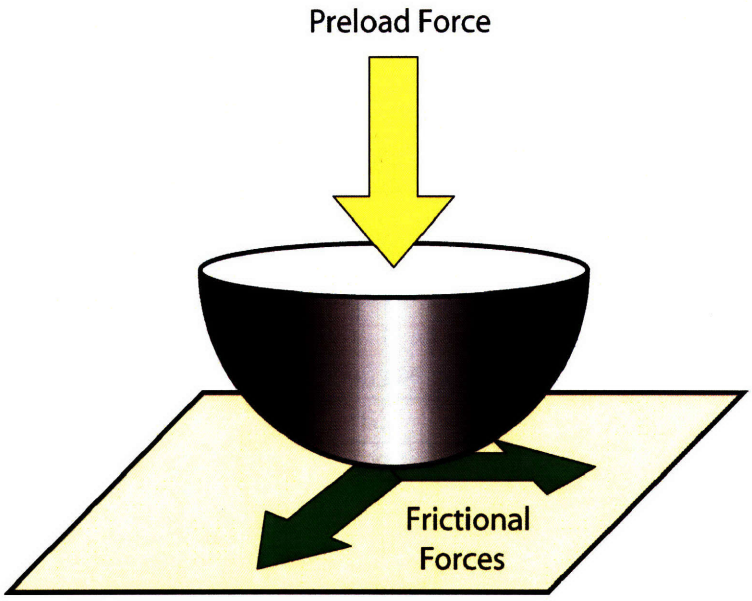

Figure 6-5: Depiction of lateral frictional forces arising from a normal preload force.

this joint, the sphere must be preloaded against the flat. This preload will give rise to frictional forces in the directions perpendicular to the preload force as depicted in Figure 6-5. Thus, in practice the sphere against flat contact is semi-constrained in the lateral direction and will resist tiny movements. These tiny movements are often the product of undesired and immeasurable changes such as temperature fluctuation that will expand and contract the bodies on the order of nanometers. This frictional effect is best alleviated by applying lubrication to the joint.

To achieve the highest stiffness, the sphere and the flat are loaded until one of the materials reaches 75% of its yield stress. The area of contact starts as a point but grows into a circle as the preload is increased. The tiny amount of area in contact limits the design to a surprisingly small amount of preload force. The radius of the circular contact patch between two spheres can be calculated through a series of equations. First we define an equivalent Young's Modulus which factors in the relative stiffness in the joint when using two dissimilar materials. The following set of equations from (6.1) through (6.4) are all taken from [25].

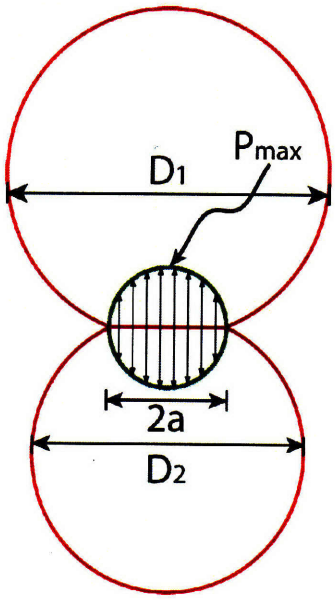

Figure 6-6: Cross-Sectional View of a Hertzian Contact Joint between two spheres.

$$E_e = \frac{1}{\frac{1-\mu_1^2}{E_1} + \frac{1-\mu_2^2}{E_2}} \tag{6.1}$$

where μ = Poisson's Ratio

and E = Young's Modulus

Similarly, we calculate an equivalent radius between the two bodies in contact. The following equation accounts for spherical, elliptical, or flat bodies. In our application where the second body was a flat, we set $R_{2major} = R_{2minor} = \infty$.

$$R_e = \frac{1}{\frac{1}{R_{1major}} + \frac{1}{R_{1minor}} + \frac{1}{R_{2major}} + \frac{1}{R_{2minor}}} \tag{6.2}$$

With these relationships defined we solve for the radius of the contact patch.

$$a = \sqrt[3]{\frac{3F}{2}\frac{E_e}{R_e}} \tag{6.3}$$

where a = Radius of Contact Patch

and F = Preload Force

The contact pressure is denoted by the vector arrows in Figure 6-6. The pressure

reaches a maximum at the center of the contact patch. To calculate the maximum contact pressure we use equation 6.4:

Material	R_{major}	R_{minor}	E	Poisson Ratio	Yield Stress
Steel	∞	∞	205 GPa	0.29	690 MPa
Invar	9.53mm	4.76mm	145 GPa	0.23	276 MPa

Table 6.2: Physical and mechanical properties of the kinematic mount joint.

Preload Force	$R_{contact}$	Max. Pressure	Deflection	Stiffness
0.21 N	22.6 μm	206 MPa	80.3nm	$4.11\frac{N}{\mu m}$

Table 6.3: Numerical results from the Hertzian Contact Force analysis.

$$q = \frac{3F}{2\pi a^2} \tag{6.4}$$

where q= Maximum Contact Pressure

F=Preload Force

and a=Radius of Contact

The joint between the sphere and the flat acts as a non-linear spring with a characteristic stiffness and displacement. We first calculate the change in displacement with equation 6.5. The following two equations are referenced from [7].

$$\delta = \frac{9F^2}{16R_eE_e} \tag{6.5}$$

Lastly, we calculate the stiffness in the joint using equation 6.6

$$k = 2 \cdot \delta^{\frac{1}{2}} \cdot R_e^{\frac{1}{2}} \cdot E_e \tag{6.6}$$

In our application we preload a concave Invar screw into a V-groove. The cross section of this type of loading can be seen in Figure 6-7. The physical and mechanical properties of this joint can be found in Table 6.2. We use these equations presented in this chapter to solve for the various quantities found in Table 6.3. We found that the Invar reached 75% yield stress with only 0.21 N of preload force resulting in a stiffness of 4.1 $\frac{N}{\mu m}$.

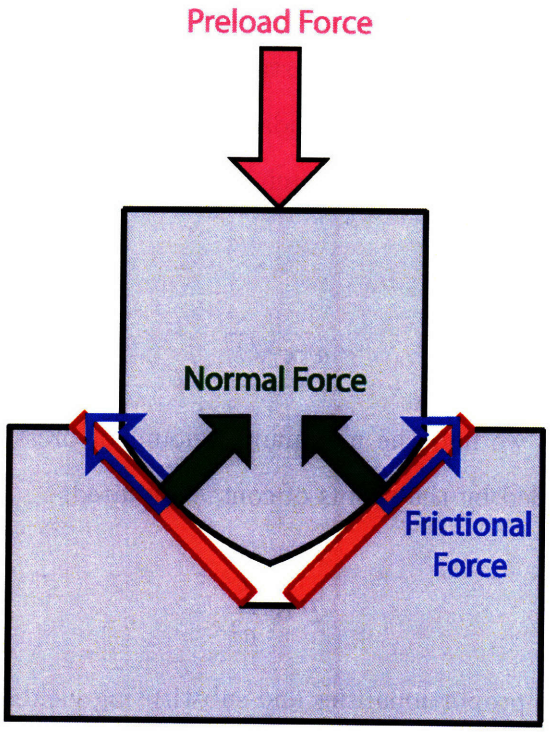

Figure 6-7: Cross-Sectional View of a Hertzian Contact Joint between the Invar screw and a V-groove. The red sections indicate the steel gauge blocks while both the screw and V-grooves are made out of Invar.

It is somewhat counterintuitive and hard to believe that a mere 0.21 N force will bring the Invar screw to yield stress. There are numerous mechanical applications such as ball bearings where small diameter steel balls are able to support a tremendous amount of weight without failing nor dissipating substantial amounts of energy. We find that this discrepancy is based upon the relatively low yield stress of Invar as compared to hardened steel. To more clearly demonstrate this point, we use the equations presented in this chapter to derive the dependence of the yield stress upon the maximum amount of preload force in a joint interfacing a sphere and a flat. In this study we disregard any numerical constants or variables such as Young's Modulus or effective radius that do not have dependance upon yield stress. From equation 6.3 we find that the area of the contact patch is proportional to the cube root of the preload force.

$$a \propto \sqrt[3]{F} \tag{6.7}$$

From equation 6.4 we find the maximum amount of pressure is proportional to the preload force divided by the radius of contact squared.

$$P \propto \frac{F}{a^2} \tag{6.8}$$

By using these two proportionalities and substituting yield stress for the pressure, we find that the maximum amount of preload force is proportional to the cube of the yield stress.

$$P = \sigma_{yield} \propto \frac{F}{a^2} \propto \frac{F}{F^{\frac{2}{3}}} = F^{\frac{1}{3}} \tag{6.9}$$

$$F_{max} \propto \sigma_{yield}^3 \tag{6.10}$$

Using this analysis, we find that a material with 10 times greater yield strength (the approximate proportion between hardened steel and Invar) can be loaded with 1000 times greater preload force without reaching plastic deformation explaining the

discrepancy between the maximum loads that can be applied to these materials.

The use of a steel gage block is a clever way to inexpensively achieve many of the physical properties that are beneficial to attain high stiffness. First, the gage blocks are precision ground leaving them with an excellent surface finish. Secondly, the gage blocks are commercially available in thin strips which allow us to use them in the metrology loop without inducing positional errors due to thermal instability. Lastly, the steel has undergone heat treatment to increase its strength. In their online catalogue [28], the manufacturer Mituyoyo claims their hardened steel gauge blocks have an 800 Vicker's Hardness which translates into an approximate 7100 MPa tensile strength. This far outperforms the 276 MPa tensile strength of Invar cited by MatWeb. Because both halves of the joint experience the same pressure, the maximum amount of preload force is limited by the weaker yield strength.

To take advantage of the gage block's physical properties, the Invar screw would have to be coated with a material with a greater yield stress than itself. The coated screw is then preloaded into a kinematic mount the cross section of which is shown in Figure 6-8. The stress felt by the coating propagates through the material in a 45 degree stress cone. The preload force felt on the Invar screw is distributed over a larger surface area and thereby decreases the stress on the Invar. We assume the stress profile to be equivalent to the profile depicted in Figure 6-6 with the maximum stress calculated with equation 6.4.

We first must evaluate the geometrical constants of the kinematic mount surface interaction before selecting a coating. As a conservative measure, we base our calculations on the assumption that the coating would have a yield stress of 690 MPa, the strength of unhardened steel. This value is almost three times the yield stress of Invar. Thus, if the load upon the Invar screw is distributed over an area three times as large as the contact patch, both the steel and Invar will reach yield stress with the same amount of preload force. The radius of the contact patch with a 0.22 N preload force was calculated to be 22.6 μm. Assuming a 45 degree stress cone, we calculate

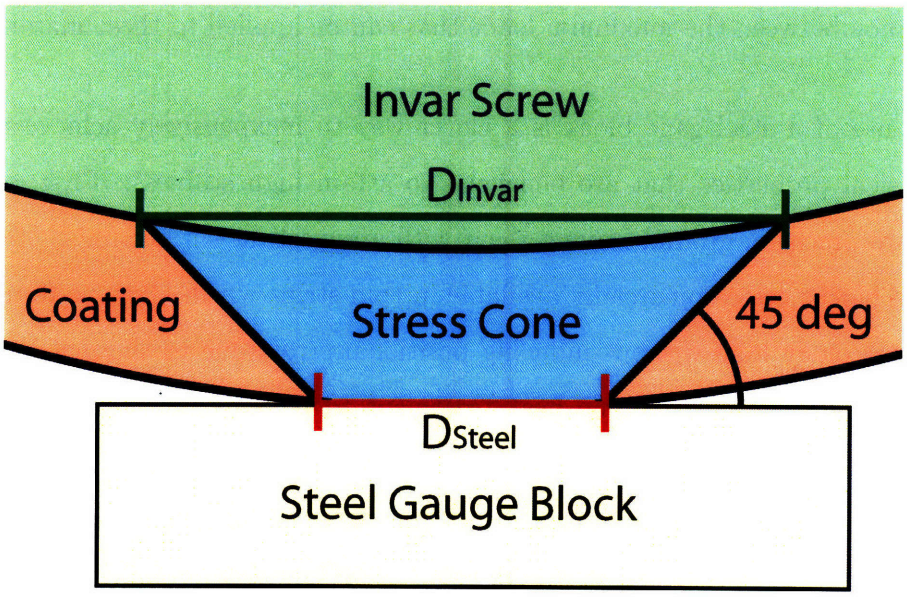

Figure 6-8: Cross-Sectional View of a coated screw interfacing with the steel gauge block and the resultant stress cone.

that the coating must be 16.4 μm thick in order to increase the surface area upon the Invar screw by three fold. With this coating, the maximum preload force increases to 3.5 N resulting in a stiffness of 10.3 $\frac{N}{\mu m}$. The coating must have a yield stress equal to or greater than 690 MPa and must be tens of microns thick. Under these criterion, we suggest using hard chrome plating at the tip of the screw.

Lastly, it is important to recognize an easy error to make while calculating the stiffness in a Hertzian contact joint. Designers may be tempted to solve of the stiffness by simply dividing the force applied by the deflection of the joint as is done in linear spring systems. This leads to calculating a stiffness value that is substantially lower than the actual stiffness. A more accurate calculation uses the localized slope at the specific point upon the force vs. displacement curve. This concept is illustrated in Figure 6-9 which shows the force versus displacement curve for this particular application. Numerically, the localized slope k_2 is about 50% greater than k_1.

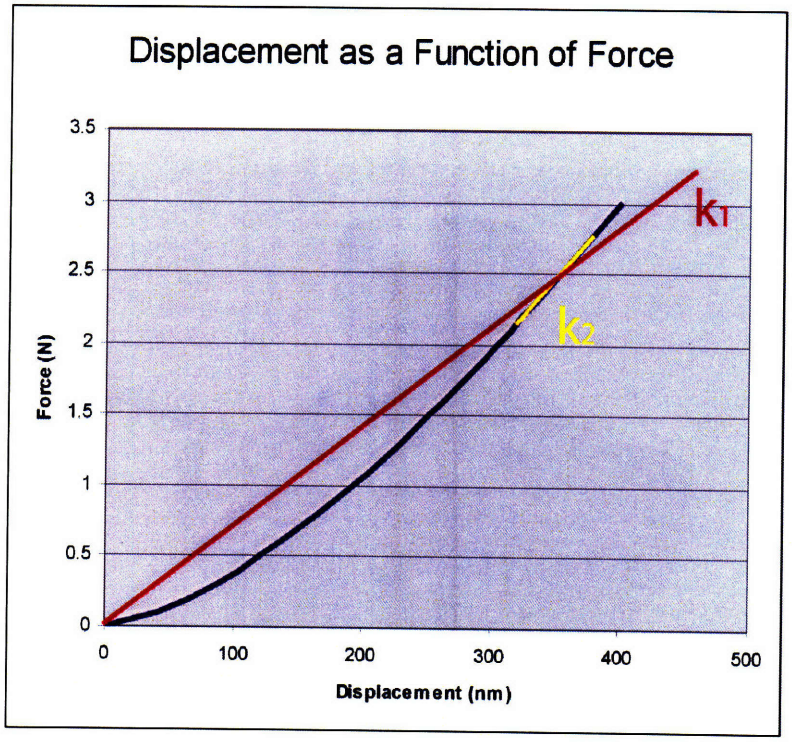

Figure 6-9: The blue line on this chart shows the amount in which a ball on a flat is compressed as a function of the preload force. We see that the localized slope is fifty percent greater than the estimate for the spring constant calculated simply by dividing the force by the displacement at any point.

6.4 Piezoelectric Actuator

This section gives a overview of the properties and criterion that drove the design towards the selected piezoelectric actuator and voltage amplifier. The most critical constraint required that the actuator have a tubular geometry which limited us to a handful of commercially available actuators. We selected Physik Instrumente's P-016 series actuator because of its high load capability and build quality. A picture of the actuator is supplied in Figure 6-10. The piezoelectric actuator was glued to the Invar cap an steel decoupling flexure using a 730 2-part epoxy purchased from Epoxy Technologies.

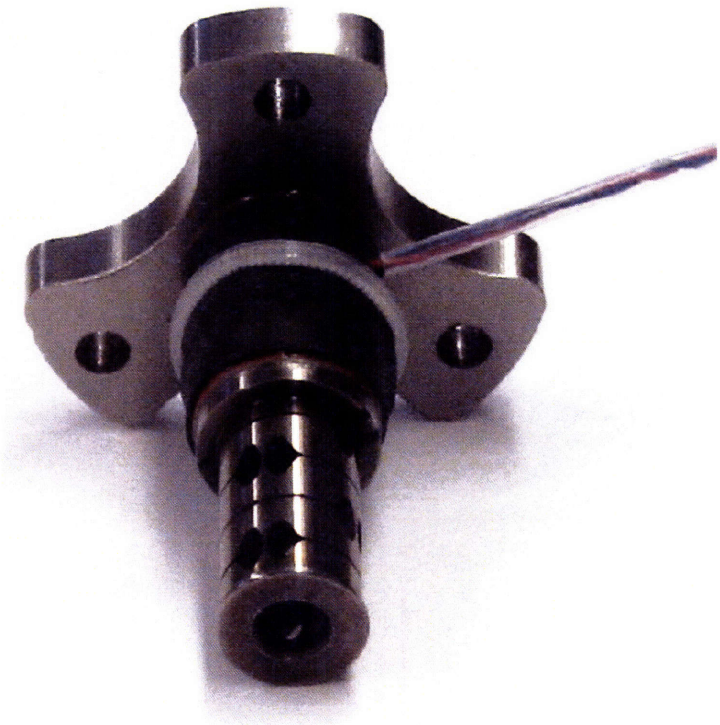

Figure 6-10: Photograph of the piezoelectric actuator sandwiched between the decoupling flexure and the three legged cap.

The selected piezoactuator has the following specifications:

Length: 21mm

Inner Diameter: 8mm

Outer Diameter: 16mm

Displacement: 20 μm

Stiffness: 190 $\frac{N}{\mu m}$

Capacitance: 170 nF

Model Number: P-016-15H

Manufacturer: Physik Instrumente

The inner diameter was required to be at least 7mm to give adequate clearance to the 4.2mm diameter borescope. A length of 20mm was chosen as a result of the 0.1% strain limit of a piezoelectric material and a desired 20 μm displacement. An outer diameter of 16mm yields a 4mm radial shelf in which to interface and glue to other mechanical components.

The voltage amplifier was chosen specifically to meet our 100 Hz bandwidth requirement. The piezoelectric actuator can be modeled electrically as a capacitor given that it will exhibit a certain amount of capacitance based on its geometrical dimensions. In order to change the voltage across the actuator the amplifier charges and discharges this equivalent capacitor by delivering current. The current is also based upon the magnitude of the voltage change. The actuator is capable of expanding 20 μm over a change of 1000 Volts. The largest step change we intend to measure within the breadth of our samples would be 5 μm, corresponding to a change of 250 Volts. Thus the attainable bandwidth of the actuator is based upon the capacitance of the actuator, the change in voltage, and the amount of current that the amplifier can deliver. These three variables are related in Figure 6-11 which is supplied by the manufacturer of the voltage amplifier Physik Instrumente [8]. From this figure we find the maximum deliverable large signal bandwidth from a 50mA amplifier for a 250 Volt change in voltage across a 170 nF piezoelectric actuator is approximately 200 Hz which fulfills our bandwidth requirement.

Based on this graph, we chose a 50mA voltage amplifier supplied by Physik Instrumente with the following characteristics:

Peak Current: 50mA

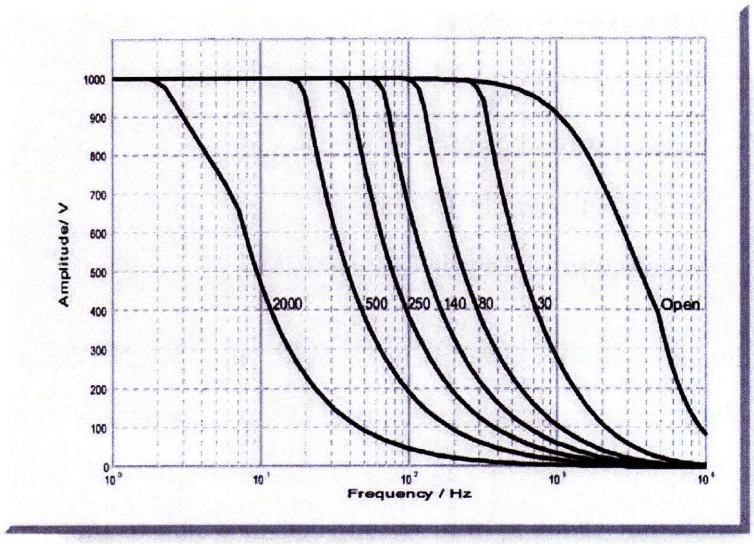

Figure 6-11: This graph shows the current limited bandwidth for a 50mA amplifier based on the capacitance of the actuator and the change in voltage taken from the Physik Instrumente website [8].

Average Current: 13mA

Peak Power: 400W

Voltage Range: -3 to -1100 Volts

Model Number: E-507

Manufacturer: Physik Instrumente

6.5 Capacitance Sensors

The capacitance sensors used in the atomic force microscope project were selected on the basis of performance, geometry, and thermal stability. We moved away from conventional cylindrical capacitance sensors after reevaluating the thermal stability of the microscope. This selected model is built out of a ceramic substrate with a glass ceramic sensor that has experimentally shown a thermal coefficient of expansion of 2.3×10^{-6} parts per million. Over the probe's 6mm tall body it will expand 0.13 nanometers with a 0.01 degree change in temperature. We must pay particular attention to this thermal expansion for it is within our metrology loop.

We selected the capacitance sensors to have subnanometer resolution to achieve our targeted nanometer positional accuracy. The capacitance sensors have a range of $\pm 25\mu$m, the narrowest possible range in which all three capacitance sensors could be positioned to overlap the piezoelectric actuator's 20μm of displacement. The bandwidth of the capacitance sensors was selected to be 1000 Hz, more than three times higher than the 300 Hz target closed loop bandwidth of the system. We have characterized the filters associated with the capacitance sensors as two poles at 700 Hz with the following transfer function shown in equation (6.11). We attained this specification by fitting models to the measured Bode plot. The Bode plot of this transfer function is shown in Figure 6-12. We see from the Bode plot that the capacitance sensors subtract 32.1 degrees of phase at our targeted 200 Hz crossover frequency of the position control loop.

$$H(s) = \frac{1}{5.17 \times 10^{-8} s^2 + 4.55 \times 10^{-4} s + 1} \tag{6.11}$$

The important values and properties of the capacitance sensor are listed below.

Resolution: 0.120 nm

Range: $\pm 25\mu$m

Bandwidth: 1000 Hz

Thermal Expansion: 2.3 $\times 10^{-6}$ / (deg C) / (meters)

Model Number: 2820-V

Manufacturer: ADE Technologies

The following section uses the data presented in graphs and tables characterize the electrical noise performance of the system. There are two electrical noise floors in the system based on the limitations of the of the capacitance sensors and the analog to digital converters. The capacitance sensors are specified to have 0.12nm RMS noise at 1000 Hz bandwidth. The second limit of noise is derived from the analog to digital converters. We employed higher resolution converters than the 16 bit converters that come standard with dSpace software. Through experimental

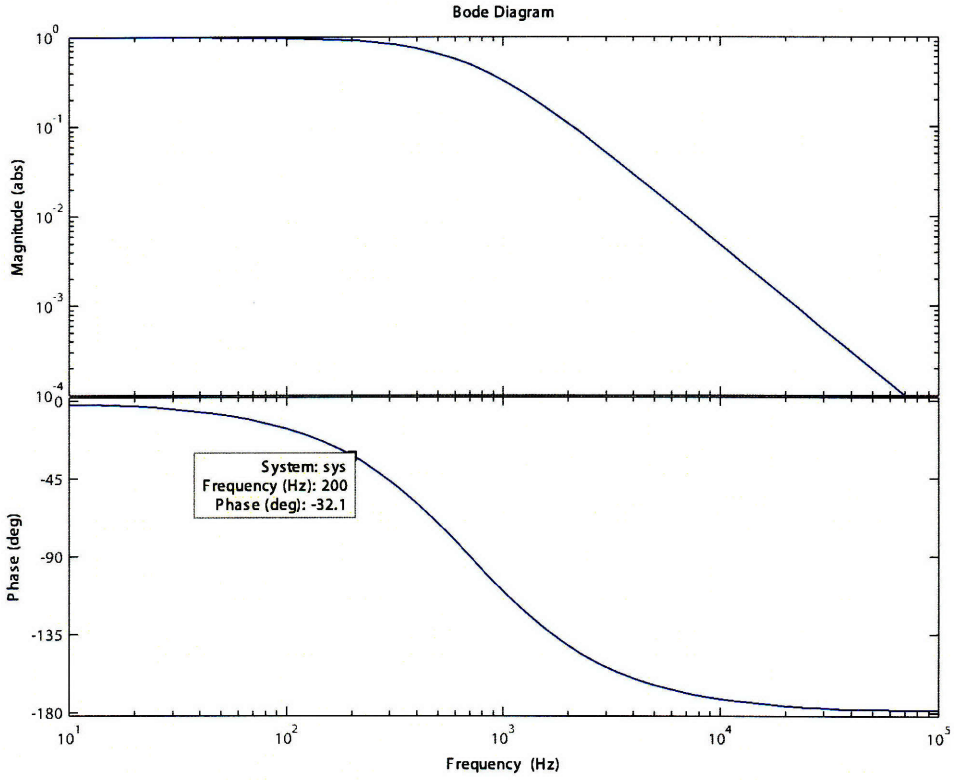

Figure 6-12: This Bode plot of the capacitance sensors shows the phase loss to the system due to the capacitance sensor filters.

testing we found that each board outputs 0.045 nm RMS noise with a complete range of 50 microns amounting to about 20 effective bits. This performance was superior than the capacitance sensor channels which on average output 0.237 nm RMS noise at 1000 Hz bandwidth. Thus, the analog to digital conversion does not impede the resolution of the capacitance sensors. We further reduce the noise of the position measurement by taking the average of the three capacitance sensor readings. This increases the number of samples per second by threefold and thereby decreases the noise by a factor of the square root of three to 0.170nm RMS at 1000 Hz bandwidth. Table 6.4 gives the noise values for the open channels and the capacitance sensor measurements as well as the averaged sums. Figure 6-13 shows a 250 continuous measurements measured by the three capacitance sensors.

Sensor	Noise (nm)	Open Channel	Noise (nm)
1	0.239	1	0.047
2	0.214	2	0.053
3	0.260	3	0.049
Sum	0.170	Sum	0.029

Table 6.4: Root mean square noise values for the capacitance sensor readings and open dSpace channels.

The timing of the capacitance sensors were phase locked against each other to avoid measurement interference. To do so, the three sensors were drive synchronized to set an appropriate phase angle with respect to the master probe. These parameters were set electronically by setting the appropriate jumper configurations. Table 6.5 shows the selected phase lock parameters for each gauging module.

Probe SN	Configuration	Phase
11378	Master	0
11379	Slave	120
11380	Slave	240

Table 6.5: This table displays the drive synchronization parameters of each probe identified by their serial number.

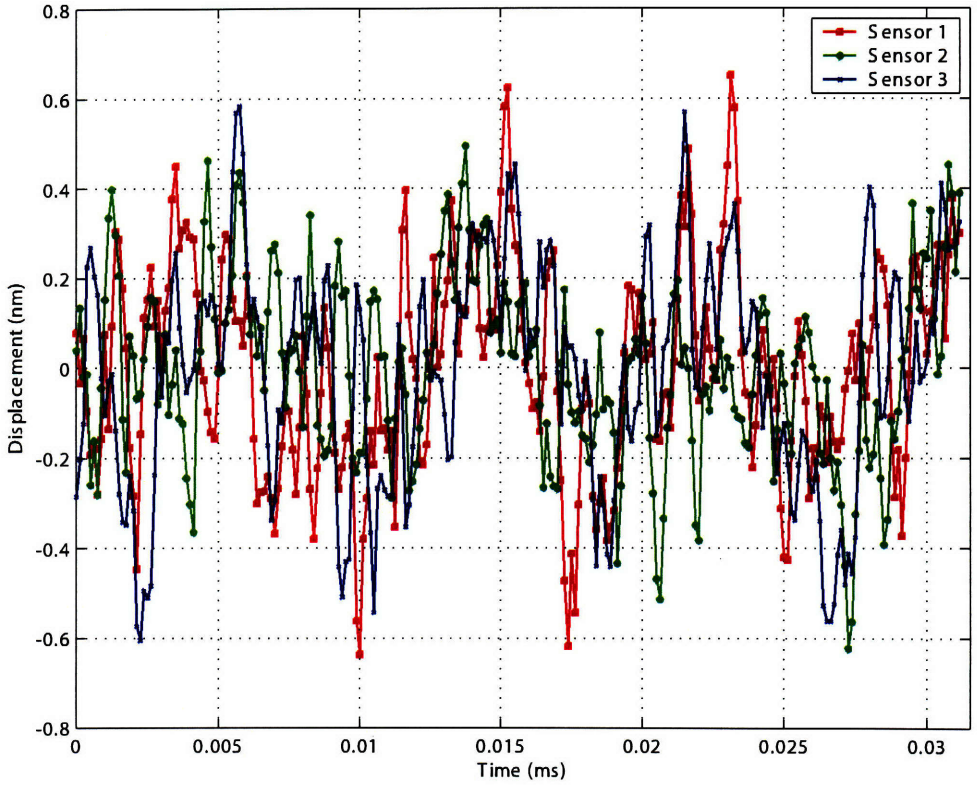

Figure 6-13: Noise data taken simultaneously from all three capacitance sensors.

6.6 Borescope

The borescope is an integral part of the atomic force microscope although it plays no direct role for the sub-atomic metrology. The function of the borescope is to provide a coarse view of the sample in order to locate micron-sized features. Without the borescope it would only be practical to measure uniform samples such as a square wave grating that are composed of one repeated pattern. The borescope slips concentrically though the entire length of the atomic force microscope while achieving mechanical, electrical, and thermal isolation.

The borescope is nested at the center of the instrument making its geometry an integral factor for the design of the AFM. We selected a borescope with a diameter of 4.2mm. A smaller diameter borescope could have been used to provide more space, but the quality of the instrument based upon its robustness and image resolution became compromised with any further reduction in size. The close proximity and potential conductivity of the borescope to the 1000 Volt piezoelectric actuator made it a safety concern. We used the mechanical separation of the atomic force microscope to form an adequate gap distance between the two components to prevent a discharge of current into the borescope. Under atmospheric conditions, the following equation [32] relates the amount of electrical insulation provided by air as a function of the gap size.

$$V_{max} = 2.44d + 2.13\sqrt{d} \tag{6.12}$$

where V_{max}=Maximum Insulated Voltage in kV

d = thickness of air gap in mm

Solving this equation for 1 kV of insulation, we find that the air gap between the piezoelectric and the borescope must be at least 0.1 mm. The piezoelectric actuator has an inner diameter of 7.8mm. The borescope must slide through a 6mm hole thus mandating at least 0.9mm of clearance between the borescope and the piezoelectric actuator. These clearances among other features are pictured in Figure 6-14. Due to

time constraints, this portion of the project has not yet been completely fabricated or tested.

The borescope must be mechanically decoupled from the atomic force microscope since its large mass and long reach make it a potential conductor of mechanical noise. We intend to use a mounting device bolted to the SAMM stage chamber wall to position and hold the borescope in place. Two o-rings are employed to constrain the position of the borescope while providing an air tight seal between the chamber and the atmosphere. The mounting device allows us to adjust the lateral position of the borescope to center it concentrically with the decoupling flexure and Invar target. The instrument as a nominal 0.9mm clearance between its 4.2mm outer diameter and 6.0mm inner diameter of the atomic force microscope. Figure 6-15 shows a picture of the borescope holder machined for this purpose.

6.7 Dimensional Positioning of the AFM Head

The atomic force microscope built in this thesis was specifically tailored to interface with UNC Charlotte's Sub-Atomic Measuring Machine (SAMM). The SAMM stage moves and measures the sample laterally while the atomic force microscope senses and measures the vertical terrain. For interfacing these two instruments, there were two components of the SAMM stage that were of particular importance: the metrology head and the sample stage. The atomic force microscope is designed to sit upon the metrology head while measuring a sample situated on the sample stage. The metrology head remains stationary while the sample stage is capable of moving $\pm$ 12.7mm in both x and y directions as well as 100 μm in the z direction. The metrology head has an elliptically shaped hole in its center that allows access to the sample stage. The face of the measured sample lies on the same plane as the laser interferometers which measure the position of the sample stage. This feature of the SAMM stage is designed to minimize Abbe error in the laser axis. Thus, the atomic force microscope must reach through the elliptical hole in the metrology head down to the Abbe plane

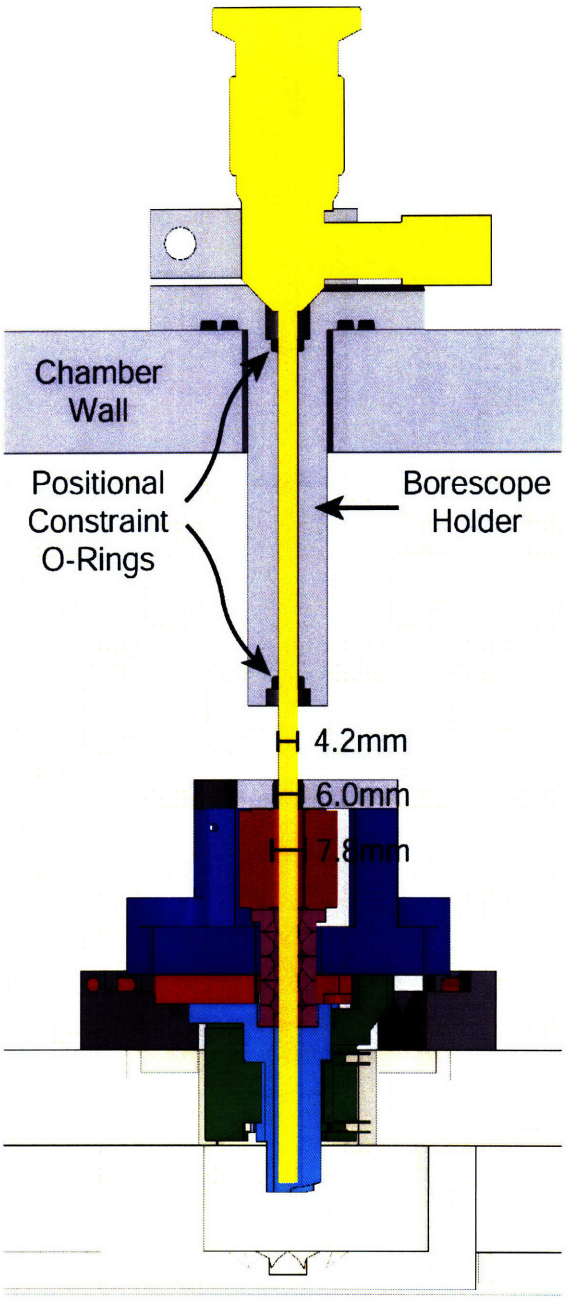

Figure 6-14: This cross section of the assembly solid model shows the clearance dimensions between the borescope and other mechanical features as well as the constraint of the instrument by two O-rings.

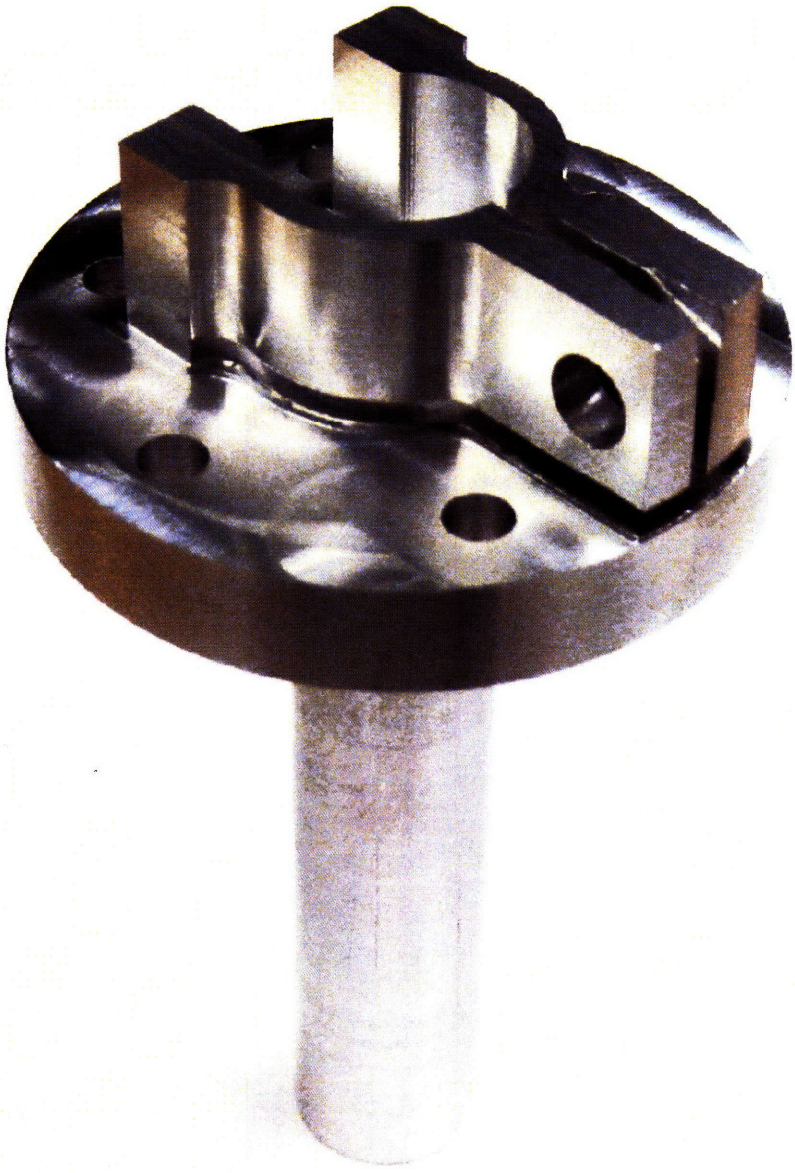

Figure 6-15: Picture of the holder designed to affix the borescope to the chamber wall. The two cantilevered beams are bolted together to squeeze and hold the borescope.

of the sample stage.

As the project unfolded, we discovered some peculiarities in the geometry of the elliptically shaped hole. The fat end of the hole does not align with the center of the sample but instead is offset by 7.7mm. This relationship between these two parts is best illustrated in Figure 6-16. This hole geometry was designed by Holmes to accommodate an STM measurement head. The cylindrical body of the microscope was centered about the 7.7mm offset point and given 1mm of clearance from sides of the hole thereby limiting the radius of the flexures to 17.6mm. The skinny end of the hole originally designed by Holmes' work [13] to allow access for a instrument such as a borescope to obtain coarse view target visibility from the side. We did not use the skinny end of the elliptical hole because our microscope takes both fine and coarse view images from the top.

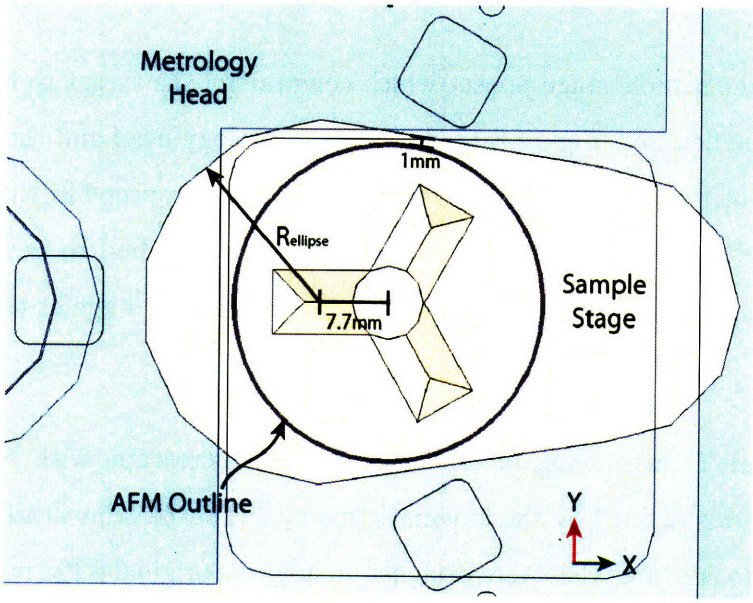

Figure 6-16: Top down view of the metrology head and sample stage assembly with overlayed geometric constraints.

While designing the interface we had to ensure that the components of the AFM would not crash into the sample stage at any point in the sample stage's range of motion. The steel flexures did not protrude past the metrology head and therefore did not pose a geometrical conflict. In order to reach the sample, the Invar target

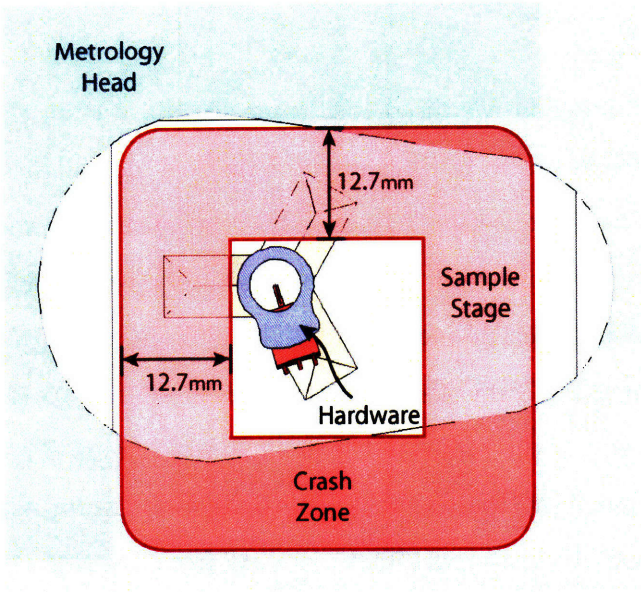

Figure 6-17: Top down view of the metrology head and sample stage assembly with overlayed geometric constraints.

reached into the sample stage pocket which constrained the target to have a smaller radius than the flexures. Figure 6-17 shows the metrology head and the sample stage in the center of its travel. Figure 6-18 shows the same concept in a 3 dimensional view. The red areas indicate the geometrical space which had to remain empty of any AFM components in order to avoid crashing the sample stage at the limits of its travel.

The X and Y positioning of the atomic force microscope with respect to the metrology head is defined by the kinematic mounts. The Zerodur head has three pin joints built into its frame that were designed to hold the original STM microscope that are was not centered concentrically about the kinematic mount for the sample. We chose to implement our own kinematic mounts to customize them to our application, implement a better v-groove geometry, and to correctly center the device. In order to accurately glue the new kinematic mounts to the metrology head, we built an interfacing module that locates itself with respect to the elliptical hole to obtain X and Y registration. The module has three bays that hold each kinematic mount in the X, Y, and θ_Z directions while the plane to plane contact with the metrology head

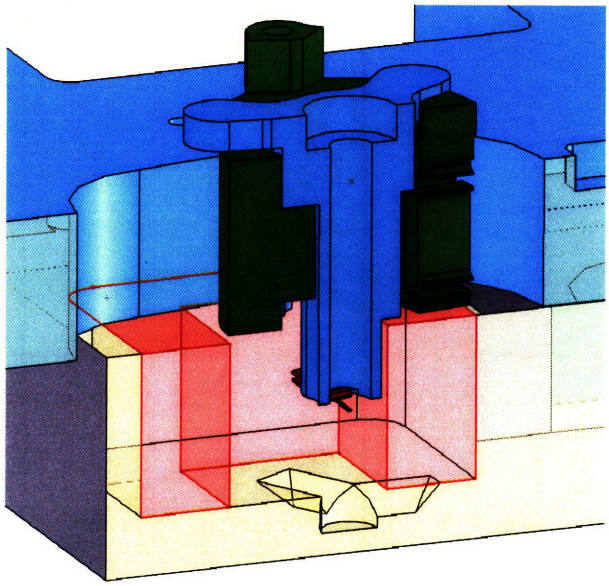

Figure 6-18: Three dimensional view of the crash zone depicting the tighter dimensional constraints on the Invar target as compared to the steel flexures.

constrain Z, θ_X, and θ_Y. Figure 6-19 shows a picture of the module with one kinematic mount inserted into a bay. The module itself is turned upside down with respect to its intended orientation in order to more easily display its mechanical features and functionality.

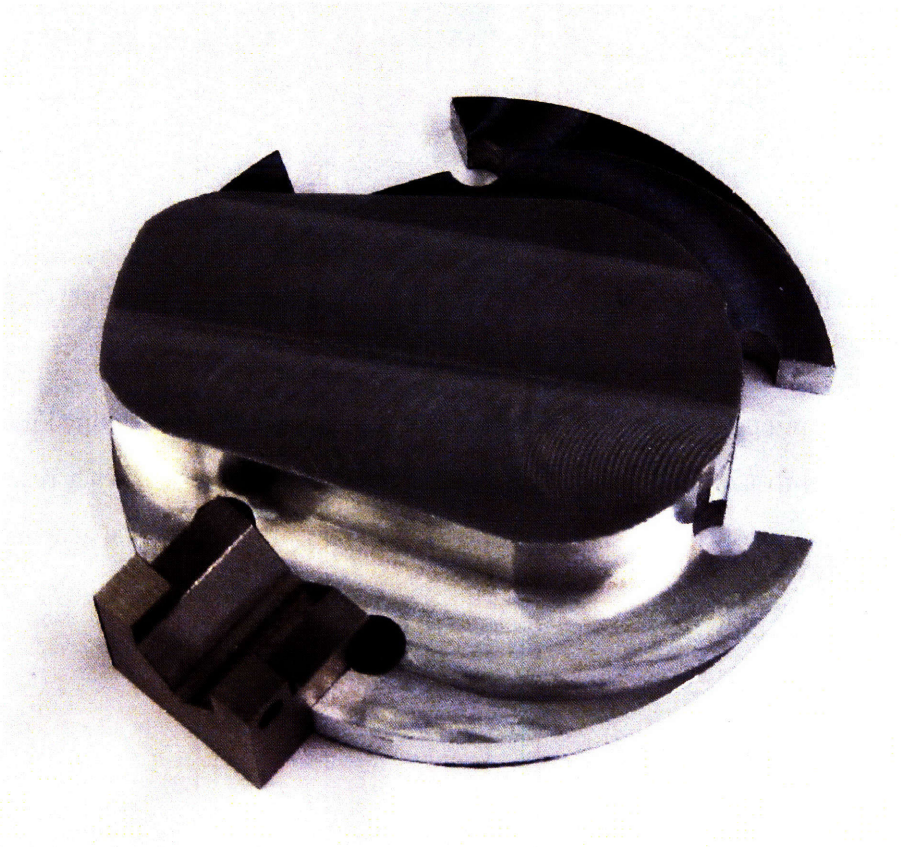

Figure 6-19: Aluminum rigging fixture made to hold the three kinematic mounts laterally with respect to the metrology head while they are being glued.

Chapter 7

Positional Dynamics and Control

This chapter covers the dynamics and controls associated with the position control system. It begins by theoretically deriving the dynamics of the atomic force microscope and then compares them to the results of the experimentally measured Bode plots. A controller is implemented though dSpace software and the performance of the system measured by noise and step response is examined.

7.1 Theoretical Analysis

It is important to create and analyze a dynamic state space model of the atomic force microscope to properly design the hardware. The model contains three primary masses as depicted in Figure 7-1. Mass 3 represents the moving body which holds the Akiymama probe whose position is measured by the capacitance sensors. The Invar base which holds the capacitance sensors and the steel flexures that guide the moving stage is modeled as mass 2. Mass 3 is driven relative to mass 2 by the piezoelectric actuator. Lastly, a large block of Zerodur that mounts onto mechanical ground but also includes various electronics, lasers, and mirrors comprises mass 1. This block is referred to as the SAMM metrology frame. Both the Zerodur block and the Invar base use three micrometers mounted in V-Grooves to kinematically define their positions. The stiffnesses of these joints, k_1 and k_2, are calculated by using the Hertzian contact stress calculations. The calculation of k_1 was a rough estimate

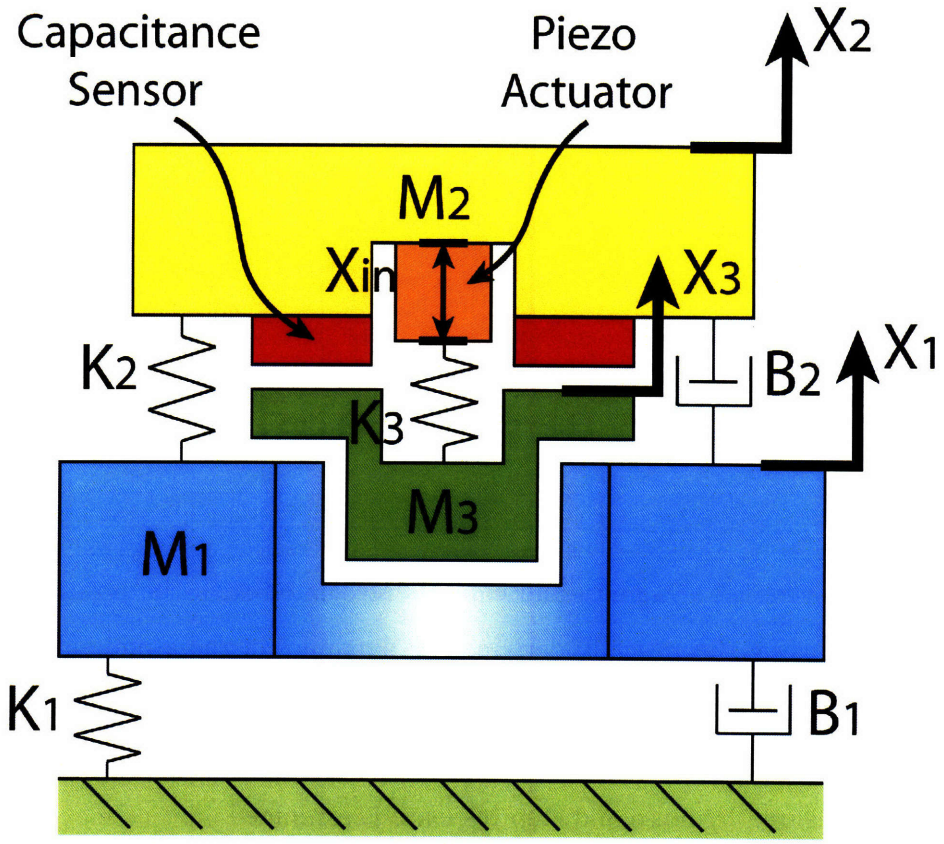

Figure 7-1: Atomic Force Microscope simplified into spring/mass lumped elements used to model its dynamics.

because the physical properties such as preload force and ball diameter were only available to a first order approximation. We calculated the stiffness of the decoupling flexure k_3 in a previous chapter. The weight of each mass and stiffness of each joint is complied in the Table 7.1.

We modeled the piezoelectric as a displacement source because its stiffness, a specified 190 N/m, was an order of magnitude greater than the stiffness of the in-

Component	Mass (kg)	Stiffness $\frac{N}{\mu m}$
Metrology Head	6.0	73
Invar Base	0.5	36
Moving Mass	0.11	18

Table 7.1: Stiffness and Mass values for Components in the Atomic Force Microscope.

series moment flexure. We derived the following dynamic equations by applying simple force balances to each mass:

$$m_1\ddot{X}_1 = -k_1X_1 + k_2\left(X_2 - X_1\right) - b_1\dot{X}_1 + b_2\left(\dot{X}_2 - \dot{X}_1\right) \tag{7.1}$$

$$m_2\ddot{X}_2 = k_2\left(X_1 - X_2\right) + k_3\left(X_3 - X_2\right) + b_2\left(\dot{X}_1 - \dot{X}_2\right) + b_3\left(\dot{X}_3 - \dot{X}_2\right) - k_3X_{in} \tag{7.2}$$

$$m_3\ddot{X}_3 = k_3\left(X_2 - X_3\right) + b_3\left(\dot{X}_2 - \dot{X}_3\right) + k_3X_{in} \tag{7.3}$$

We can rearrange the equations to form the state space matrix found in Figure 7-2. This model takes into account the dynamics of the AFM head and the SAMM stage. The dynamics of the SAMM stage were not present in preliminary testing of the AFM head presented in this thesis. This effectively removes mass and spring 1, simplifying our system to a four by four state space matrix seen in Figure 7-3.

$$\begin{bmatrix} \dot{x}_1 \\ \ddot{x}_1 \\ \dot{x}_2 \\ \ddot{x}_2 \\ \dot{x}_3 \\ \ddot{x}_3 \end{bmatrix} = \begin{bmatrix} 0 & 1 & 0 & 0 & 0 & 0 \\ \frac{-k_1-k_2}{m_1} & \frac{-b_1-b_2}{m_1} & \frac{k_2}{m_1} & \frac{b_2}{m_1} & 0 & 0 \\ 0 & 0 & 0 & 1 & 0 & 0 \\ \frac{k_2}{m_2} & \frac{b_2}{m_2} & \frac{-k_2-k_3}{m_2} & \frac{-b_2-b_3}{m_2} & \frac{k_3}{m_2} & \frac{b_3}{m_2} \\ 0 & 0 & 0 & 0 & 0 & 1 \\ 0 & 0 & \frac{k_3}{m_3} & \frac{b_3}{m_3} & \frac{-k_3}{m_3} & \frac{-b_3}{m_3} \end{bmatrix} \begin{bmatrix} x_1 \\ \dot{x}_1 \\ x_2 \\ \dot{x}_2 \\ x_3 \\ \dot{x}_3 \end{bmatrix} + \begin{bmatrix} 0 \\ 0 \\ 0 \\ \frac{-k_3}{m_2} \\ 0 \\ \frac{k_3}{m_3} \end{bmatrix} X_{in}$$

Figure 7-2: The dynamic equations derived by taking a force balance on each mass are rearranged to fit into this six by six state space matrix.

It is important to correctly define the output of our system. As depicted in Figure 7-1, the capacitance sensors are mounted to the bottom of mass 2 and face

$$\begin{bmatrix} \dot{x}_2 \\ \ddot{x}_2 \\ \dot{x}_3 \\ \ddot{x}_3 \end{bmatrix} = \begin{bmatrix} 0 & 1 & 0 & 0 \\ \frac{-k_2-k_3}{m_2} & \frac{-b_2-b_3}{m_2} & \frac{k_3}{m_2} & \frac{b_3}{m_2} \\ 0 & 0 & 0 & 1 \\ \frac{k_2}{m_3} & \frac{b_3}{m_3} & \frac{-k_3}{m_3} & \frac{-b_3}{m_3} \end{bmatrix} \begin{bmatrix} x_1 \\ \dot{x}_1 \\ x_2 \\ \dot{x}_2 \end{bmatrix} + \begin{bmatrix} 0 \\ \frac{-k_3}{m_2} \\ 0 \\ \frac{-k_3}{m_3} \end{bmatrix} X_{in}$$

Figure 7-3: The modeled system was simplified to exclude the dynamics of the SAMM stage by setting $x_1 = \dot{x_1} = \ddot{x_1} = 0$. This four by four state space matrix holds the dynamic equations that describe the tested hardware.

the top surface of mass 3. Thus, the capacitance sensors measure X_2 - X_3, not the absolute movement of X_3. The Bode plot of these two outputs with respect to X_{in} can be seen in Figure 7-4. From this plot we see that the differential measurement shows better performance with a reduction in phase loss around 1 kHz.

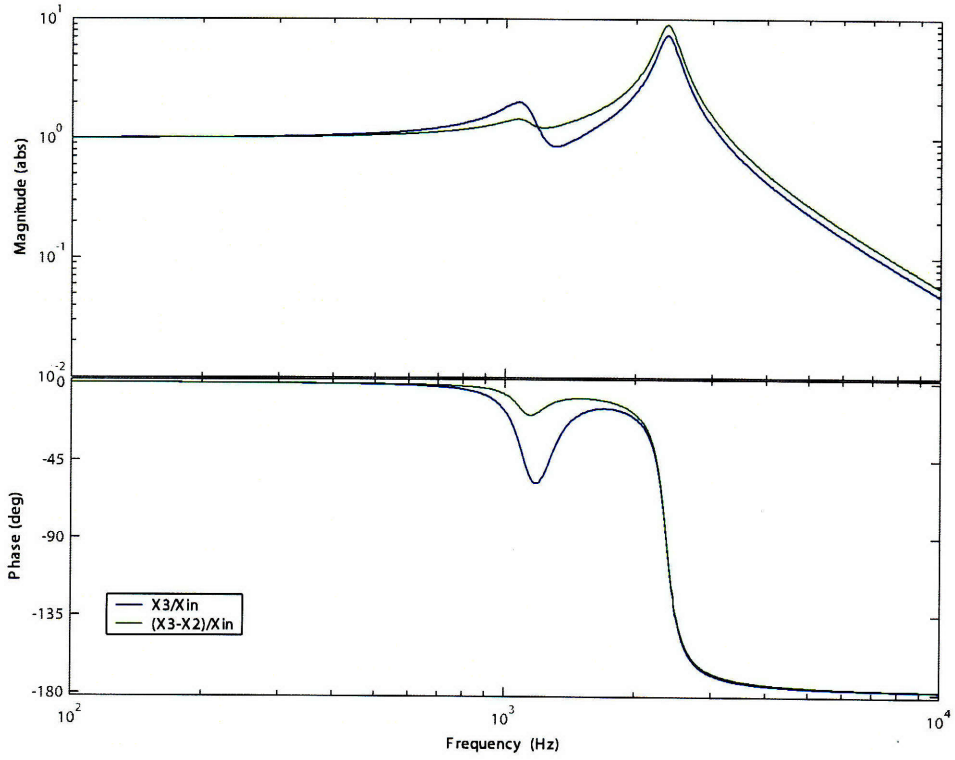

Figure 7-4: Bode diagram showing the theoretical dynamics of the absolute position of X_3 versus the differential position $X_3 - X_2$

7.2 Plant Experimental Results

The experimental results showed that the system was accurately modeled and well behaved. Our theoretical model matched the measured response by estimating the mechanical resonance at 2250 Hz and a pole-zero doublet at approximately 1250 Hz. The damping coefficients used in the theoretical model were selected to match those of the measured response. The system displayed no mechanical resonances or unexpected dynamics within the frequencies of interest we wish to control, namely between 10 and 1000 Hz. The measured response uncovered additional dynamics in the form of two poles at approximately 700 Hz. We believe the added dynamics are the result of a two pole Butterworth filter implemented by the capacitance sensors. The system also exhibited a time delay of 0.47ms believed as a result of details in the digitally sampled input voltages with the dSpace sampling frequency set to 8000 Hz. Figure 7-5 shows the plant transfer function of the system overlayed with a fitted response. Figure 7-6 shows the dSpace controller in block diagram format. We obtained the plant transfer function by using a dynamic signal analyzer specifically designed to work with dSpace software that was created by Katherine Lilienkamp[22].

7.3 Plant Modeling

The theoretical and measured data is combined to develop a model for the plant. The model of the position control loop is represented by the block diagram in Figure 7-7. The plant model starts with the control voltage generated in the dSpace software and ends with the voltage input into dSpace from the capacitance sensors.

We break down each block in the model starting with the high voltage amplifier. The amplifier multiplies the incoming voltage by 100 and supplies a maximum of 70mA. This current charges and discharges the piezoactuator. The actuator is treated as a displacement source directly turning voltage into displacement without any frequency based dynamics. The piezoactuator expands a maximum of 15 micrometers when 1000 volts is applied to it.

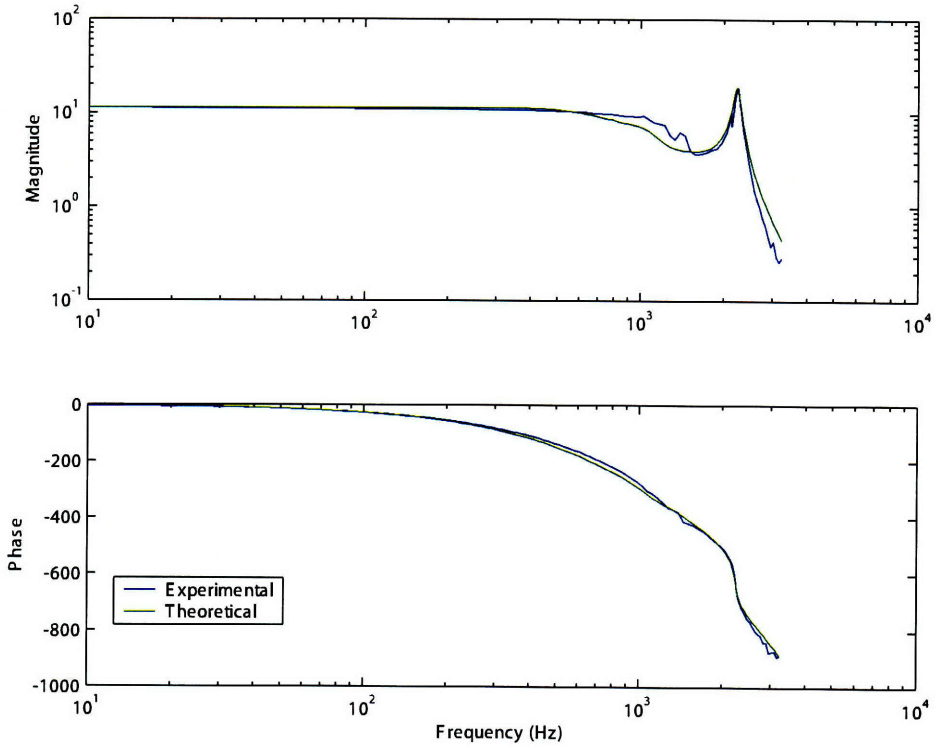

Figure 7-5: Bode diagram showing the measured plant transfer function of the AFM under position control contrast against the fitted values.

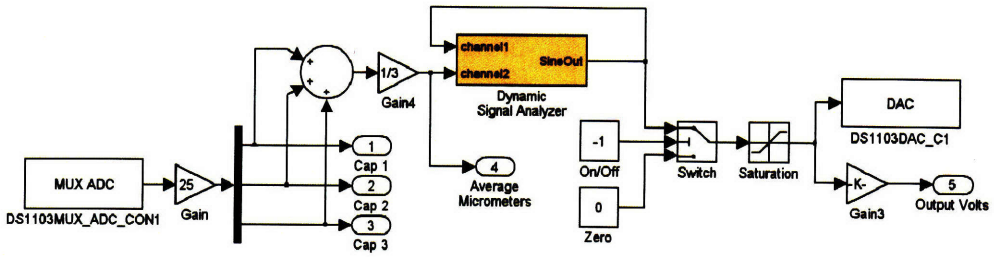

Figure 7-6: Block diagram of the dSpace configuration to import capacitance sensor readings and output a drive voltage to the piezoactuator while taking the open loop Bode plot of the system via Katherine Lilienkamp's dSpace dynamic signal analyzer.

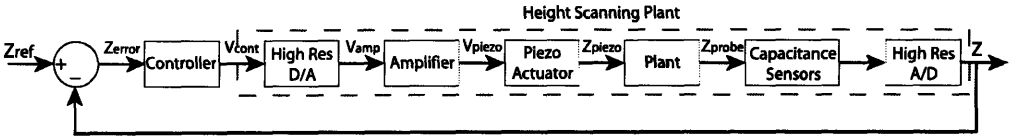

Figure 7-7: Block diagram of the position control loop. The plant is shown in the dashed box.

Secondly we characterize the dynamics of the plant. The dynamic equations presented in equations (7.1), (7.2), and (7.3) and the values in Table 7.1 are used to construct a model for the plant to relate the output position of the stage to the input position of the piezoactuator. These dynamics are factored into a their canonical form and represented in equation (7.4) in the Laplace domain. We found the damping ratio for the pole-zero doublet and mechanical resonance were 0.10 and 0.02 respectively.

$$\frac{X_{out}}{X_{piezo}} = \frac{1.86 \times 10^8 \cdot (s^2 + 2(.10)(7119)s + 7119^2)}{(s^2 + 2(.10)(6848)s + 6848^2)(s^2 + 2(.02)(14200)s + 14200^2)} \tag{7.4}$$

Additional plant dynamics come from the capacitance probes' electronics. The 8810 gaging module manufactured by ADE technologies are configured to 1 kHz bandwidth. The filtering electronics associated with the low pass filtering can be modeled as two real axis poles at 700 Hz.

$$H_{sensor}(s) = \frac{4398^2}{(s + 4398)^2} \tag{7.5}$$

The phase lag from the control board's discrete time processing is then added in to complete the simple model of the plant. From the measured data we estimated the time delay to be 0.47ms. The time delay does not change the magnitude of the plant but decreases by the time delay T_d multiplied by the frequency whereby

$$H_{delay}(s) = e^{-s \cdot T_d} \tag{7.6}$$

$$\phi_{lag} = -\omega \cdot 0.47ms \quad [rad] \tag{7.7}$$

Finally, we compile all of the fitted dynamics to achieve an accurate model of the open loop transfer function.

$$\frac{Z_s}{V_{Cont}(s)} = \frac{3.61 \times 10^{15} \cdot (s^2 + 2(.10)(7119)s + 7119^2) \cdot e^{-(0.47ms)s}}{(s^2 + 2(.10)(6848)s + 6848^2)(s^2 + 2(.02)(14200)s + 14200^2)(s + 4398)^2} \tag{7.8}$$

7.4 Controller Design

After measuring and modeling the plant dynamics we implement a controller to shape the loop transmission. We started with a simple integral controller and later added a lead compensator to increase the performance of the system. Both controllers were designed to attain a crossover frequency of 200 Hz and at least 30 degree phase margin. We present the two controllers sequentially in order to identify the problems that arose and the methodology that was used to solve them.

We began designing the integral controller by examining the plant response at 200 Hz, at which frequency the system has a magnitude of 10.9 and a phase of -54.6 degrees. Adding a pole at the origin caused the loop transmission to lose 90 degrees of phase at all frequencies. This resulted in a phase of -144.6 degrees at 200 Hz thus yielding a phase margin of 35.4 degrees. Adding the integrator decreases the magnitude of the system at 200 Hz or 1256 radians per second by a factor of 1256. Taking into account the original gain of the system and the attenuation of the magnitude by the integrator, we use a controller gain of 115.2 and thereby set the crossover frequency ω_C at 200 Hz. The system crosses through -180 degrees of phase at 333 Hz with a corresponding gain margin of 1.61. Figure 7.4.1 shows the theoretical and measured loop transmission dynamics for the plant and the controller. The integral controller is described by the following transfer function:

$$C_L(s) = 115.2\left(\frac{1}{s}\right) \tag{7.9}$$

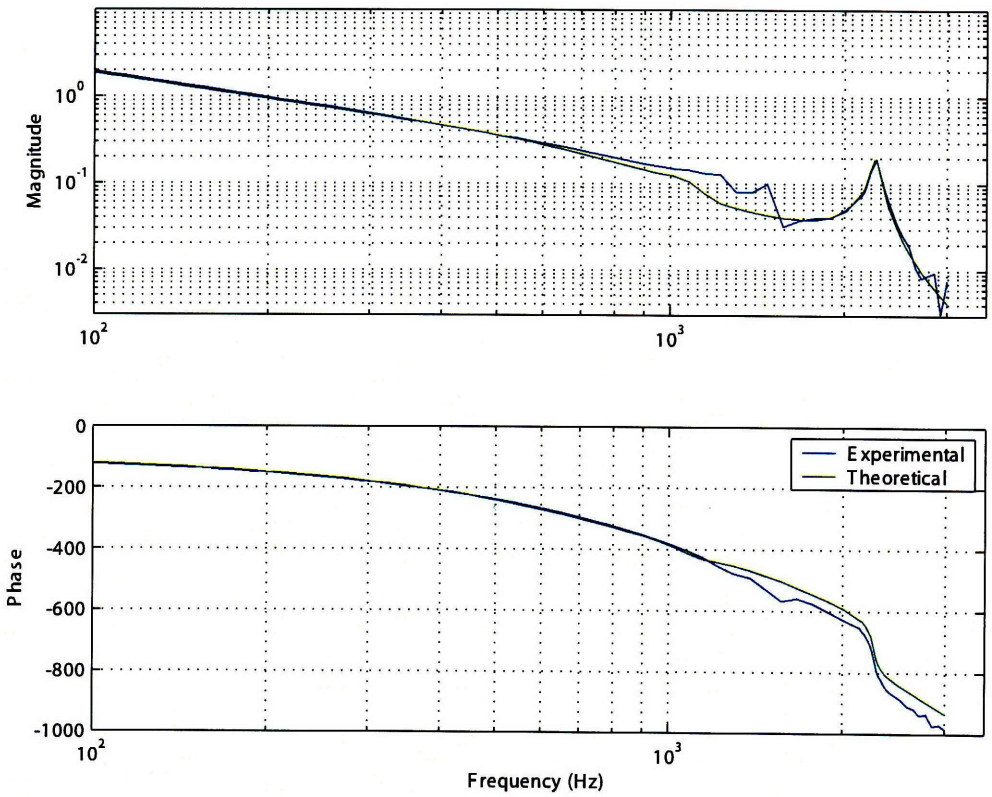

Figure 7-8: This Bode plot shows the loop transmission for using integral controller. The system shows a 198 Hz crossover frequency with a 33 degree phase margin and a gain margin of 1.61.

We found the performance of this system to be worse than anticipated. Firstly, we measured the phase margin to be 31 degrees which is less than the 35.4 degrees we expected. Secondly, the step response of the system showed less damping than that which is calculated for a system with 31 degrees of phase margin. We use equation (7.10) to calculate the expected damping coefficient ζ as a function of the phase margin [30]. By curve fitting the measured response against a second order model, we found that the system has a ζ equal to 0.215 and a natural frequency of 275 Hz. The measured damping ratio is 23% lower than the 0.28 value calculated by equation (7.10) found by using a phase margin of 31 degrees.

$$\Phi_M = tan^{-1}\left(\frac{2\zeta}{\sqrt{-2\zeta^2+\sqrt{1+4\zeta^4}}}\right) \tag{7.10}$$

We attribute the poor performance of our system to the unusually weak gain margin of 1.68. This substandard gain margin is the result of rapid phase loss at 200 Hz caused by 8 kHz sampling frequency analog to digital conversion. This nonlinear effect does not affect the magnitude of the loop transmission but causes the system to lose phase linearly with frequency. This loss of phase at an accelerated rate results in a smaller frequency difference between the crossover frequency ω_C and the frequency in which the system passes through -180 degrees ω_{GM} as compared to a linear system. Although the system decreases in magnitude at a rate of 20 dB per decade, the relatively small change in frequency between ω_C and ω_{GM} results in a small attenuation of magnitude and thus a weak gain margin. We measured the loop transmission of the system with a sampling frequency of 50 kHz, the highest frequency our PC-based digital controller would allow. We found the rate at which the system lost phase with respect to frequency $\left(\frac{\Delta Phase}{\Delta\omega}\right)$ at ω_C was 2.4 times greater when digitally sampling at 8 kHz as compared to 50 kHz. Had the system lost phase with respect to frequency at the 50 kHz rate, ω_{GM} would have been increased from 333 Hz to about 507 Hz resulting in an increase of gain margin from 1.61 to 2.34. Figure 7-9 shows the measured phase of the loop transmission of the plant and integral controller taken with an 8 kHz and 50 kHz sampling rate. The 8 kHz sampling frequency caused an

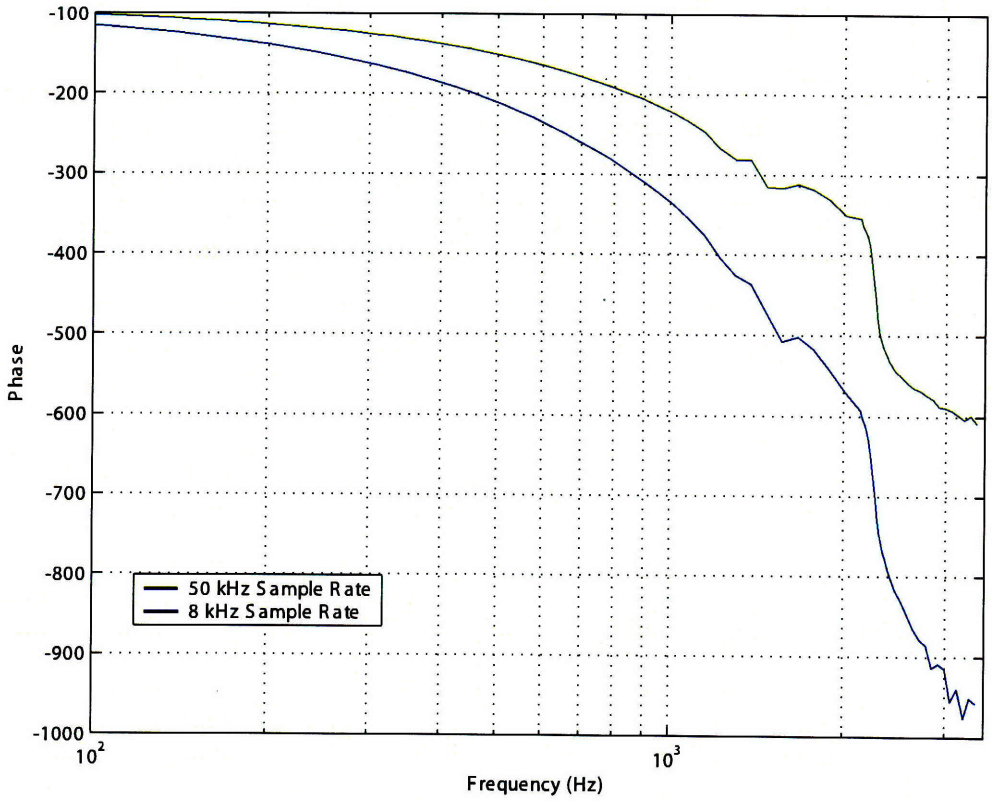

Figure 7-9: This graph displays the difference in the phase of the loop transmission of the plant and the controller while sampling at 8 kHz and 50 kHz.

accelerated rate of phase loss with respect to frequency in turn decreasing the gain margin. This lower than expected gain margin violated the assumptions made when calculating the damping ratio ζ as a function of the phase margin thus explaining the difference between the the measured and calculated vales of ζ.

We chose to use the 8 kHz sampling frequency in order to utilize high resolution analog to digital converters. The high resolution A/D converters output 20 effective bits which outperforms the 16 bit A/D converters that come standard with dSpace systems. In order to achieve this higher performance, the high resolution A/D converters oversample and then low pass filter the voltage inputs. This low pass filtering along with other processing operations limits the sample rate of the high resolution A/D converters to 8 kHz. As seen from Figure 7-9, this decrease in sampling fre-

quency subtracts substantial amounts of phase from a wide range of frequencies. We estimate that the loop transmission crossover frequency could have been increased from 200 to 800 Hz had we used the 50 kHz sampling frequency. We chose to sacrifice bandwidth in order to use these high resolution sensors based upon our project goals that focus on high accuracy metrology as opposed to high speed scanning.

A lead compensator was added to the controller to increase both the phase margin and the gain margin. The application of the lead compensator was somewhat unconventional for most lead compensators are centered around ω_C as to maximize the addition of phase due to the lead compensator at the crossover frequency. The lead compensator designed in this controller is centered around 1250Hz or six times ω_C. The zero associated with our lead compensator is located at 700 Hz and adds phase between 200 and 500 Hz without significantly increasing the magnitude over this range. This pushes ω_{GM} from 333 Hz to 376 Hz without decreasing the rate at which the magnitude rolls off with respect to frequency. As a result of the lead compensator we increased phase margin from 31 degrees to 42 degrees and improved the gain margin from 1.61 to 1.88. Fitting the step response of this system to a second order model, we find that the system has a ζ of 0.34 and a natural frequency of 317 Hz. Due to the increase in gain margin, the measured ζ is only 13% less than damping ratio we calculated to be 0.39 by using equation (7.10) which is an improvement from the 23% discrepancy measured with a lesser gain margin. Thus we have simultaneously increased the expected damping ratio and decreased percentage in which our measured ζ is lower than the expected value. The result of increasing the damping ratio from 0.215 to 0.34 is clearly shown in Figure 7-10 which plots the step responses of both controllers against each other. Figure 7-11 displays the theoretical and measured loop transmission Bode plot of of the plant with the second controller which incorporates the original integral controller and the additional lead compensator.

The placement of the pole in the lead compensator was as important as the placement of the zero. Upon the addition of the zero we increase the phase and magnitude

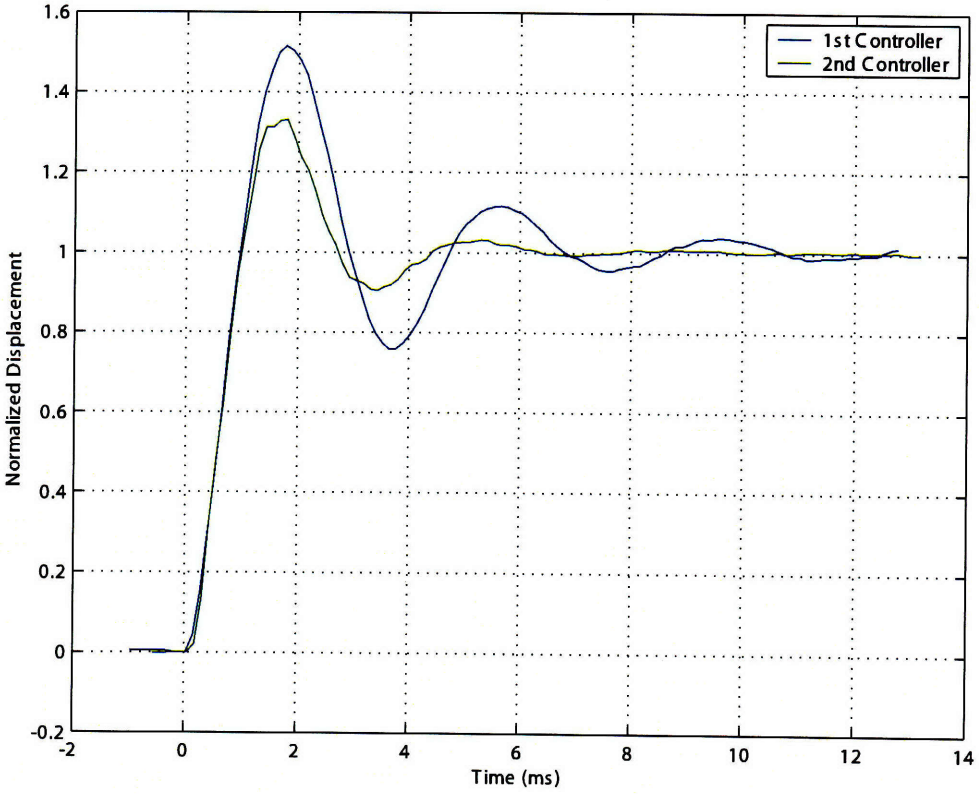

Figure 7-10: This graph shows the step responses for the nominal and improved controllers. The improved controller shows an increased damping ratio of 0.34 from 0.22 and higher natural frequency of 317 as compared to 275 Hz.

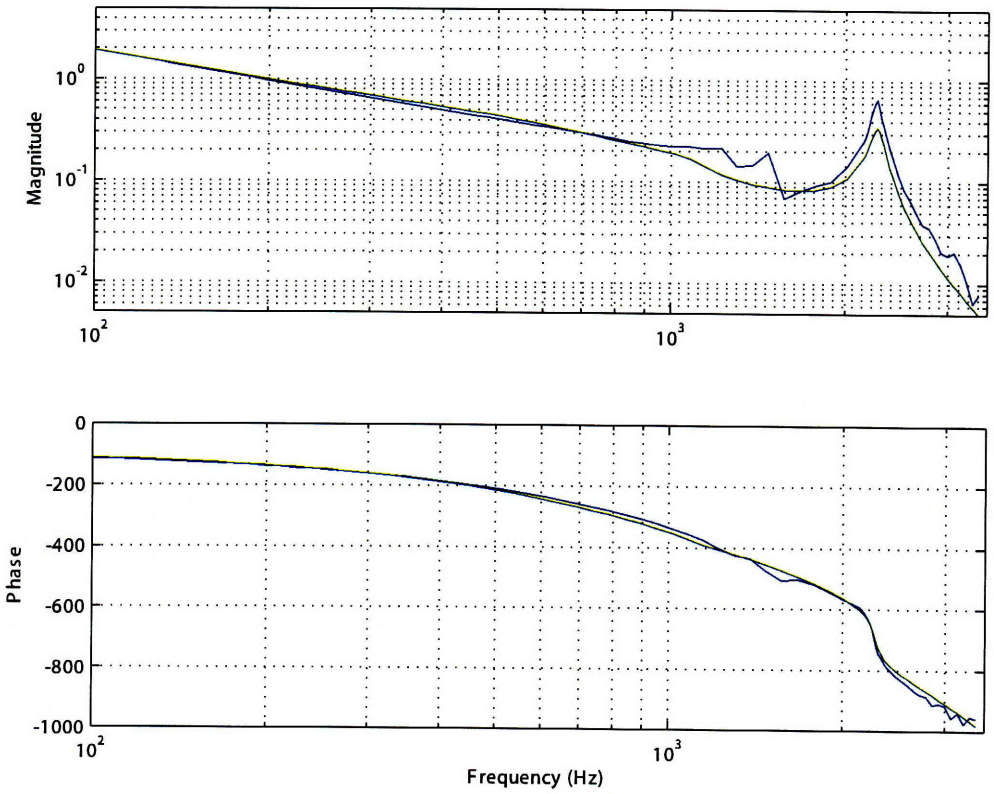

Figure 7-11: Loop transmission of the plant and final controller. The Bode plot shows a crossover frequency of 193 Hz, a phase margin of 43.5 degrees, and a gain margin of 1.88.

of the loop transmission beyond 200 Hz. This change in dynamics is of particular importance when assessing the stability of the loop as affected by mechanical resonance at 2250 Hz. We use the Nyquist criterion to verify the stability of the loop which requires that the loop transmission does not encircle the -1 point in the Nyquist plot. We locate the loop compensator pole at 2250 Hz to decrease the magnitude of the mechanical resonance and add 45 degrees of phase to nearby frequencies. This decreases the area encircled by mechanical resonance and shifts it 45 degrees clockwise on a radial plot thus drawing it away from the -1 point. This effect is more clearly demonstrated in Figure 7-12 which shows the on a radial plot the loop transmission of the system with the second controller. With both zero and pole locations for the lead compensator selected, we define the second controller in the Laplace domain with following transfer function. We then multiply the magnitude of the loop transmission by a gain of 358 in order to set the crossover frequency at 200 Hz.

$$C_L(s) = 358\left(\frac{1}{s}\right)\left(\frac{s+4398}{s+14200}\right) \tag{7.11}$$

With the second controller fully defined, we take a closed loop Bode plot of the combined plant and controller. Figure 7-13 shows that the system has a -3dB closed loop bandwidth of 450 Hz.

7.5 Noise Performance

In this section we report the noise in the position control system a final performance metric. The noise values are given as root mean square calculations away from an average value. The noise performance of the high resolution boards, capacitance sensors, and both positioning systems are displayed in Table 7.2. Although the second controller displays slightly better noise than the first, we believe the discrepancy is due to variance between samples. All of the noise measurements displayed in this table were taken on data that was averaged between the three capacitance sensors. Figure 7-14 demonstrates the magnitude of the noise with respect to one nanometer

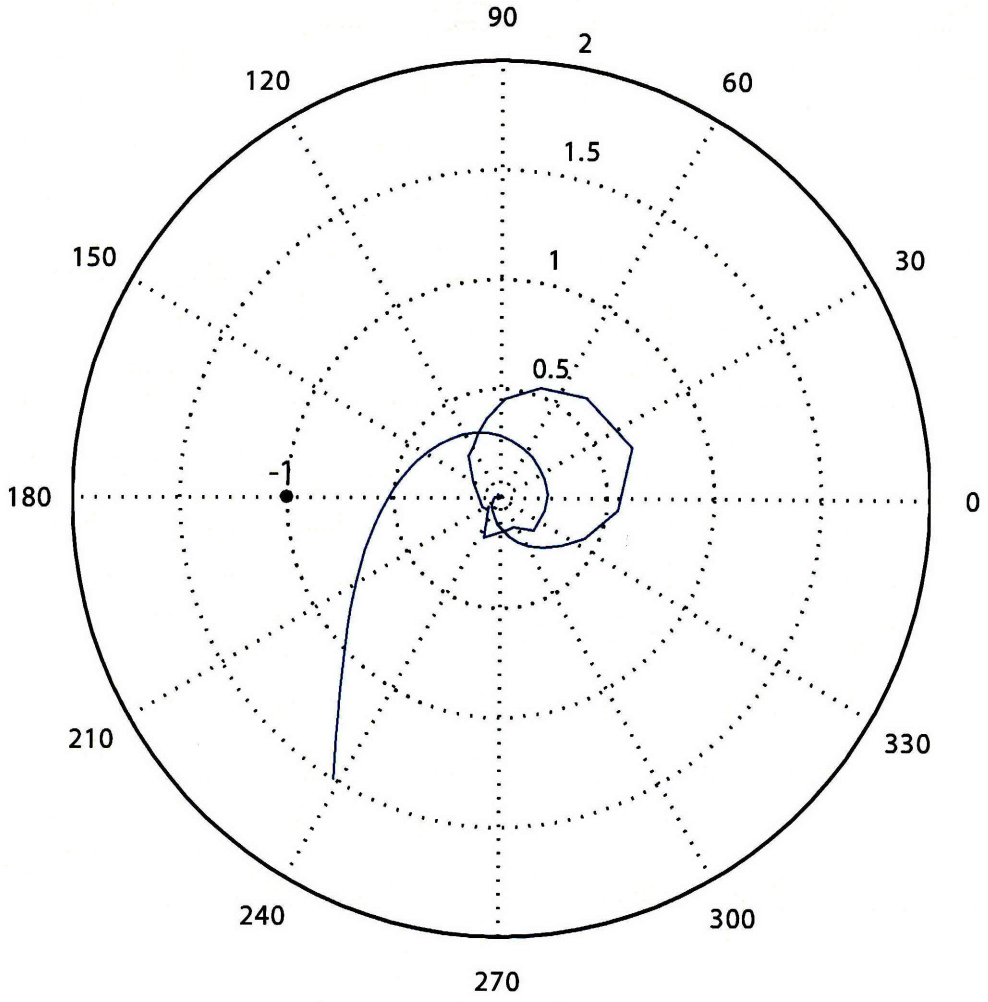

Figure 7-12: This figure shows the Nyquist plot for the loop transmission of the system and the controller. The loop created by the mechanical resonance at 2250 Hz has been shifted clockwise by 45 degrees in order to distance it from the -1 point.

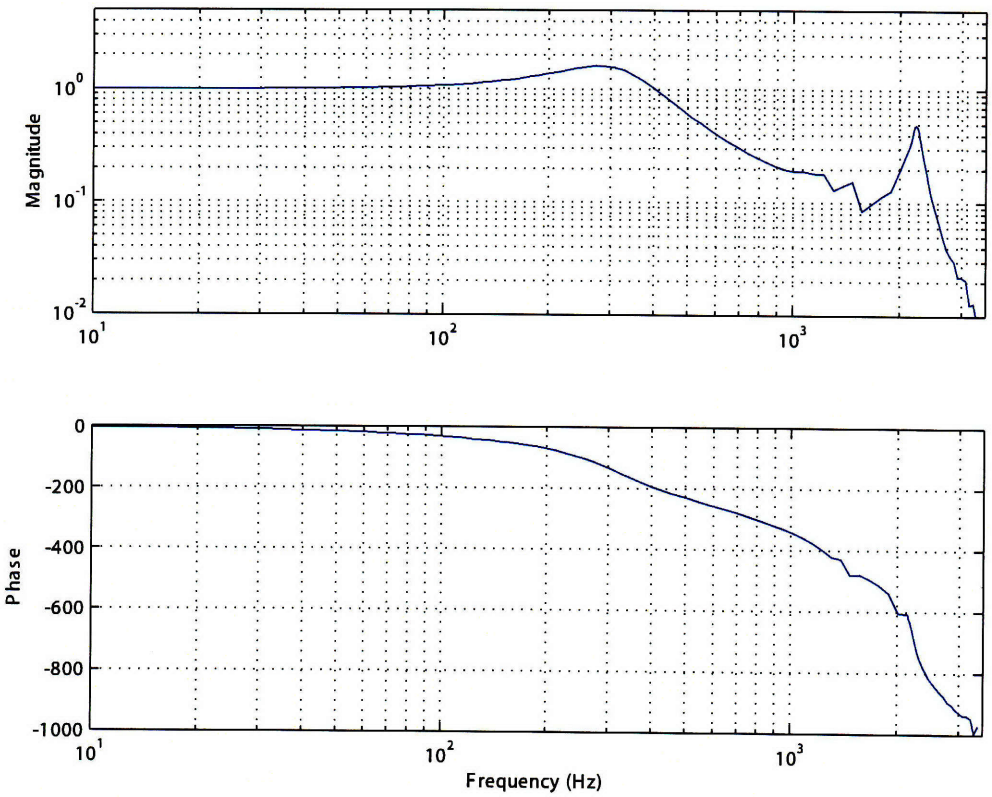

Figure 7-13: This Bode plot shows the closed loop transfer function for the second controller and plant. It demonstrates a closed loop bandwidth of 450 Hz based upon the -3dB point.

High Res Boards	Cap Sensors	1st Controller	2nd Controller
0.029 nm	0.170 nm	0.281 nm	0.249 nm

Table 7.2: This table displays the RMS noise of the position control system and capacitance sensors. Data taken with a measurement bandwidth of 1000 Hz.

by showing the response of the system to a 1nm step change in commanded position. The noise in the positioning system shows traces of 60 Hz signal which can likely be traced to the AC power supply. We believe with proper proper grounding or use of a differential amplifier this noise source can be eliminated to further reduce the noise in the position measurement.

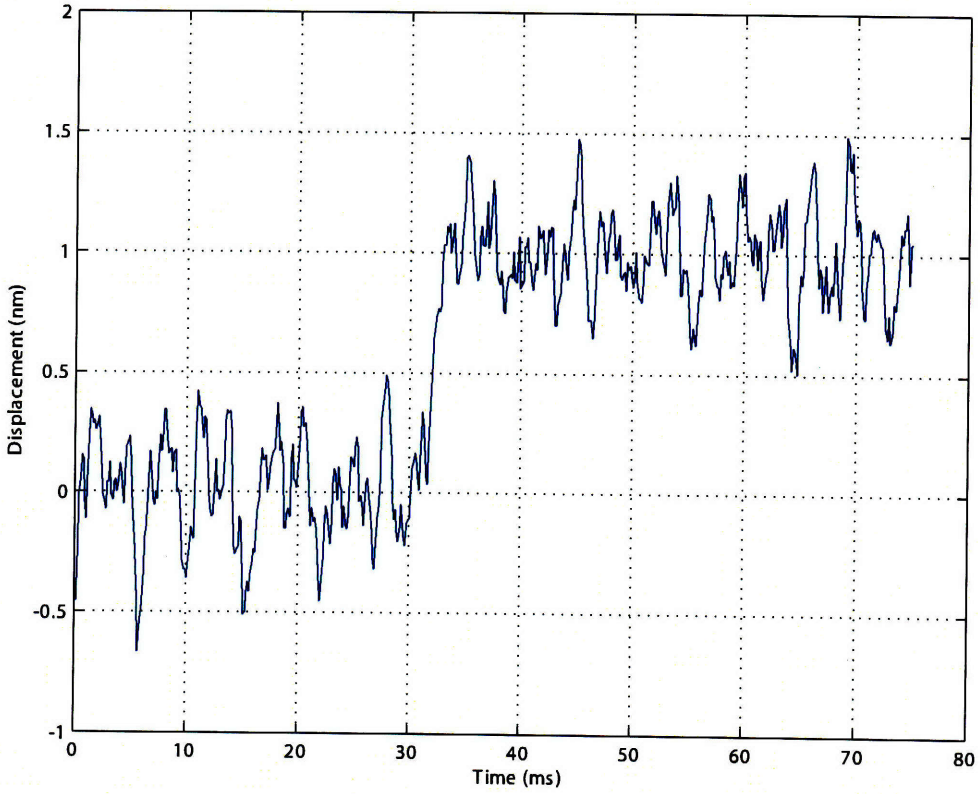

Figure 7-14: This graph shows the step response of the system to a 1 nm step change in commanded position.

Chapter 8

Surface Detection and the Akiyama Probe

The Akiyama probe is a newly developed sensor invented by Dr. Terunobu Akiyama and manufactured by NanoWorld AG. The mechanics of the probe that relate to its actuation and fabrication are found in [20] while notes upon its implementation and and characterization are detailed in [41]. Further documentation about the Akiyama probe can be found in [40] and [39]. The Akiyama probe is commercially available probe that offers potential improvements over previous atomic force microscope sensors demonstrated by Karrai and Grober in 1995 with the advent of their crystal tuning fork sensor. Both sensors use piezoelectric cantilevers which can be driven at resonance without requiring the use of a separate piezoelectric actuator. The removal of this mechanical dither simplifies the mechanical design and electronics implementation for the probe.

The innovation behind the Akiyama probe is based on technological improvements that make the probe easier to use. To make a crystal tuning fork sensor, researchers were previously required to individually glue a sharp-tipped optical fiber onto each tuning fork. In his Master's thesis, Aaron Mazzeo proposed a technique to simplify this process by holding the fiber with a Post-It note during the gluing operation [27]. The optical fibers are produced by pulling the ends of a strand apart while heating

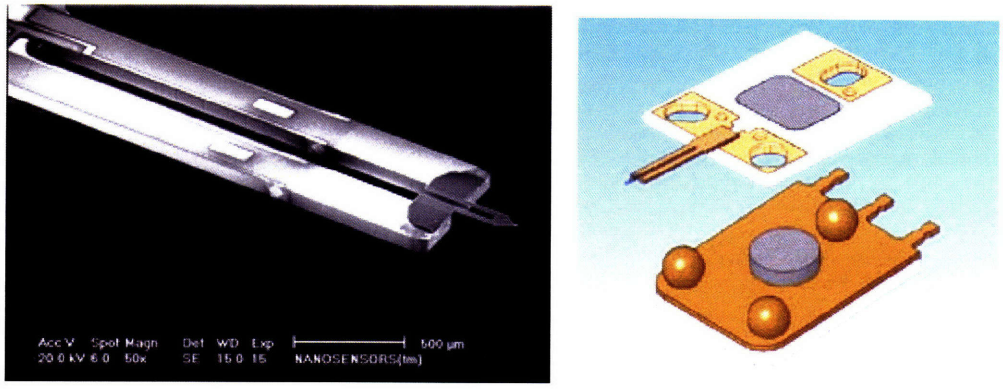

Figure 8-1: The first picture shows a microscopic view of the cantilevered beam with a commercial AFM tip glued to it. The second picture shows a CAD model of the Akiyama probe and its gold-tipped kinematic mount. Pictures taken from [39]

the center with a laser. As the fiber melts it gets drawn down to a small diameter. The result of this imprecise process produces tips with a tip radius under 1 μm and a fiber base diameter of approximately 50 μm. Alternatively, various companies have demonstrated the production of chemically etched 5-6 nm tips based from silicon cantilevers. Dr. Akiyama's product uses MEMS technology to glue the commercially produced AFM tips across the quartz tuning fork to achieve self excitable sensors with commercial grade repeatability. Furthermore, each probe is magnetically preloaded into a kinematic mount which allows for repeatable positioning. The six contact points of the kinematic mount are plated in gold and serve as a soldierless joint which greatly simplifies the process of replacing a broken probe. These mechanical features are displayed in Figure 8-1.

8.1 Surface Detection Theory

The atomic force microscope uses a quartz piezoelectric tuning fork to sense the sample surface. A sinusoidal voltage excites the tuning fork at its resonant frequency. The tip is brought within about 10 nm of the sample surface at which proximity the interatomic forces between the tip and the sample have a measurable effect on the tuning fork dynamics. The interaction introduces higher stiffness and a greater

amount of physical damping to the system causing the amplitude of the resonating tip to decrease and the phase between output current and input voltage to shift. The closed-loop circuit reacts to changes in the current to voltage transfer function in order to maintain a constant tip to sample gap.

We measure the current flowing through the probe in order to monitor its mechanical oscillations. The sensor has a finite amount of capacitance across its leads. The mechanical displacement of the fork generates a voltage potential by virtue of its piezoelectric nature. A change in voltage across the sensor's capacitive load causes a flow of current between its leads. Thus, the mechanical oscillations of the sensor are proportionally related to the amount of current flowing through it.

We used two different analog circuits to measure the current through the probe. The first circuit uses a current-to-voltage converter. The output voltage of the op amp shown in Figure 8-2a is proportional to the current flowing through the fork. The voltage is a product of the current through resistor R_3 multiplied by the resistance. The positive terminal of the operational amplifier acts as a virtual ground allowing us to measure the current through the tuning fork without imposing a drop in voltage. We assume that the voltage across the tuning fork is simply a fraction of the input voltage as determined by the voltage divider between R_1 and R_2 since R_2 is a relatively small value. The second circuit as shown in Figure 8-2b uses a differential amplifier to directly measure the voltage across the tuning fork. This direct metrology provides an accurate measurement of the voltage which, unlike the first circuit, is not subject to errors such as offset voltage or current bias across the op amp terminals. A second differential amplifier determines the current by measuring the voltage across a resistor placed in series with the tuning fork.

8.2 Results

The differential amplifier circuit was built and tested by Ross Ian MacKenzie. Figure 8-3 shows the current to voltage transfer function of the tuning fork while in a

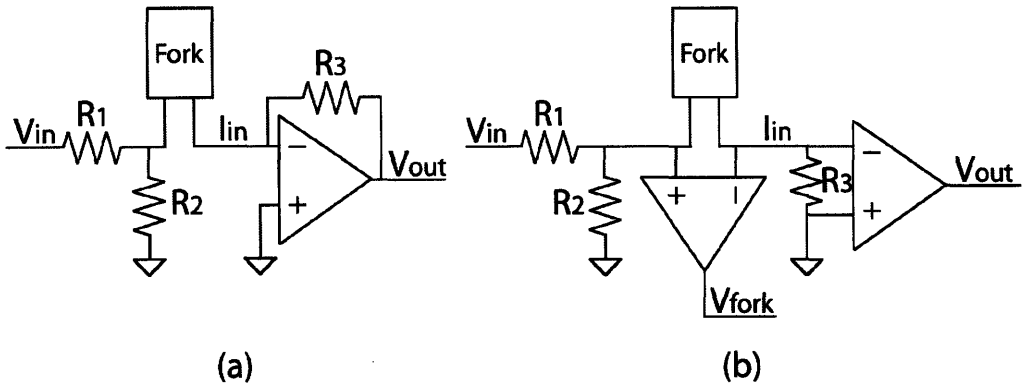

Figure 8-2: Electrical schematics to measure current via a (a) current to voltage converter and (b) differential amplifier.

closed can vacuum chamber and while open to atmospheric conditions. We first notice that the tuning fork exposed to the atmosphere has greater damping leading to less sharp changes in phase as well as more moderate resonant peaks. Secondly notice that the two transfer functions exhibit different natural frequencies. This discrepancy is not caused by environmental factors but instead because the tests were preformed on two different tuning forks.

We use the current to voltage converter in order to characterize the dynamics of the Akiyama Probe. A more complicated version of this simple circuit serves as the front end of a lock-in amplifier. This instrument has two outputs channels "X" and "Y" that represent the current to voltage transfer function as coordinates on a real vs. imaginary plane whereby

$$Magnitude = \sqrt{X^2 + Y^2} \tag{8.1}$$

$$Phase = tan^{-1}\left(\frac{Y}{X}\right) \tag{8.2}$$

We use the output from lock-in amplifier to generate a Bode plot of the current over voltage transfer function over a range of frequencies. Figure 8-4 displays three such frequency response plots. The red data shows the frequency response of the

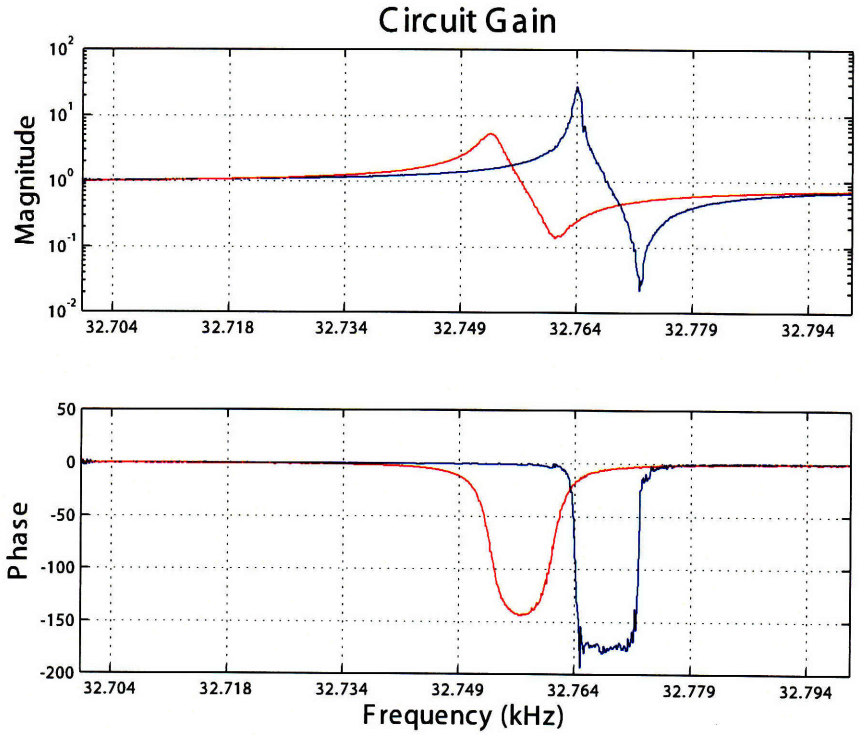

Figure 8-3: Open loop Bode plot of a crystal tuning fork both inside and outside its vacuum sealed cover.

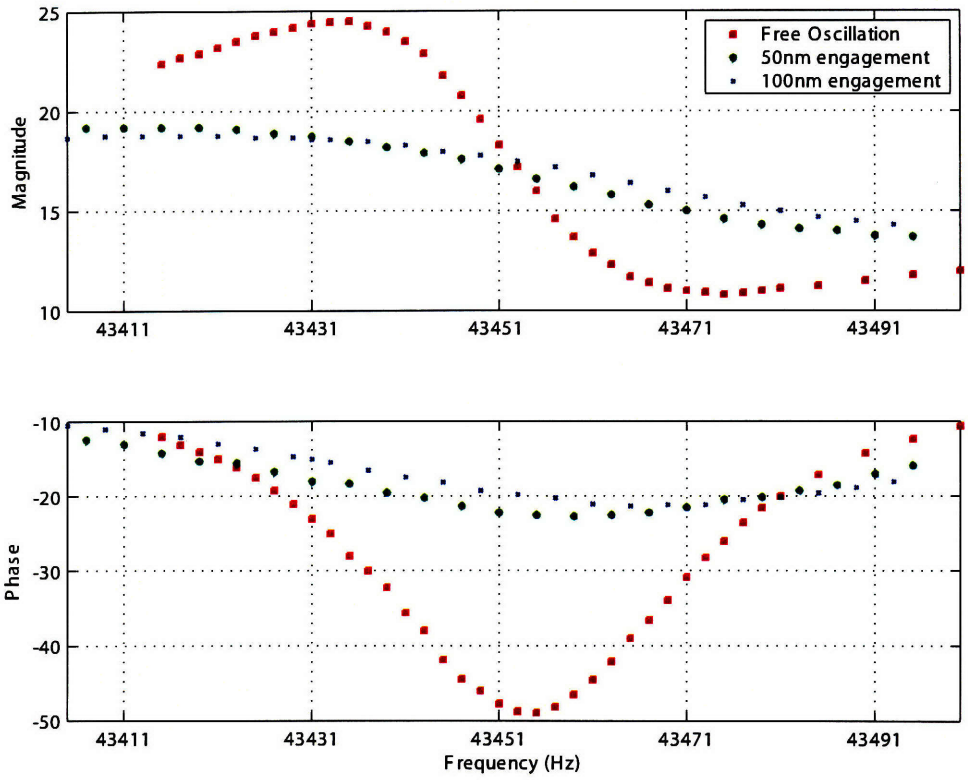

Figure 8-4: Bode Plot of the current to voltage transfer function as measured by the lock-in amplifier. The three curves represent the Bode plot for one probe while vibrating freely as well as engaged by both 50 and 100nm depth.

probe during free oscillation. The green data was taken while the probe was engaged at a 50nm depth and the blue data was taken at 100nm depth. The Akiyama probe exhibits more damping than the watch crystal tuning fork as evidenced by the Bode plot probably because the probe has a tip spanning the two tines of its piezoelectric fork.

The construction of each chemically etched tip varies from probe to probe. This variance affected two out the ten probes we tested resulting in defective behavior. The probe cantilever must have low stiffness in order to detect interatomic forces between the sensor and the surface. Non defective probes will have cantilever stiffness that are within specifications, while defective probes will have cantilever stiffness

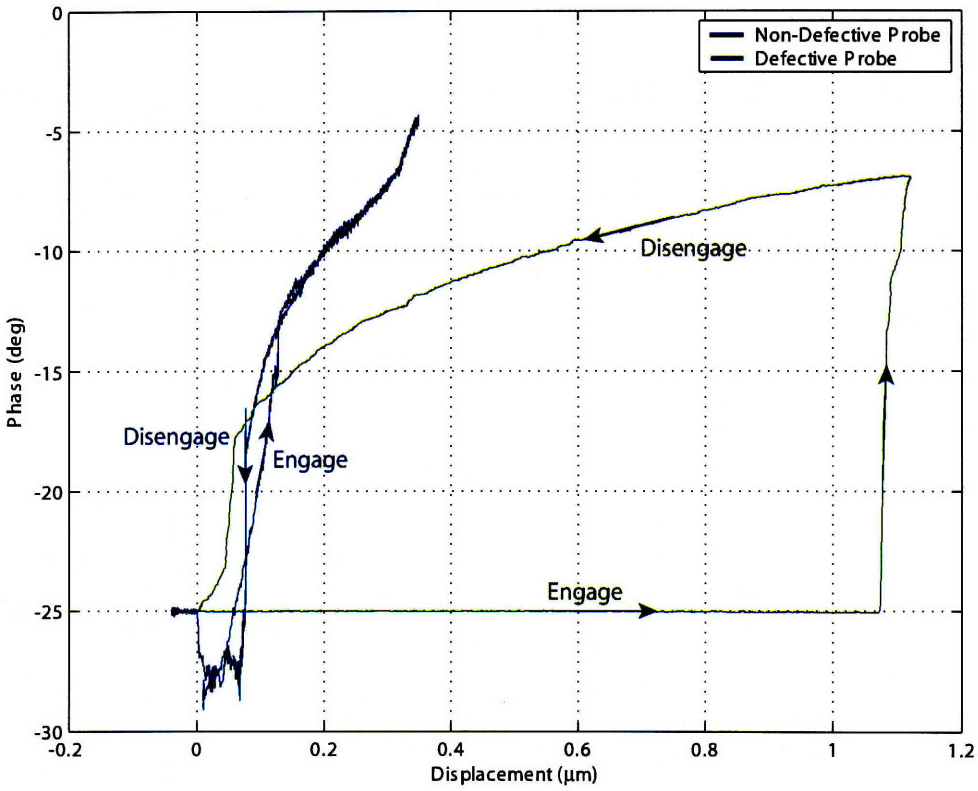

Figure 8-5: 2 axis plot showing the relationship between standoff distance and phase. The two curves signify two different probes with distinctly different behaviors. We notice as the probe nears the surface, the difference in phase between the voltage and current signals diminishes leading to a smaller negative value.

that are too low. The effect of this defect will cause the interatomic forces will overcome the spring force of the cantilever thereby creating a snap-in effect that draws the tip into contact. This leads to a hysteretic effect during engagement and disengagement. This is seen in Figure 8-5 which plots the phase signal from the lock in amplifier versus the proximity to the sample surface. The figure displays two phase versus engagement curves recorded from a defective probe and non-defective probe. Although the hysteretic snap-in effect is present in the behavior of the non-defective probe, it does not affect a significant portion of the range. The most linear and least hysteretic relationship exhibited by the non-defective probe between phase and displacement occurs between the range of -5 to -10 degrees of phase.

We chose to feedback the magnitude of the current to voltage transfer function as opposed to the phase. The phase measurement was found to drift up to ten times more than the magnitude. The drift presumably occurs because of temperature variations that affect the tuning fork. Although the drive signal remains at a fixed frequency, the natural frequency of the cantilever will change as the length, width, and thickness grow and shrink with thermal expansion. This change in frequency does not affect the magnitude as much as the phase because we operate at the resonant peak whereby small changes in frequency in either direction leave the magnitude relatively unaffected. Also, the phase exhibited noise at 1850 Hz the cause of which was not uncovered. To quell the noise in both the magnitude and phase measurements we used a low pass filter after the lock-in amplifier. The filter had two poles at 200 Hz with the following transfer function:

$$F(s) = \frac{1.58 \times 10^6}{s + 2513 + 1.58 \times 10^6} \tag{8.3}$$

We monitor and feedback the amplitude of the current running through the fork in order to track the surface of the sample. As the probe nears the surface, the amplitude of oscillation is damped. By regulating the system to maintain a constant amplitude, the probe to sample gap distance remains constant. Figure 8-6 shows the relationship between gap distance and amplitude of oscillation. Again we notice a snap-in hysteretic effect that draws the probe from an amplitude of 5.0 to 3.6 mV over a short distance. During the tests we specified that the amplitude remain within the linear region at 3.5 mV.

8.3 Sensor Modulated Height Tracking

In this section we describe the measurement and implementation of a feedback control system used to track the surface of a sample with the Akiyama probe. We combine the dynamics of the tuning fork and lock-in amplifier with the positional control feedback system derived in the previous chapter.

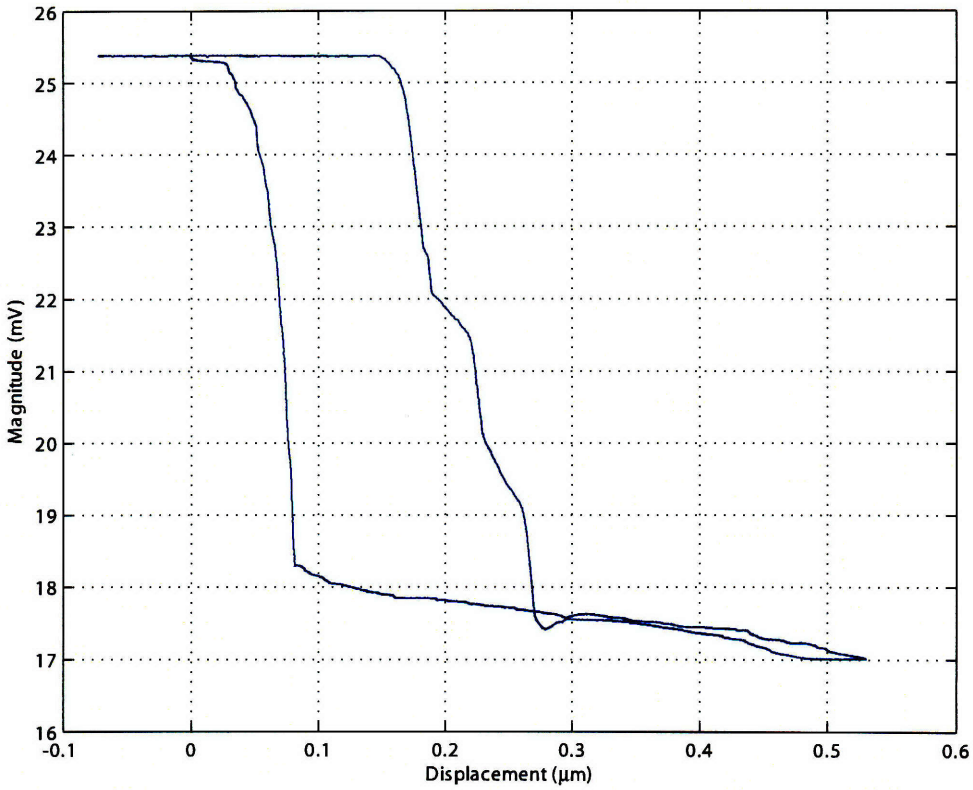

Figure 8-6: 2 axis plot showing the relationship between standoff distance and the magnitude of the current flowing through the sensor.

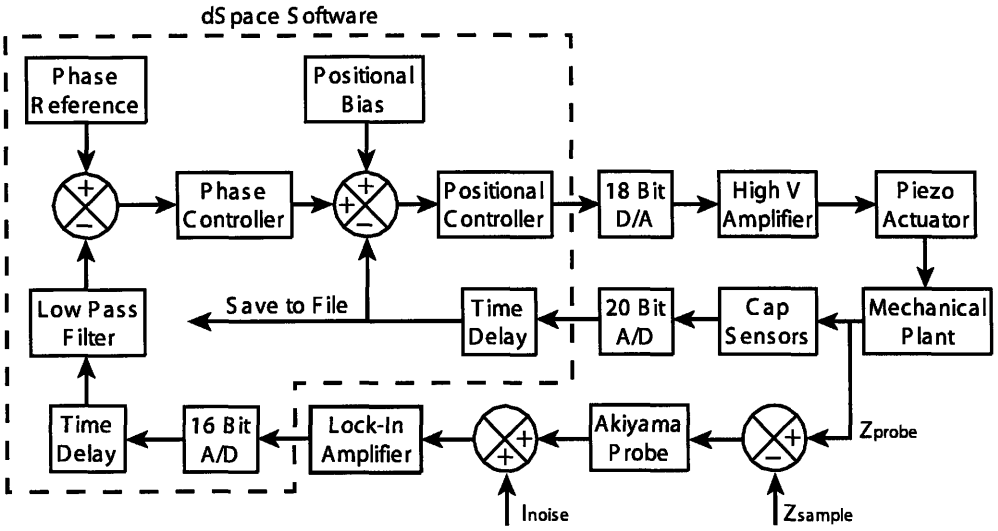

Figure 8-7: This figure shows a block diagram of the tracking system. The positional control feedback system designed and tested in the previous chapter has been integrated as a minor loop.

We incorporate the position feedback control system as a minor loop within the tracking system as is shown in Figure 8-7. If the bandwidth of the minor loop is substantially higher than that of the major loop, the minor loop will not add frequency dependent dynamics to the loop transmission. For this reason we maximized the bandwidth of the minor loop to 200 Hz. The minor loop works to hide the dynamics of the mechanical plant and the hysteresis of the piezoactuator. It also reacts to counteract other noise inputs such as thermal variance that affect the position of the moving stage.

We cannot directly measure the dynamics of the minor loop as they are implemented within the tracking system. The output of the minor loop is the z displacement of the probe, a quantity we measure by monitoring the output voltage of the capacitance sensors. Thus, the dynamics of the capacitance sensors which appear as two poles in the feedback loop of the position control system will act as two zeros in the tracking system. We capture these inverted dynamics as well as the frequency response of the lock-in amplifier and Akiyama probe by taking the loop transmission of the entire system.

The goal of the tracking system is for the capacitance sensor reading to accurately match the input height of the sample. Ultimately we are interested in finding the transfer function between these two variables. We cannot measure this transfer function given the current experimental apparatus for we have no way to accurately displace the z position of the sample as a function of time. This final test must be undertaken once the instrument is interfaced with the SAMM stage.

In order to take the loop transmission of the system and design a controller we must be able to sinusoidally drive one of the inputs. We first engage the probe onto a stationary target thus fixing the sample height and command the system to follow a sinusoidal change in the magnitude of current flowing through the sensor. In practice we would operate the instrument in the opposite manner in which the system would react to a sinusoidal change in the sample height in order to keep the magnitude fixed. While measuring the loop transmission we implemented a proportional magnitude controller with a low gain. This allows us to take the test while running the system in closed loop control limited risk of it going unstable. In this fashion we measured the following loop transmission shown in Figure 8-8.

This Bode plot shows that we can easily attain a open loop crossover frequency of 27 Hz with a 30 degree phase margin by simply increasing the gain by a factor of 12. The Bode plot also indicates that the magnitude signal is fairly noisy based upon the incongruities between measured points. We decided it was unwise to increase the gain on the controller until the noise in the magnitude measurement was identified and diminished. Applying high gains to noisy signals results in jumpy movements that can potentially break the Akiyama probes by rapid engagement with the surface. This noise on the block diagram is denoted at the summation junction before the lock-in amplifier labeled "I_{noise}." Because this noise is injected before the controller, it is deamplified only by the low pass filter. Using the sensor to track the sample surface, we find that the system holds a stable but noisy measurement resulting in 8.3 nm RMS of noise. The displacement of the sensor plotted against time while the probe is engaged with the surface is shown in Figure 8-9.

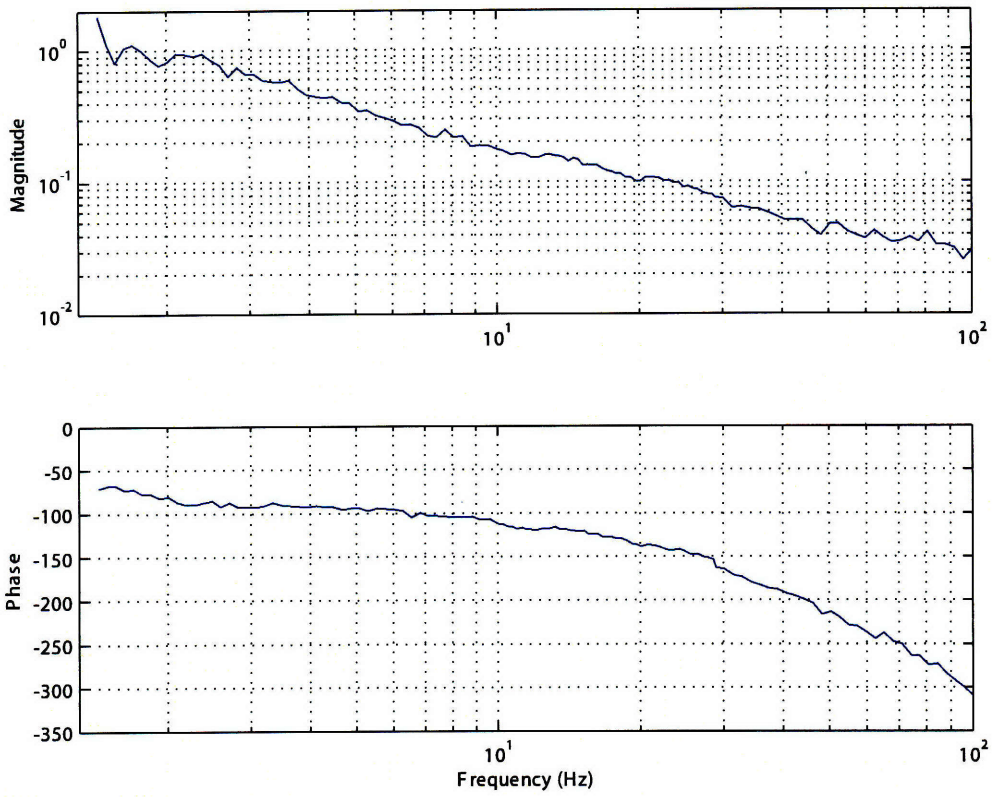

Figure 8-8: This Bode diagram shows the loop transmission of the height tracking system.

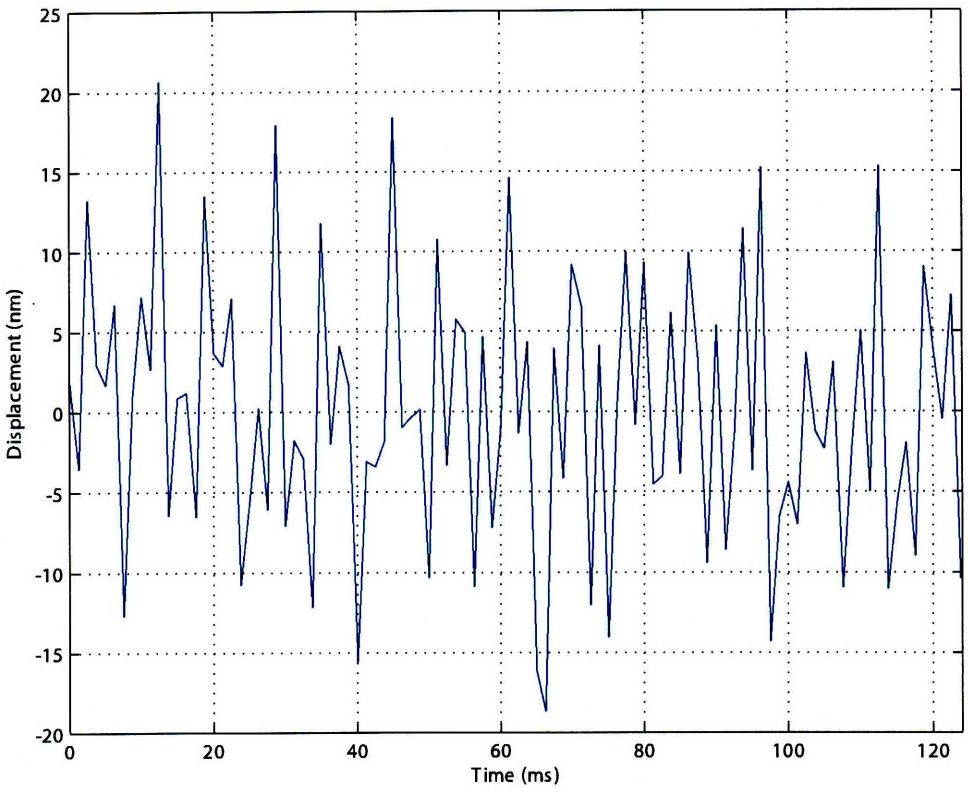

Figure 8-9: Plot showing the height of the sensor with respect to time while tracking a stationary surface.

Chapter 9

Phase Locked Loop

The phase locked loop is an electrical feedback system used in a wide variety of applications. The circuit was originally developed by Columbia University professor Edwin Howard Armstrong [33] who was later driven to commit suicide resulting from varied patent wars associated with the phase locked loop and the superheterodyne receiver. The phase locked loop can be used for advanced surface detection. This chapter will explain the basics of a phase locked loop and how it applies to our application. Labmates Ian McKenzie and Aaron Gawlik contributed to the understanding of the phase locked loop circuit through their assistance with the laboratory assignment worked through in this chapter [35]. Due to time limitations, the phase lock circuit was not experimentally tested with our probe system.

9.1 Theory

To understand and implement a phase locked loop it helped me to through a laboratory assignment written by Professor Lundberg at MIT presented in 6.331 Advanced Circuit Techniques [24]. An equally informative laboratory assignment written by Dragan Maksimovic in the University of Colorado, Boulder was used to gain understanding on the phase locked loop circuit. Working through these examples in the absence of any atomic force microscope related parts sets a firm foundation for understanding this complex electrical circuit. The assignment uses a Fairchild Semiconduc-

tor MM74HC4046 CMOS Phase Locked Loop chip. This inexpensive chip features many components of the phase locked loop all integrated into one small package. This section will use the laboratory assignment along with its supplementary notes to first give a review of the phase locked loop.

The theory behind a phase locked loop can be explained using a simple analogy. The purpose of the loop is for the circuit generate an output signal with the same phase as an unknown input signal. To accomplish this task, the loop electronically measures the difference in phase between the two signals and adjusts the frequency of the output signal to track phase. This is akin to two cars traveling around a circular track where the purpose of the driver in the second car is to visually measure the difference in position between the two cars and adjust the velocity of his car to track position. Thus, adjusting frequency to control phase is analog to adjusting velocity to control position. If two signals are held at the same relative phase from one another they will oscillate at the same frequency. Continuing the analogy, if two objects constrained to one degree of freedom are held at the same relative position from one another they will move at the same velocity.

The phase locked loop is comprised of three basic components: a voltage controlled oscillator, a phase detector, and a loop filter. A schematic detailing the pinouts of the PLL chip is presented in Figure 9-1. The voltage-controlled oscillator integrated into the Phase Locked Loop chip will output a square wave from 0 to 50 KHz whose frequency is linearly proportional to the VCO's input voltage on terminal 9. Although the input voltage is specified to range between 0 and 5 Volts, the output minimum frequency and range are programmable and defined by the equations 9.1 and 9.2.

$$f_{min} = \frac{k_1}{R_2 (C + a)} \tag{9.1}$$

$$Range = \frac{k_2}{R_1 (C + a)} \tag{9.2}$$

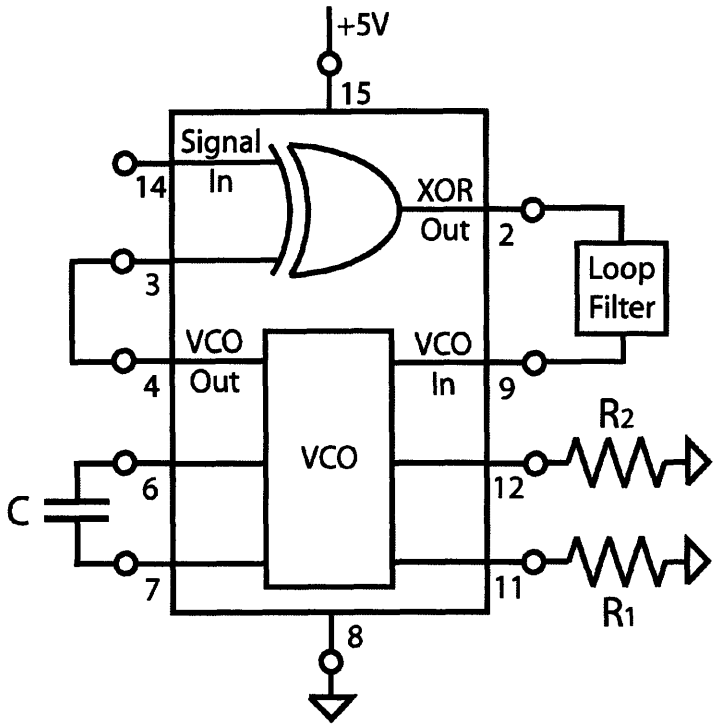

Figure 9-1: Schematic showing the pin out connections on the Fairchild Semiconductor 4046 PLL Chip.

It is suggested to choose R_1 and R_2 larger than 50 kΩ. k_1, k_2, and a are unknown constants experimentally determined by substituting in various values of R_1, R_2, and C. We measured these constants to be 1.81, 1.63, and 20.6pF respectively.

The next important parameter to calculate is the VCO constant K_o measured in radians/sec-volt. K_o is the proportional constant that relates the change in frequency to the change in input voltage and is calculated in equation 9.3.

$$K_o = \frac{\Delta f}{\Delta V} = \frac{Range \times 2\pi}{5V} = \frac{2.05}{R_1 \left(C + 20.6 \times 10^{12}\right)} \tag{9.3}$$

The next basic component of the phase locked loop measures the difference in phase between the output of the VCO and the input signal. The Phase Locked Loop chip has three different phase detectors incorporated into its hardware. The simplest of these detectors an XOR gate. Given two binary inputs, an XOR gate gives a binary output as defined by Table 9.1. The XOR gate will work most cleanly when its inputs

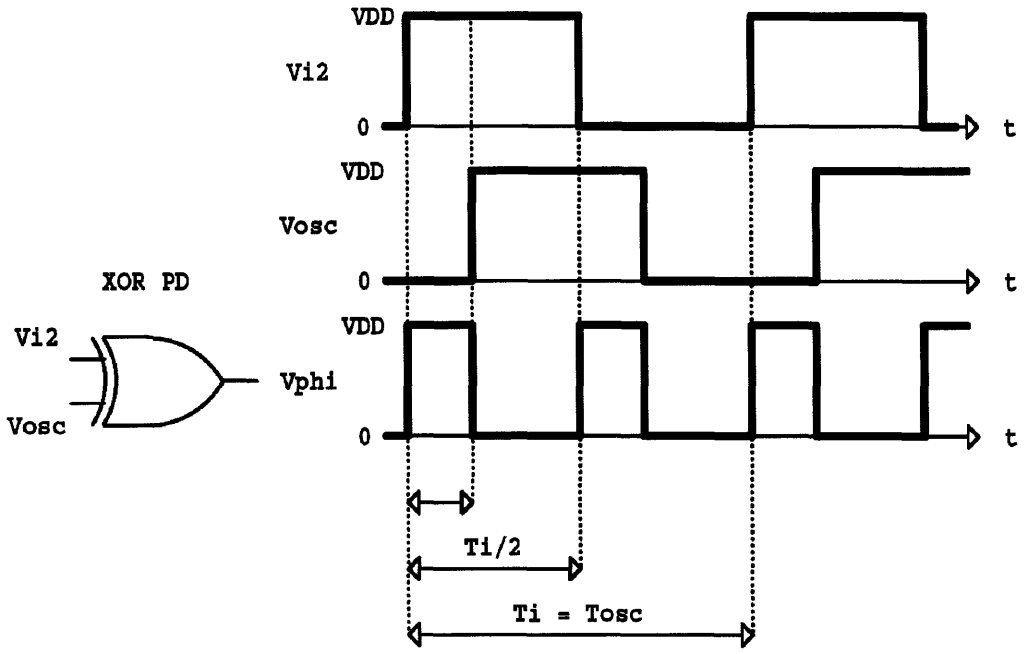

Figure 9-2: Diagram showing all three inputs and outputs of the XOR gate found in a PLL laboratory assignment from the University of Colorado, Boulder [26].

are square waves.

Input 1	Input 2	Output
0	0	0
0	1	1
1	0	1
1	1	0

Table 9.1: This table holds the binary input/output logic of an XOR gate.

When two signals of equal frequency are input through an XOR gate, the duty cycle of the output will be proportional to the difference in phase between the signals. We define the duty cycle of a binary signal as the fraction of the period in which the signal is high. This concept is more easily understood by examining Figure 9-2 which simultaneously shows the output of all three signals with respect to time. The example in this figure shows the output signal lagging the input signal by 40^o leading to about a 35% duty cycle. We find a linear relationship between the average output voltage of the phase detector and phase as shown in Figure 9-3.

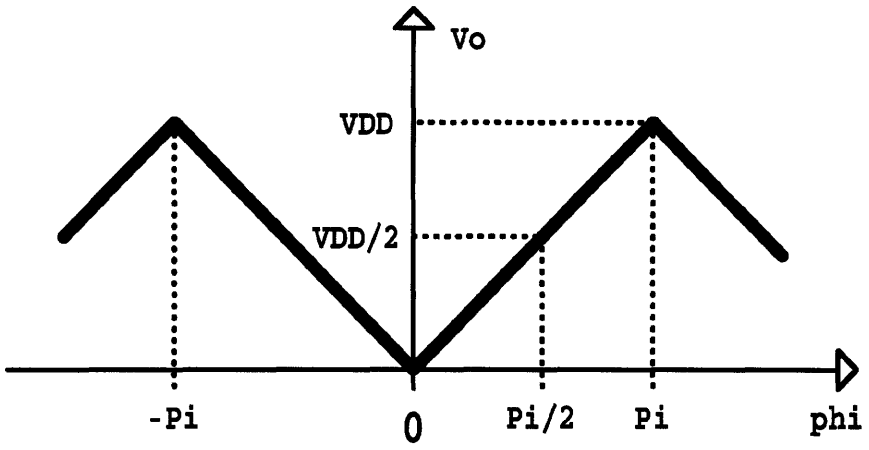

Figure 9-3: This graph shows the linear relationship between phase and average output voltage of the phase detector taken from [26].

There are a couple of points to note from Figure 9-3. First, we see that this type of phase detector is only capable of detecting phase between $0 \leq \phi \leq 180$ degrees. Secondly, we can use this graph to calculate the change in voltage with respect to the change in phase error. The relationship that defines this slope K_d is presented in equation 9.4.

$$K_d = \frac{\Delta V}{\Delta \phi_{error}} = \frac{5V}{\pi} = \frac{5}{\pi} \tag{9.4}$$

When comparing the phase between the two signals, we assumed that both signals had the exact same frequency. This condition is the goal of the phase locked loop but is almost never exactly satisfied. The phase error calculation only works when the mathematical inaccuracies posed by a discrepancy in frequency are small enough to assume the frequencies are the same. This ultimately leads to the concept of "lock range" which defines the maximum allowable difference in frequencies in which the system will still obtain lock.

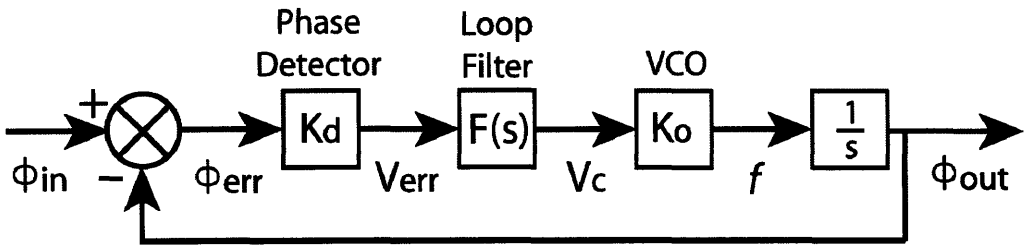

Figure 9-4: Block diagram of the Phase Locked Loop circuit.

9.1.1 Passive Filter

The last basic component of a phase locked loop is the loop filter. The loop filter inputs the XOR gate square wave output. The most simple of loop filters will simply average this signal though a low pass filter. The averaged signal is delivered into the input of the VCO thus completing the feedback control loop. A schematic of this loop is presented in Figure 9-4. The open loop gain of the system is presented in equation 9.5.

$$L(s) = \left(\frac{K_d K_o}{s}\right) F(s) \tag{9.5}$$

The integrator will subtract 90^o of phase to the open loop Bode plot. A single pole passive filter will subtract 45^o of phase at the corner frequency $\frac{1}{RC}$. Thus crossing over at the corner frequency of the filter will yield 45 degrees of phase margin. We want the corner frequency of the filter to be two orders of magnitude below the signal frequency for an 100 times attenuation of the high frequency signal. Had our signal frequency been 32kHz, the corner frequency and consequent bandwidth of the phase locked loop would be 320 Hz. Using a moderate value of 1 μF for C, we calculate R to be 500Ω. Lastly, we select the range so that the open loop Bode plot passes through unity gain at 320 Hz. Using the determined value for K_d we select K_o to yield a range of 1362 Hz. The resulting Bode plot of the open loop system is shown in Figure 9-5.

This system will have a steady state error in the phase between the input and

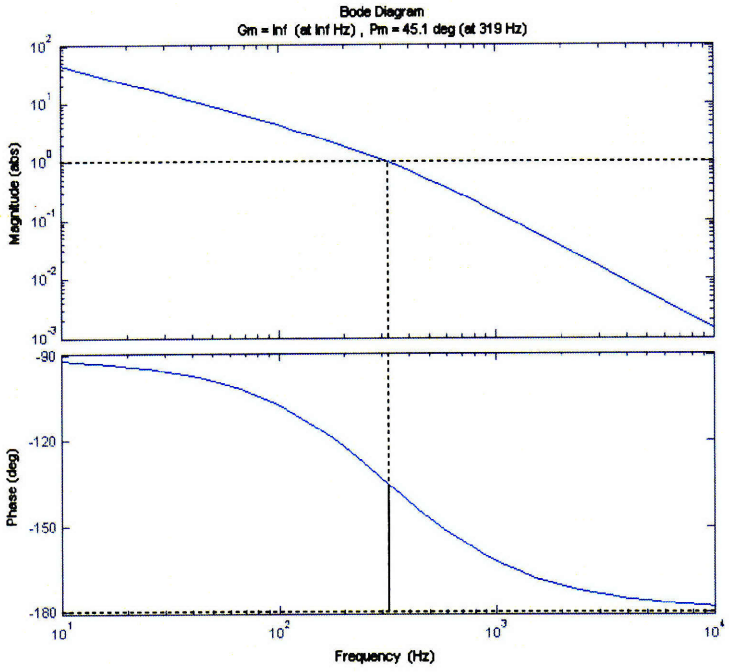

Figure 9-5: Open loop Bode plot using a passive loop filter.

output signals. This is evident by examining the hardware. The output of the phase detector represents error in phase between the two signals. The average value of this voltage as fed into the VCO is 2.5 V which translates into a steady state phase error of 90°. We apply closed loop control to the phase by modifying frequency. Our error signal increases as the integral of our control parameter thereby resulting in a ramp error output. Although the system has infinite gain at DC, it has only a -1 slope resulting in a steady state error when working with ramp outputs.

9.1.2 Active Filter

The next stage of the phase locked loop is to implement an active filter that will exhibit zero steady state error. We start by adding a pure integrator to the system which when coupled with the VCO brings the system to -180 degrees of phase for all frequencies. Simultaneously, we add a lead compensator centered around our desired bandwidth of 320 Hz that adds 45° of phase at its peak. Lastly, we select the gain in

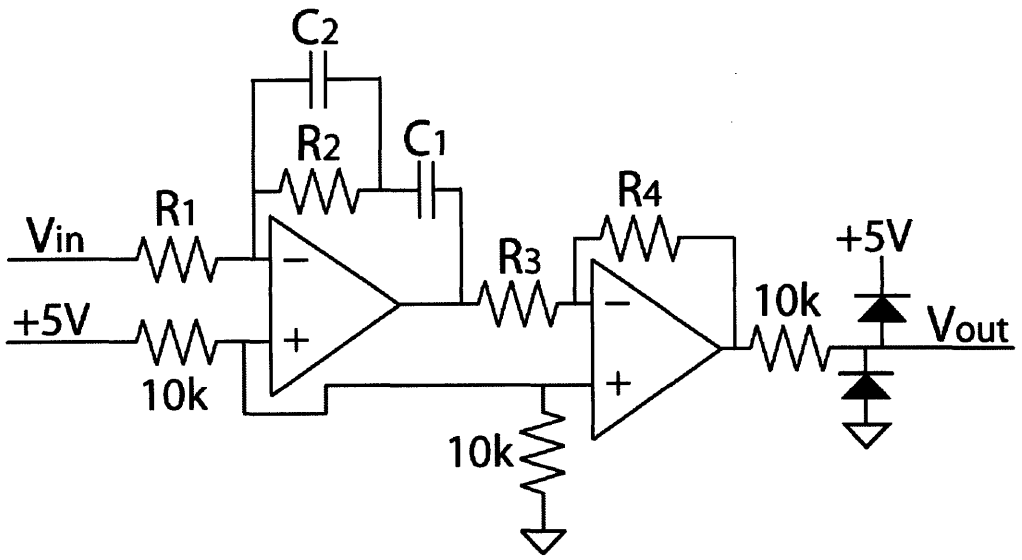

Figure 9-6: Electrical schematic showing the analog electronics layout for the active filter PLL.

order to force crossover at 320 Hz. This system will exhibit 45° of phase margin and a -2 slope at DC thus achieving both of our design criterion. Figure 9-6 shows the analog electronics associated with the loop filter while equation 9.6 gives its transfer function. To achieve the desired dynamics the first stage of the active filter uses an inverting amplifier configuration. The second stage stage is a unity gain inverting amplifier that returns the voltage to a positive value. The positive terminal of both stages are biased to +2.5 volts for that is the value required by the VCO at steady state. Lastly, a 10kΩ resistor is place in series to limit the current into the VCO while a diode clamp restricts the voltage to remain between 0 and 5V.

$$\frac{V_{out}}{V_{in}} = \frac{R_1 \cdot R_4}{C_1 \cdot R_3 s} \cdot \frac{R_2 (C_1 + C_2) s + 1}{C_1 R_2 + 1} \tag{9.6}$$

Next we must select the component and parameter values to set crossover at 350 Hz. We first choose the range to be 500Hz. Secondly, we configure the lead compensator based off of the generalized lead compensator transfer function. We find that an alpha of 6 will yield a maximum increase of 45° of phase. Beginning with a moderate value of C_1 equal to 1 μF, we find $R_2 = 185\Omega$ and $C_2 = 5\mu F$. Finally we set the gain by selecting R_1=R_4=50Ω and $R_3 = 1250\Omega$. Figure 9-7 shows the open

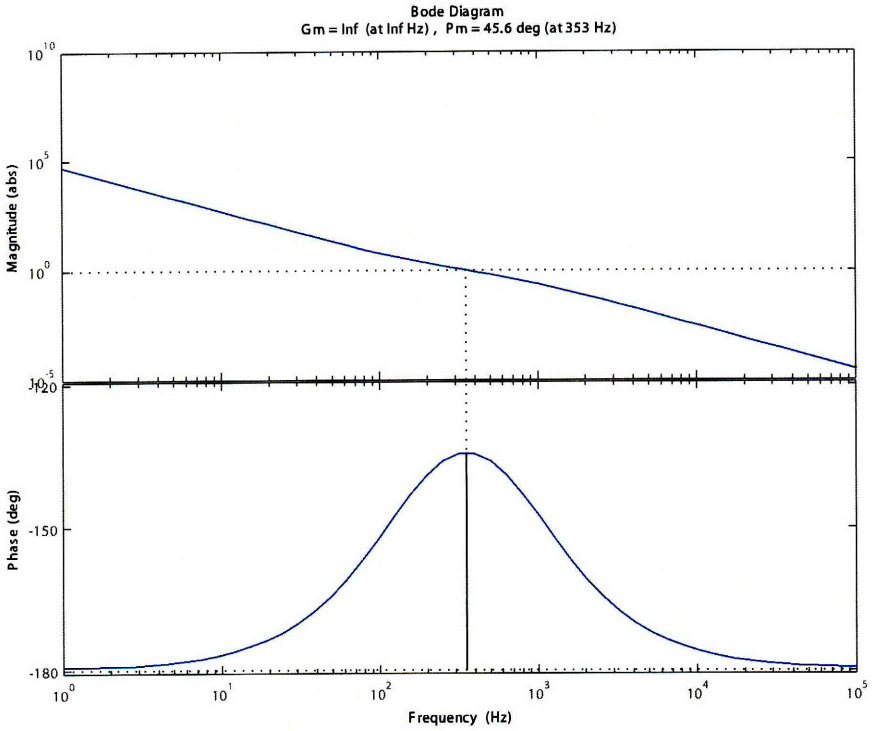

Figure 9-7: Open loop Bode plot of the active filter built for the PLL loop.

loop Bode plot of the active filter.

9.2 Hardware Implementation

The hardware we implemented to create a phase locked loop ultimately did not work properly. The design behind the hardware came from a paper published by K. Kobayashi et. al [21] in December, 2001 focussed on implementing a phase locked loop to excite a detector for dynamic force microscopy. This section will review the differences in implementation between the phase locked loop laboratory assignment and the hardware we built based on Kobayahi's work.

The overall layout of the phase locked loop circuit we created is shown in Figure 9-8. This qualitative diagram was used to conceptually understand the flow and processing of the varied circuit signals. It is evident from the diagram that this circuit

is inherently more complicated than the phase locked loop presented in the laboratory manual with the main difference being the concept of an "intermediate frequency." Although the sensor is being exited at 32kHz, the VCO output and phase detection operate the intermediate frequency of 4.5 MHz. The use of this higher frequency allows for more versatile signal processing, but it adds a host of complications to the circuit. The foremost necessity for the intermediate frequency is to attain compatibility with commercial VCO's which at their lowest limit output 1 MHz signals. The green arrows in Figure 9-8 indicate the signals that oscillate at the intermediate frequency.

This circuit requires the use of many otherwise unnecessary components that allow the shift between the signal and intermediate frequency. We use two sets of mixers and filters to step up and step down the frequency between the 4.5 MHz intermediate frequency and 32,768 Hz natural frequency of the probe. When two sine waves of frequencies f_1 and f_2 are multiplied together the resulting signal carries two signals at $f_a = f_1 + f_2$ and $f_b = f_1 - f_2$. To step down from the intermediate frequency we mix a function generator with output frequency 4.532 MHz with the 4.500MHz VCO to get a 32kHz signal overlayed with 9.032MHz noise. This large discrepancy between the two frequencies allows us to attenuate the noise by cleanly low pass filtering the signal. Conversely when we step back up to the intermediate frequency the 32kHz signal is mixed with the same 4.532 MHz function generator resulting in a 4.500MHz signal and 4.532MHz noise. We used a 4.5MHz ceramic bandpass filter to attenuate the 4.532 MHz noise but it did not substantially help with the noise reduction. Kobayahi argues that the 4.532 MHz noise does not pose a problem even if it were not attenuated because it is outside of the lock range.

After studying both implementations of phase locked loops it is clear that the use of Fairchild Semiconductor's PLL chip greatly simplifies the project. The best way to solve the noise problem bought about by mixing and filtering signals is to simply eradicate the need for an intermediate frequency. There are two dotted outline depicting different zones on the circuit diagram shown in Figure 9-8. The blue zone

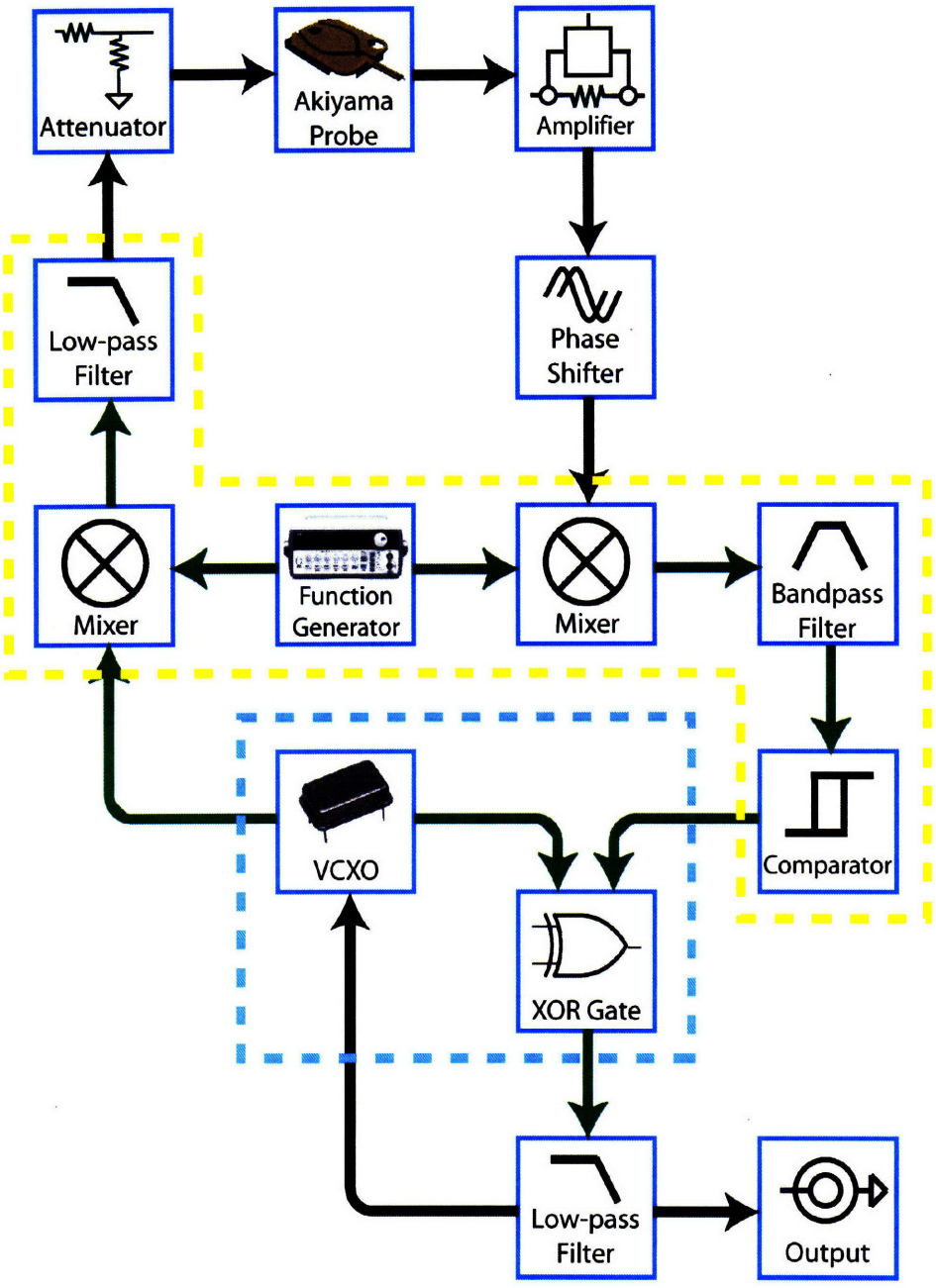

Figure 9-8: Quantitative schematic detailing the various signals and loops used in the PLL circuit.

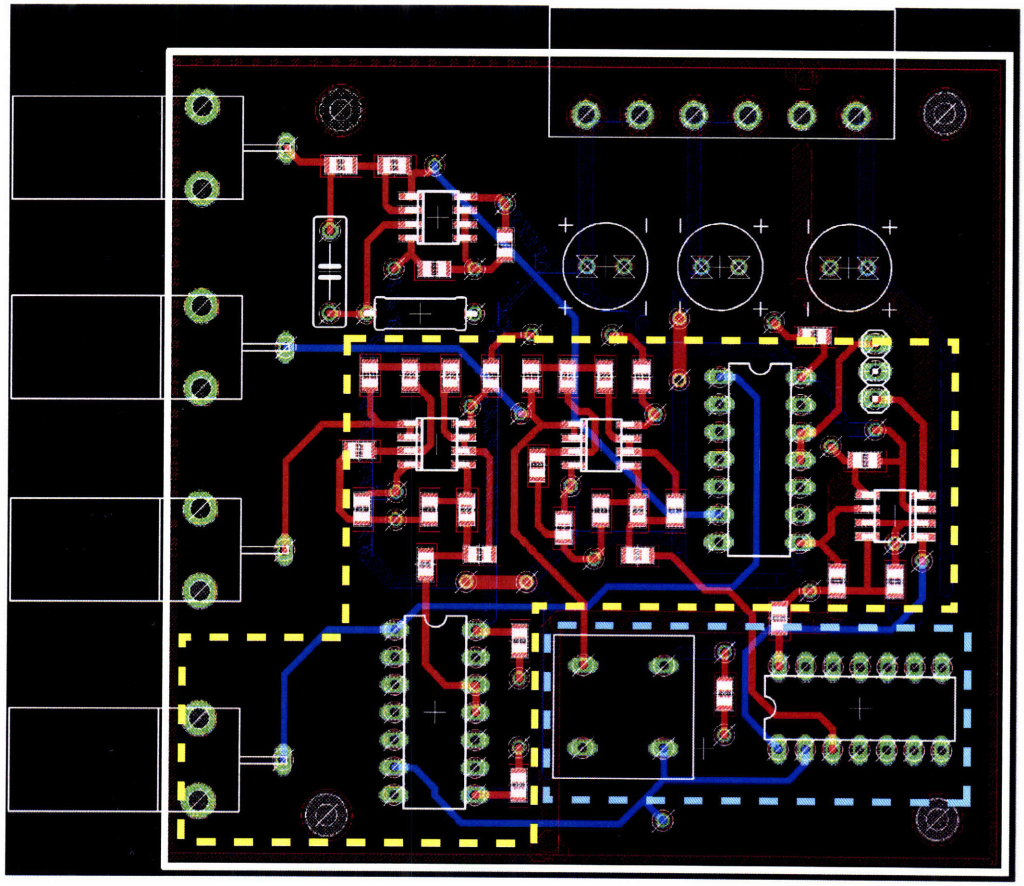

Figure 9-9: Layout of the printed circuit board with the yellow zone indicating obsolete parts and the blue zone indicating the PLL chip.

encircles the electrical hardware integrated into the PLL chip while the yellow zone encircles the hardware that the PLL chip renders obsolete. The same notation has been applied to the printed circuit board featured in Figure 9-9. This diagram shows the third of three printed circuit boards constructed to run the PLL circuit with minimal noise. As demonstrated by the PCB board in Figure 9-9, a compact PLL chip also eliminates the power lines and decoupling capacitors required to run the unnecessary mixers, active filters, comparators, and function generators that are used in Kobayahi's circuit.

9.3 Using the PLL chip to self-resonate an AFM sensor

In this section we present a method for using a PLL chip to create a circuit that will self-resonate an AFM sensor. We examine a circuit that is designed to work with the crystal tuning fork sensor as described in Karrai and Grober or tailored for the Akiyama probe. Although we have demonstrated a working Phase Locked Loop circuit with both active and passive filters, we did not experimentally test the following configuration which incorporates an atomic force microscope sensor.

The biggest change to the phase locked loop system upon the addition of a resonator is the source of the input signal. The phase locked loop presented in the laboratory assignment inputs a square wave specified by a function generator. The loop replicates that signal and sends it into the phase detector. We replace the function generated signal with the measured current flowing through the tuning fork. The phase locked loop will react to changes in either of these signals by increasing or decreasing the frequency of the replicated signal. Thus both the current and function generated signals act as unknown input signals.

Careful attention must be paid to the phase of the input signals to implement the loop correctly. The active loop will output produce a replicated signal that is in phase with the input signal at steady state. From chapter 8, we find that current lags the voltage by 70^o when using the crystal tuning fork resonator and by 30^o when using the Akiyama probe. Depending on which probe we are using, we must lag the replicated signal by either 30^o or 70^o before it is input into the phase detector. The loop will work to keep the two signals into the phase detector at the same phase which in turn will advance the voltage signal by a specified amount of phase ahead of the current signal. By adjusting the frequency of the voltage signal to achieve this difference in phase, the system will continuously find the resonant frequency of the probe. Figure 9-10 details a schematic which provides the basis of this system.

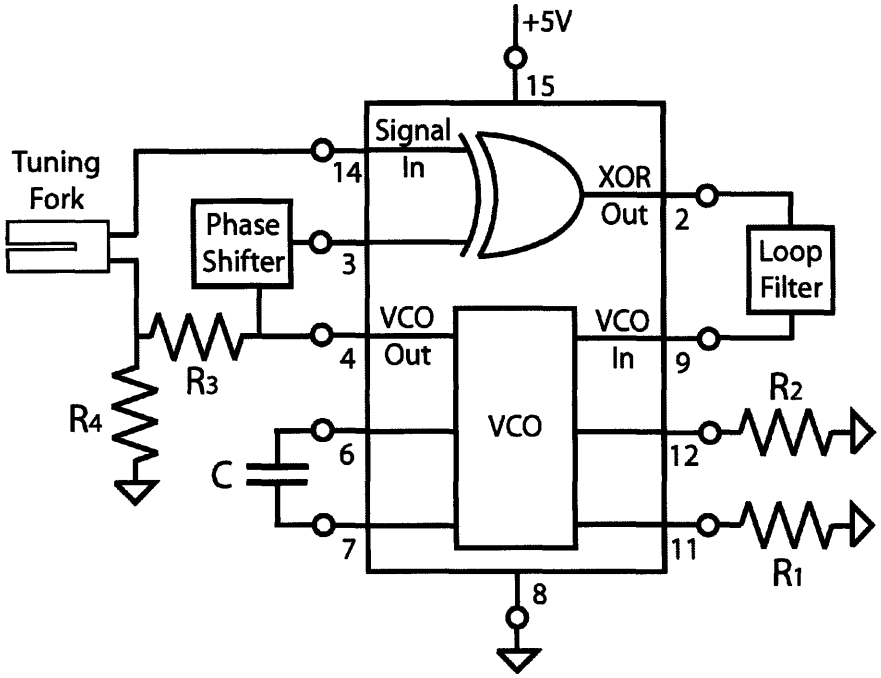

Figure 9-10: Layout of the printed circuit board with the yellow zone indicating obsolete parts and the blue zone indicating the PLL chip.

Chapter 10

Conclusions and Suggestions for Future Work

10.1 Summary

In this thesis we present an atomic force microscope that was designed to achieve subnanometer accuracy over 20 microns of range. The design was specifically tailored to interface with the Sub-Atomic Measuring Machine currently in operation at the University of North Carolina at Charlotte. The project began by building a simplistic nanopositioner in order to better understand the challenges of the project and gain experience with the mechanical and electrical components. We successfully implemented a closed loop feedback system that was able to control the position of the nanopositioner to one nanometer.

We then began work on the mechanical design of the atomic force microscope. A monolithic, one degree of freedom, flexure was designed to address many of the problems inherent to the first nanopositioner's motion guidance system. A second decoupling flexure is used in conjunction with the guide flexure to attain the desired accuracy. The relative stiffnesses between the decoupling and guide flexures theoretically guarantees the mechanical positioning error would be less than 0.6 nm. These mechanical systems along with the piezoelectric actuator, high voltage amplifier, 20

bit resolution converters, and low thermal expansion capacitance sensors were all successfully integrated into the instrument.

After manufacturing and assembling the hardware we developed the controls to regulate the axial height of the moving stage. We began by controlling the position of the stage by using the measurements from the capacitance sensors as feedback. High resolution A/D and D/A boards were successfully used and integrated into the project. The proportional integral controller we used set the crossover frequency to 200 Hz and demonstrated a -3 dB closed-loop bandwidth of 450 Hz. The controller held the position of the stage steady to 0.249 nm RMS positioning noise at a measurement bandwidth of 1000 Hz. We then implemented an Akiyama sensor feedback control system which demonstrated 8.3 nm RMS of positioning noise at a low crossover bandwidth. Advanced techniques to built a self-resonating circuit that monitors the Akiyama probe were explored.

10.2 Conclusions

Overall we are very pleased with the performance of the high accuracy atomic force microscope. There were many mechanical design parameters that preformed experimentally as they were designed to preform theoretically. In order to achieve the maximum resolution on the capacitance sensors, their range was set at $\pm$ 25 μm. The nonadjustable 50 μm range all three capacitance sensors needed to overlap by at least 30 μm in order to position the 20 μm range of the stage within these bounds. Had these range of the capacitance sensors not overlapped as closely as they did, we would have had to increase their range to 100 μm thereby doubling the noise floor and requiring a recalibration of the probes.

The guide flexure contained a host of manufacturing issues that were all well resolved over the course of the project. The complexity of the guide flexure coupled with the its thin features made it a difficult part to physically machine. Additonally, we were unsure if the proposed technique to pocket mill and then wire EDM cut the

back side of the flexures would provide well toleranced flexure legs by diminishing the chatter enough to leave a clean surface finish. In the end, the ten month lead time of the flexure was the only detail that did not go according to plan. This bottleneck pushed back the our timetable and which compromised our ability to reach all of the goals we hoped to finish by the end of the project.

There were many parts made of the project made out of Invar, a gummy and hard material of which neither the machinists nor I had much experience working with. After consulting industry experts we found a set of speeds and feed for various diameter drills and endmills which we were used on a light duty Bridgeport CNC mill to successfully and cleanly machine a variety of Invar parts. We were also uncertain if the 80 tpi fine thread screws and tapped holes could be made to work together out of Invar. The machinists at Central Machine Shop on MIT campus did an excellent job on both of parts and provided us with fully functional parts. Furthermore, we were pleased to find that the Titanium Nitride coating did not disturb the functionality of the screws.

The performance of the electrical feedback control systems was mixed. The 0.249 nm RMS positioning noise measured by the position feedback control circuit is eight fold better performance than the 2.0 nm RMS noise attained by the predecessor metrological AFM designed and built by Andrew Stein [37]. The 8.3 nm noise from the sensor feedback circuit was unexpectedly high but we remain optimistic that correct filtering and signal processing of the current signal can significantly improve the accuracy. Many improvements also can be derived by better understanding the dynamics and physics of the Akiyama probes. Although these probes were easier to use, their variance between manufactured probes, build quality, and overall durability leave something to be desired.

10.3 Suggestions for Future Work

10.3.1 Trueness Testing

The current experimental apparatus can measure precisely how far the moving stage displaces in the z direction and record its tip and tilt motions. Yet, we can only guarantee through theoretical calculations that the stage will remain within a 1 nm error budget with respect to lateral motions. To experimentally test the lateral accuracy of the microscope, we suggest first mounting onto the stage a cube with a precision ground surfaces or possibly a diamond cut prism.The test then would require a laser interferometer to be focused on the cube from orthogonal directions taking measurements while the piezoelectric actuator extended and retracted the stage.

This setup would also allow us to calibrate the instrument against against any repeatable tip and tilt errors. Ideally, the flexure stage will move perpendicularly to the face of the metrology head. To achieve this motion, the AFM body must be parallel to the metrology head. We set this parallelism by adjusting the three coarse approach screws to define the tip and tilt of the AFM body with respect to the metrology head. We would be able to use this experimental setup to measure the tip and tilt errors and adjust accordingly. We assume for the purposes of these tests that the faces of the cube run parallel to the movement of the stage. Any additional nonlinearities or hysteresis would remain as the lateral error of the flexure stage.

10.3.2 Measurement of Current Through the Tuning Fork

It is imperative to the accuracy of this instrument to identify and reduce the amount of noise injected into the probe current signal. The measurement itself is very sensitive and easily influenced by environmental factors. One source of noise at 8 kHz was identified as the beat tone frequency between the drive signal at 43 kHz and the electric field emitted by overhead fluorescent lights that have an electronic ballast with a switching frequency of 35kHz. It is recommended to build a small circuit on the atomic force microscope that amplifies the current measurement directly after

the tuning fork to safeguard this sensitive signal against noise. The specific lock-in amplifier used in the loop and its selected low pass filter will also play a large part in the noise performance of the height tracking system. The user manual from the Stanford Research Systems SR530 used in these experiments states that the current input has a floating ground which guards the measurement from noise on the ground line. The other half of the circuit is hooked up to the output of the signal generator which is also specified to have a floating ground.

We believe that the tuning fork will display enhanced performance by implementing a phase locked loop to automatically operate the fork at resonance. As indicated in Chapter 8, both the phase and magnitude measurements drift with time due to shifts in temperature or electrical parameters. The effects of these disturbance inputs would be tracked and counteracted with a phase locked loop.

10.3.3 Electrical Integration with the SAMM Stage

There are a number of issues that need to be addressed that upon transfer and integration of the AFM with the SAMM stage that affect the electrical systems of both instruments. Firstly, the PC-based digital controller must be reworked using National Instruments hardware and software. A National Instruments board was originally used in the SAMM stage for its compatibility with the laser interferometers. Although the dSpace system has historically been more robust, the National Instruments system has more extensive capabilities. The atomic force microscope can also benefit from a higher sampling rate to increase the bandwidth and phase margin at crossover. To do so, we would employ a field programmable gate array (FPGA) controller that is capable of higher sampling frequencies and which runs on the National Instruments but not dSpace systems.

Secondly, we must upgrade the systems used to conduct the electrical signals in and out of the chamber wall. One goal of the SAMM stage is to make all metrology measurements in a pure helium environment. The helium has good thermal conduc-

tive properties that will displace any heat gradients. Also, the laser interferometers can obtain higher accuracy if the medium they travel through is of low infractive index, as with Helium. To ensure that air does not seep into the chamber, all the signals must be connected using double-ended BNC vacuum feedthrough connections with floating grounds. The BNC outputs allow for reliable electrical connections between the electrical instruments inside the chamber. The capacitance sensors that we purchased have a BNC break in the line between the sensor and gaging electronics for this reason. It is important to use a floating ground feedthrough so that the noise from various signals and stray capacitance does not influence the analog signals. We suggest to use the vacuum feedthrough connectors provided by either ISI Insulator Seals or the Kurt J. Lesker company.

10.3.4 Mechanical Integration with the SAMM Stage

The integration of the atomic force microscope with the SAMM stage will require further attention to access the full functionality of the microscope. The project will require the purchase and installation of a borescope. The microscope has been designed to interface with a 7.3" long, 4.2mm diameter "Pro Slim" borescope manufactured by Hawkeye under the Gradient Lens Corporation. The aluminum borescope holder machined in this thesis was made to fit these dimensions. The top of the holder where the borescope flares out and seats is not yet machined and should not be until a particular borescope has been selected, purchased, and measured in length. The end of the borescope is optimally placed at a 2 mm working distance away from the target.

Additionally, there are a couple of mechanical items pertaining to the kinematic mounts that we suggest to update. Firstly, as covered in Chapter 6, we recommend plating the remaining three Invar screws with Titanium Nitride. This relatively inexpensive process will prevent cold welding between the Invar components. Also, we suggest to use the three bay fixture to align the kinematic mounts into position while they are being glued down to the SAMM stage surface.

Overall we are satisfied with the performance and results of the high accuracy atomic force microscope detailed in this thesis. We believe the follow on work to integrate the instrument into the SAMM stage has large promise to enhance the field of accurate AFM metrology.

Appendix A

Mechanical Drawings

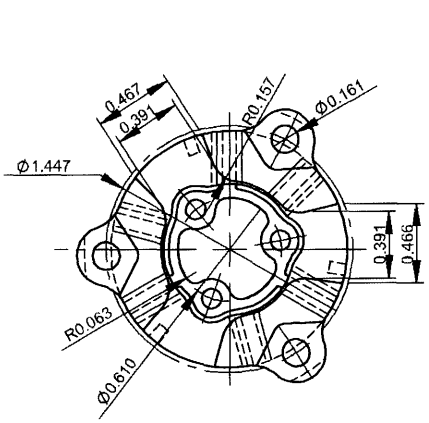

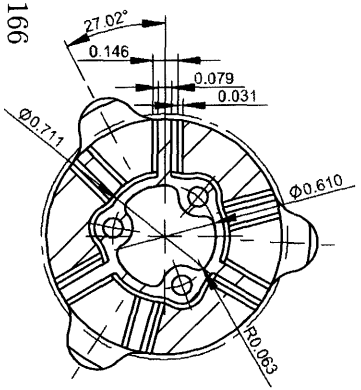

SECTION V-V

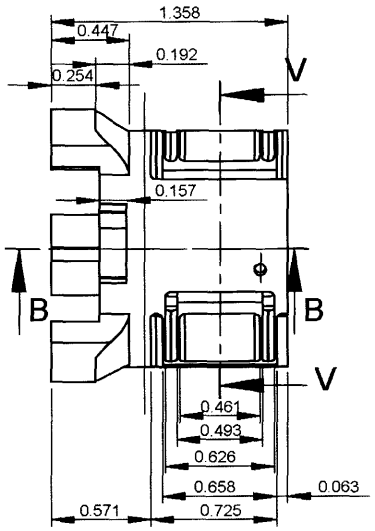

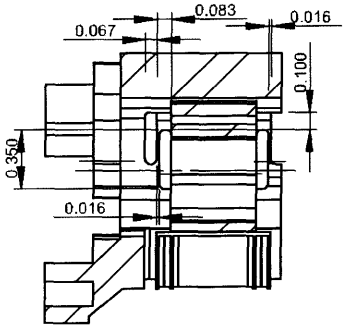

SECTION B-B

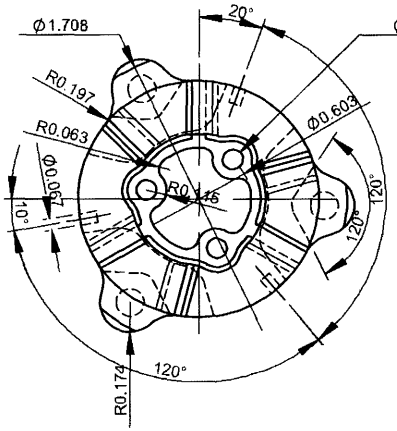

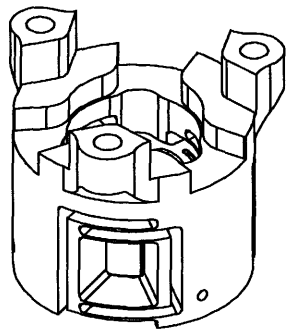

166

MATERIAL:

NOTES:						
1. DIMENSIONS ARE IN MM UNTOLERANCED DIMENSIONS ARE BASIC					DRAWN:	DJK
					DATE:	10/26/2007
		.	.	.	SCALE:	1:1
2. INTERPRET GEOMETRIC TOLERANCING PER: ASME Y14.5M – 1994		.	.	INITIAL RELEASE FOR CONSTRUCTION	CHKD:	.
	REV	DATE	BY	DESCRIPTION	APVD:	.

Massachusetts Institute of Technology
Precision Motion Control Laboratory

DWG. TITLE: Guide Flexure

DWG. NUMBER | REV.

SHEET 1 OF 1 | SIZE A

5 4 3 2 1

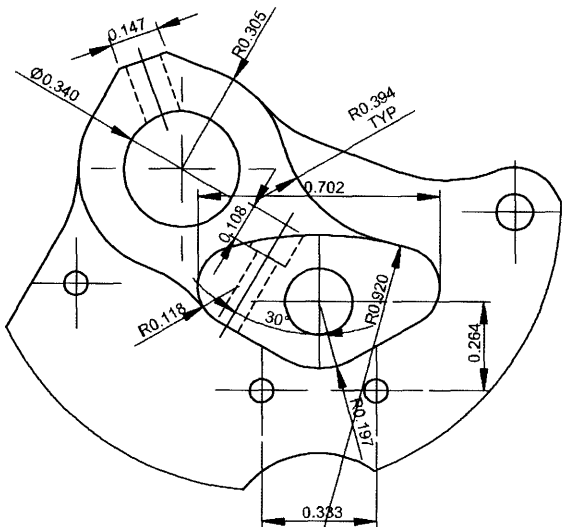

DETAIL A
SCALE 2 : 1

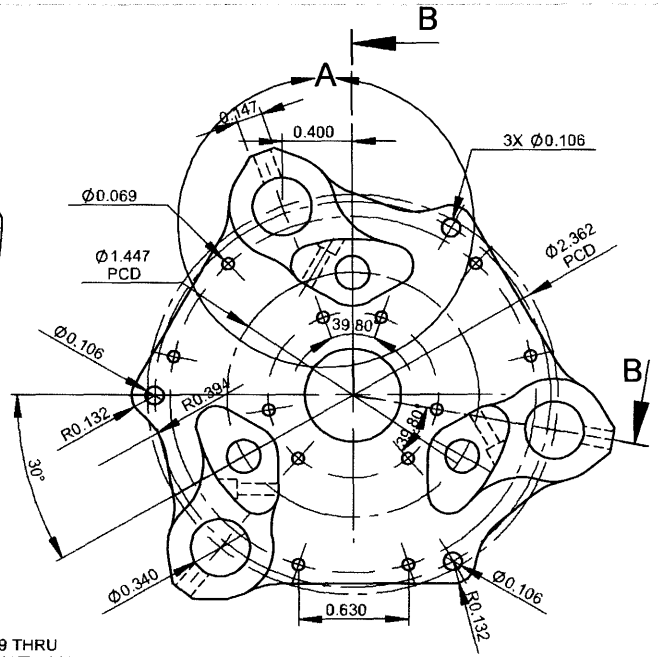

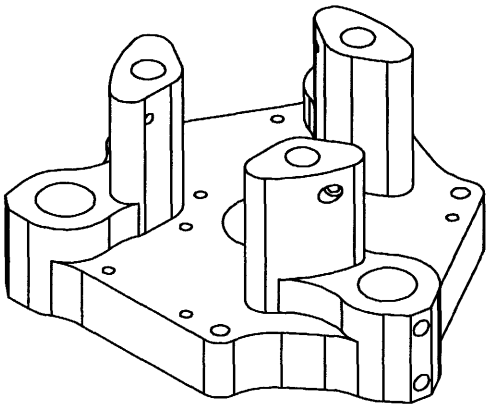

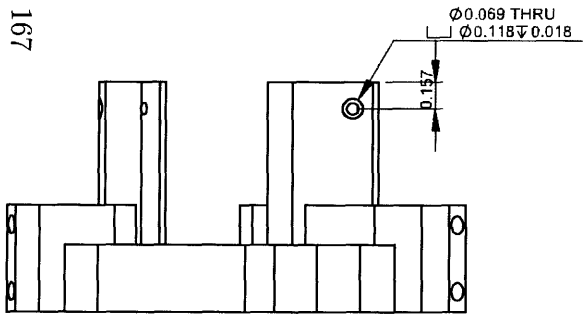

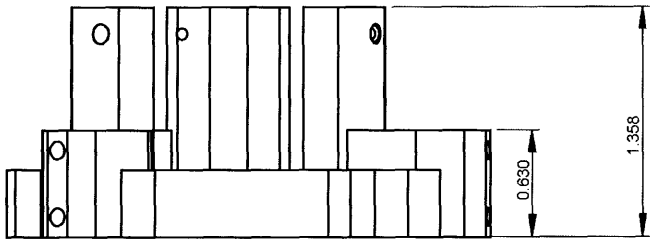

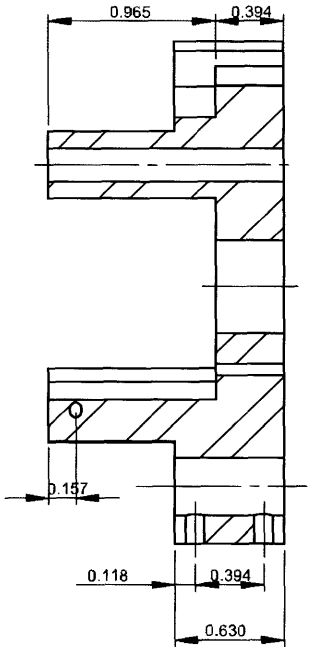

SECTION B-B

MATERIAL:

167

NOTES:						
1. DIMENSIONS ARE IN MM UNTOLERANCED DIMENSIONS ARE BASIC					DRAWN:	DJK
					DATE:	10/26/2007
					SCALE:	1:1
2. INTERPRET GEOMETRIC TOLERANCING PER: ASME Y14.5M – 1994				INITIAL RELEASE FOR CONSTRUCTION	CHKD:	
	REV	DATE	BY	DESCRIPTION	APVD:	

Massachusetts Institute of Technology
Precision Motion Control Laboratory

DWG. TITLE

DWG. NUMBER: **Invar Platform** REV: A

SHEET: 1 OF 1 SIZE: A

5 4 3 2 1

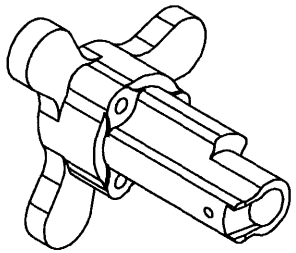

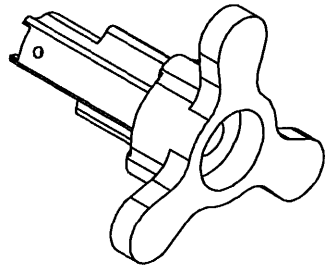

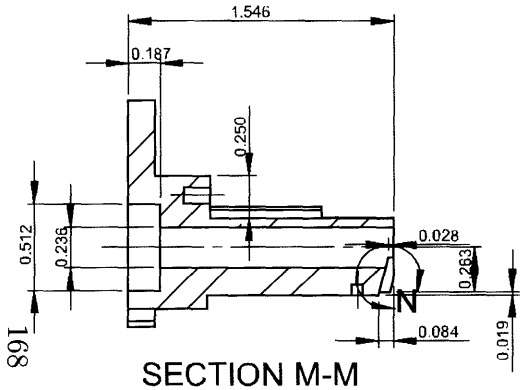

SECTION M-M

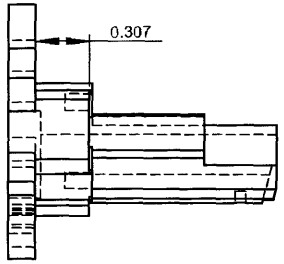

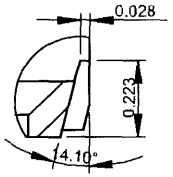

DETAIL N
SCALE 2 : 1

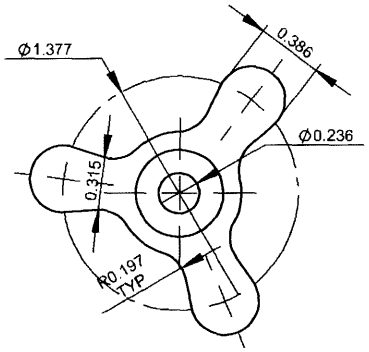

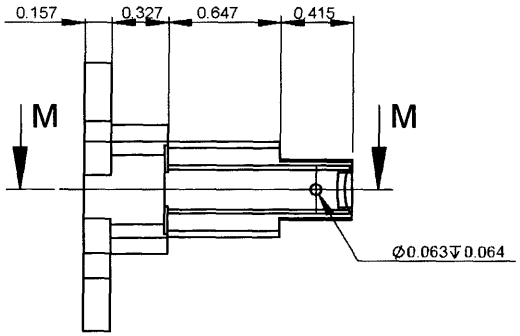

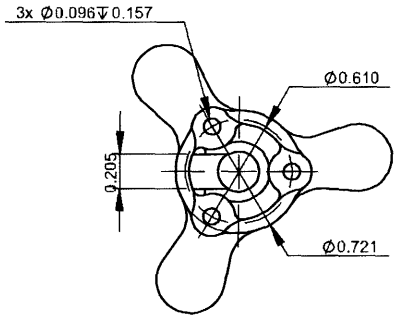

MATERIAL:

NOTES:						
1. DIMENSIONS ARE IN MM UNTOLERANCED DIMENSIONS ARE BASIC					DRAWN:	DJK
					DATE:	10/26/2007
					SCALE:	1:1
2. INTERPRET GEOMETRIC TOLERANCING PER: ASME Y14.5M – 1994				INITIAL RELEASE FOR CONSTRUCTION	CHKD:	
	REV	DATE	BY	DESCRIPTION	APVD:	

Massachusetts Institute of Technology
Precision Motion Control Laboratory

DWG. NUMBER: **Target** | REV: A

DWG. TITLE: Target

SHEET: 1 OF 1 | SIZE: A

5 4 3 2 1

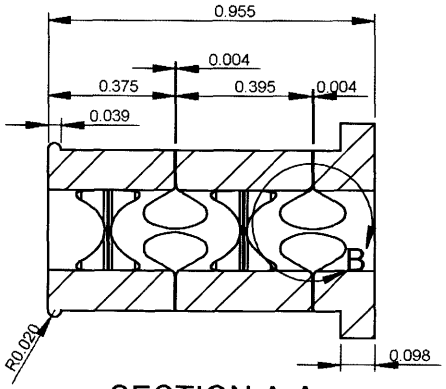

SECTION A-A

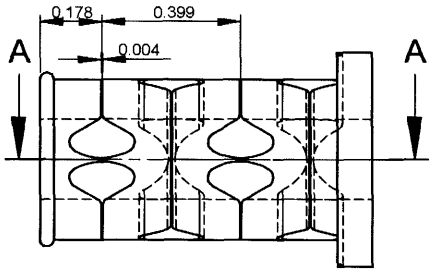

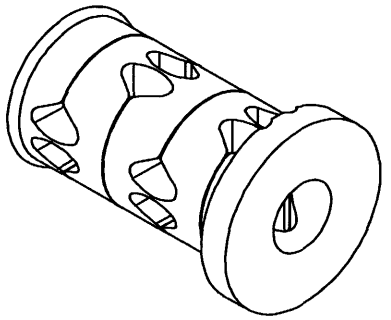

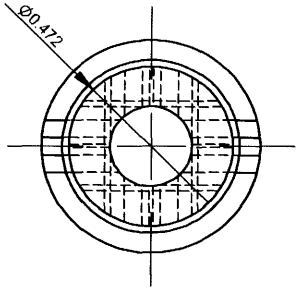

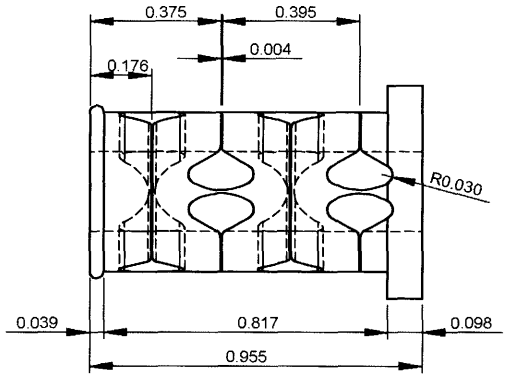

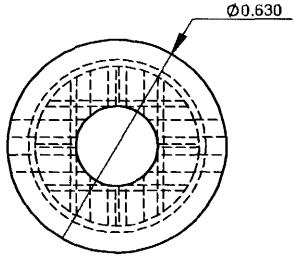

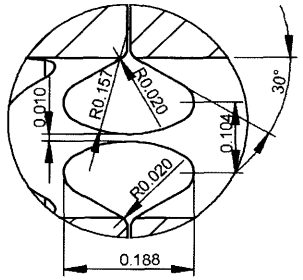

DETAIL B
SCALE 4 : 1

169

MATERIAL:

NOTES: 1. DIMENSIONS ARE IN MM UNTOLERANCED DIMENSIONS ARE BASIC 2. INTERPRET GEOMETRIC TOLERANCING PER: ASME Y14.5M – 1994					DRAWN:	DJK	Massachusetts Institute of Technology Precision Motion Control Laboratory
					DATE:	10/26/2007	
					SCALE:	2:1	DWG. NUMBER / REV.
				INITIAL RELEASE FOR CONSTRUCTION	CHKD:		DWG. TITLE: Decoupling Flexure
	REV	DATE	BY	DESCRIPTION	APVD:		SHEET 1 OF 1 / SIZE A

5 4 3 2 1

Appendix B

Vendors

ADE Corporation
KLA-Tencor Corporation
77 Rowe Street
Newton, MA 02466
Telephone: (617) 831-8000
URL: www.ade.com
Products Used: 2820-V Passive Probes, 8810 Gaging Modules

Agilent Technologies
5301 Stevens Creek Blvd
Santa Clara, CA 95051
Telephone: (877) 424-4536
URL: http://www.home.agilent.com/agilent/home.jspx
Products Used: HP 33120A Function Generator

BryCoat, Inc.
207 Vollmer Avenune
Oldsmar, FL 34677
Telephone: (727) 490-1000
URL: www.brycoat.com
Services Used: Titanium Nitride Coating

Central Machine Shop
77 Massachusetts Avenue
Building 38-001
Cambridge, MA 02139
Telephone: (617) 253-2392
URL: http://web.mit.edu/cmshop/
Services Used: Machining

dSPACE Inc.
28700 Cabot Drive - Suite 1100
Novi, MI 48377

Telephone: (248) 567-1300
URL: www.dspaceinc.com/index.htm
Product Used: ACE Kit DS1103

ECS, Inc. International
1105 S. Ridgeview
Olathe, KS 66062
Telephone: (913) 782-7787
URL: www.ecsxtal.com
Product Used: ECS-3X8 32.768 kHz Tuning Fork Crystals

Epoxy Technology
14 Fortune Drive
Billerica, MA 01821
Telephone: (978) 667-3805
URL: www.epotek.com
Products Used: 730 2-part Epoxy

Gradient Lens Corporation
207 Tremont Street
Rochester, NY 14608
Telephone: (800) 536-0790
URL: www.gradientlens.com
Products Used: Borescope

ISI Insulator Seal
6460 Parkland Drive
Sarasota, FL 34243
Telephone: (941) 751-2880
URL: www.insulatorseal.com
Products Used: Vacuum Feedthrough Manufacturer

Kaufmann, Co.
19 Walkhill Road
Norwood, MA 02062
Telephone: (617) 491-5500
URL: www.kaufmanco.com/
Products Used: Endmills, Drill bits

Kurt J. Lesker Co.
Pittsburgh, PA 15205
Telephone: (800) 245-1656
URL: www.lesker.com/newweb/index.cfm
Products Used: Vacuum Feedthrough Manufacturer

The MathWorks, Inc.
3 Apple Hill Dr.
Natick, MA 01760-2098
Telephone: (508)647-7000
URL: www.mathworks.com
Products Used: MATLAB, Simulink

Nanoscience Instruments, Inc.
9831 South 51st Street, Suite C119
Phoenix, AZ 85044
Telephone: (480) 940-3940
URL: www.nanoscience.com/index.html
Product Used: Akiyama Probe

Physik Instrumente
16 Albert St.
Auburn, MA 01501
Telephone: (508) 832-3456
URL: www.physikinstrumente.com
Products Used: P-.016-15H Piezo Actuator, E-507 High Voltage Amplifier

Ramco Machine, LLC
Rowley Business Park
27 Turcotte Memorial Drive
Rowley, MA 01969
Telephone: (978) 948-3778
URL: www.ramcomachine.com
Services Used: Machining, Heat Treating, Wire EDM

Stanford Research Systems
1290-D Reamwood Ave.
Sunnyvale, CA 94089
Telephone: (408) 744-9040
URL: www.srsys.com
Product Used: SR530 Lock-in Amplifier

Bibliography

[1] *Military Handbook - MIL-HDBK-5H: Metallic Materials and Elements for Aerospace Vehicle Structures (Knovel Interactive Edition).* U.S. Department of Defense, New York.

[2] Heiko Ahrens. http://www3.physik.uni-greifswald.de/method/afm/eafm.htm. 2001.

[3] A. F. Maarten Altelaar. Gold-enhanced biomolecular surface imaging of cells and tissue by sims and maldi mass spectrometry. *Analytical Chemistry*, 78:734–742, 2006.

[4] Peter Bagley. KLA-Tencor's ADE division, 2007. Personal communication with product application engineer.

[5] C. Bai. *Scanning Tunneling Microscopy and Its Applications.* Springer Series in Surface Sciences. Springer-Verlag, New York, second edition, 2000.

[6] C. Julian Chen. *Introduction to Scanning Tunneling Microscopy.* Springer Series in Surface Sciences. Oxford University Press, New York.

[7] Martin Culpepper. 2.75 constraint lecture. page 16, 2000.

[8] Physik Instrumente Datasheet. http://www.physikinstrumente.com/. 2008.

[9] C. F. Quate G. Binnig and Ch. Gerber. Atomic force microscope. *Physical Review Letters*, 56, 1986.

[10] Ch. Gerber G. Binnig, H. Rohrer and E. Weibel. Surface studies by scanning tunneling microscopy. *Physical Review Letters*, 49:57–61, July 1982.

[11] F. J. Giessibl. Advances in atomic force microscopy. *Reviews of Modern physics*, 75:949–983, 2003.

[12] F. J. Giessibl and G. Binnig. True atomic resolution on kbr with a tow-temperature atomic force microscope in ultrahigh vacuum. *Ultramicroscpy*, 42, 1992.

[13] Michael L. Holmes. *Analysis and Design of a Long Range Scanning Stage.* PhD dissertation, University of North Carolina at Charlotte.

[14] Michael L. Holmes and David L. Trumper. Design and three dimensional calibration of a measuring scanning tunneling microscope for metrological applications. *Precision Engineering*, 18:38–49, 1996.

[15] K. Kusumoto J. Wang and K. Nezu. Plasma arc cutting torch tracking control. *Advanced Motion Control, 2000. Proceedings. 6th International Workshop on*, 2000.

[16] Seung-Bae Jung and Seung-Woo Kim. Improvement of scanning accuracy of pzt piezoelectric actuators by feed-forward model-reference control. *Precision Engineering*, 16, 1990.

[17] M. Takahashi K. Takayanagi, Y. Tanishiro and S. Takahashi. Structural analysis of si (111)-7 7 by uhv-transmission electron diffraction and microscopy. *Journal of Vacuum Science and Technology*, 3:1502–1506, May 1985.

[18] K. Karrai and R. D Grober. Piezoelectric tip-sample distance control for near field optical microscopes. *Applied Physics Letters*, 66, 1995.

[19] K. Karrai and R. D Grober. Tip-sample distance control for near-field scanning optical microscopes. *Proceedings of SPIE*, 2535, 1995.

[20] Nicolaas F. de Rooij et al. Kaspar Suter, Terunobu Akiyama. Tuning fork afm with conductive cantilever. *scanning tuneling MIcroscopy/Spectrosopcy and Related Techniques: 12th International Conference*, pages 227–233, 2003.

[21] Hiroshi Itoh Toshihisa Horiuchi Kazumi Matsushige Kei Kobayashi, Hirofumi Yamada. Analog frequency modulation detector for dynamic force microscopy. *Reviews of Scientific Instruments*, 72(12):4383–4387, 2001.

[22] Katherine A. Lilienkamp and David L. Trumper. Dynamic signal analyzer for dspace. In *Proceedings of dSPACE User's Conference*, 2000.

[23] Premier Employement LTD. www.premier-employment.co.uk/.

[24] Kent Lundberg. 6.331 laboratory 3: Phase locked loops. pages 4383–4387, 2007.

[25] T. E. Shoup M. F. Spotts and L. E. Hornberger. *Design of Machine Elements.* Pearson Prentice Hall, Upper Saddle River, New Jersey, eighth edition, 2000.

[26] Dragan Maksimovic. Experiment 4: Cmos 4046 phase-locked loop. 1997.

[27] Aaron David Mazzeo. Accurate capacitive metrology for atomic force microscopy. Masters of science, Massachusetts Institute of Technology, Department of Mechanical Engineering, 2005.

[28] Mitutoyo, http://www.mitutoyo.co.jp/eng/products/gaugeblock/Gauge *Small Tools Instrumnents and Data Management*, Accessed February 2008.

[29] C. V. Newcomb and I. Flinn. Improving the linearity of piezoelectirc ceramic actuators. *Electronics letters*, 18, 1982.

[30] Norman S. Nise. *Control Systems Engineering.* John Wiley and Sons, Inc., fourth edition, 2004.

[31] H. Wolff O. Jusko, X. Zhao and G. Kilening. Design and three dimensional calibration of a measuring scanning tunneling microscope for metrological applications. *Review of Scientific Instruments*, 65:2514–2518, 1994.

[32] W. Mosch R. Arora. *High Voltage Insulation Engineering.* New Age Publishers, 1995.

[33] John Redford. http://world.std.com/ jlr/doom/armstrng.htm. 1996.

[34] David L. Trumper Robert J. Hocken and Chunhai Wang. Dynamics and control of the uncc/mit sub-atomic measuring machine. *CIRP Annals*, 50:373–376, 2001.

[35] Aaron Gawlik Ross Ian McKenzie. Research Assistants in the Precicion Motion Control Laboratory, 2007. Personal communication with labmates.

[36] Stuart T. Smith. *Flexures: Elements of Elastic Mechanisms.* Gordon and Breach Science Publishers, New York.

[37] Andrew John Stein. A metrological atomic force microscope. Masters of science, Massachusetts Institute of Technology, Department of Mechanical Engineering, September 2002.

[38] N. F. de Rooij T. Akiyama, K. Suter. Novel dynamic scanning microscope probe and its application to local electrical measurement in an ion sensitive field effect transistor. *Mater. Res. Soc. Symp. Proc.*, 838, 2005.

[39] N. F. de Rooij T. Akiyama, K. Suter and U. Staufer. Novel dynamic scanning microscope probe and its application to local electrical measurement in and ion sensitive field effect transistor. *Mater. Res. Soc. Symp. Proc.*

[40] U. Staufer T. Akiyama and N. F. de Rooij. Self-sensing and self-actuating probe based on quartz tuning fork combined with microfabricated cantiliver for dynamic mode atmoic force microscopy. *Applied Surface Science*, 210, 2003.

[41] U. Staufer T. Akiyama and N. F. de Rooij. Symmetrically arranged quartz tuning fork with soft cantilever for intermittent contact mode atomic force microscopy. *Review of Scientific Instruments*, 74, 2003.

[42] Jr Thomas B. Greenslade. http://physics.kenyon.edu/.